MILLENNIAL- TO ANNUAL-SCALE HOLOCENE CLIMATE CHANGE IN THE ALASKAN ARCTIC AND TROPICAL ANDES INFERRED FROM PHYSICAL SEDIMENTOLOGY AND GEOCHEMICAL INDICATORS PRESERVED IN FINELY LAMINATED ALPINE LAKE SEDIMENT ARCHIVES

by

Broxton Williams Bird

B.A. Hamilton College, 1999

M.Sc. California State University-Fullerton, 2005

Submitted to the Graduate Faculty of

Geology and Planetary Science in partial fulfillment

of the requirements for the degree of

Doctor of Philosophy

University of Pittsburgh

2009

UNIVERSITY OF PITTSBURGH

GEOLOGY AND PLANETARY SCIENCE

This dissertation was presented

by

Broxton Williams Bird

It was defended on

June 30, 2009

and approved by

Dr. Mathias Vuille, Assistant Professor, University at Albany, State University of New York, Department of Atmospheric and Environmental Sciences

Dr. Emily Elliott, Assistant Professor, University of Pittsburgh, Department of Geology and Planetary Science

Dr. Michael Rosenmeier, Assistant Professor, University of Pittsburgh, Department of Geology and Planetary Science

Dr. Brian Stewart, Associate Professor, University of Pittsburgh, Department of Geology and Planetary Science

Dissertation Advisor: Dr. Mark Abbott, Associate Professor, University of Pittsburgh, Department of Geology and Planetary Science

MILLENNIAL- TO ANNUAL-SCALE HOLOCENE CLIMATE CHANGE IN THE ALASKAN ARCTIC AND TROPICAL ANDES INFERRED FROM PHYSICAL SEDIMENTOLOGY AND GEOCHEMICAL INDICATORS PRESERVED IN FINELY LAMINATED ALPINE LAKE SEDIMENT ARCHIVES

Broxton Williams Bird, Ph.D.

University of Pittsburgh, 2009

High-resolution sediment archives from small alpine lakes in the Alaskan Arctic and tropical Andes were used to investigate Holocene climate change in these climatically sensitive and important regions. Varved minerogenic sediments from glacial-fed Blue Lake, Brooks Range Alaska (1275 m asl), were used to derive a proxy temperature record between AD 730-2005. Cool temperatures characterize the late Holocene (last millennial average, or LMA = 4.2°C) with 20th century warming anomalous within the context of the last 1275 years (0.8°C above LMA). However, temperatures between AD 1350-1450 and AD 1500-1620 approached modern values (0.4 and 0.3ºC above LMA, respectively). Prolonged cooling at Blue Lake occurred from AD 1620-1880, during the Little Ice Age (LIA). LIA cooling and 20th century warming correspond to radiative minima and maxima, respectively. However, the relationship between radiative forcing and temperature is not consistent through the record, suggesting that other factors contributed to temperature variability in this region. In the tropics, South American summer monsoon (SASM) variability during the last 2300 years was reconstructed from oxygen isotope ratios of authigenic carbonate ($\delta^{18}O_{cal}$) preserved in varved sediments from Laguna Pumacocha (4300 m asl), Peru. High $\delta^{18}O_{cal}$ values and reduced variability during the Medieval Climate Anomaly (MCA; AD 920-1050) suggest that the SASM and El Niño-Southern Oscillation

(ENSO) were weak due to reduced easterly tropospheric flow and cooling within the eastern tropical Pacific (ETP). Low $\delta^{18}O_{cal}$ from during the LIA (AD 1415-1820) and enhanced variability from AD 1415-1770 suggest that the SASM and ENSO were strong as a result of enhanced easterly tropospheric flow and warm, but variable, sea surface temperatures in the ETP, respectively. These ocean-atmosphere responses reflect the tropical Pacific's response to radiative forcing described by the ocean dynamical thermostat model (Clement et al. 1996). Long-term $\delta^{18}O_{cal}$ trends at Pumacocha suggest that the SASM was weak during the early Holocene and then strengthened through the Holocene as Southern Hemisphere insolation increased. This confirms the importance of orbital controls on SASM dynamics. However, the Andean SASM strengthened to a greater extent than the SASM over the Amazon basin, indicating that these regions respond differently to similar forcing mechanisms.

TABLE OF CONTENTS

PREFACE ..... **XVIII**

1.0 INTRODUCTION **1**

2.0 A 2000 YEAR VARVE-BASED CLIMATE RECORD FROM THE CENTRAL BROOKS RANGE, ALASKA **5**

2.1 ABSTRACT **5**

2.2 INTRODUCTION **6**

2.3 STUDY AREA **7**

2.4 CLIMATIC SETTING **9**

2.5 METHODS **10**

2.5.1 Core collection **10**

2.5.2 Radiometric Age Control **11**

2.5.3 Thin-section preparation **12**

2.5.4 Core imaging and couplet measurements **13**

2.6 RESULTS **14**

2.6.1 Sedimentology **15**

2.6.2 Radiometric age control **17**

2.6.2.1 ^{137}Cs and ^{210}Pb **17**

2.6.2.2 ^{14}C **17**

2.6.3 Varve Chronology 18
2.6.4 Varve thickness trends 19
2.7 DISCUSSION 20
2.7.1 Varve thickness and the instrumental record 20
2.7.2 Temperature reconstruction 24
2.7.3 Regional paleoenvironmental records 27
2.7.4 AD 10 to 730: first millennium wet period 27
2.7.5 AD 730 to 1620: late Neoglacial cooling 29
2.7.6 AD 1620 to 1880: the Little Ice Age 30
2.7.7 AD 1880 to 2005: post-Little Ice Age warming 32
2.7.8 Comparisons with Arctic basin records 33
2.8 SUMMARY 35
3.0 SOUTH AMERICAN SUMMER MONSOON VARIABILITY DURING THE LITTLE ICE AGE AND MEDIEVAL CLIMATE ANOMALY 37
3.1 ABSTRACT 37
3.2 INTRODUCTION 38
3.3 STUDY AREA 39
3.4 METHODS 42
3.4.1 Sediment core recovery 42
3.4.2 Sediment imaging and mineralogy 43
3.4.3 Modern sedimentation and Limnology 43
3.4.4 Radiometric age control 44
3.4.5 Couplet-based age control 46

3.4.6 Carbonate sampling and stable isotope measurements 46
3.4.7 Data filtering and wavelet analysis 47
3.5 RESULTS 48
3.5.1 Sedimentology 48
3.5.2 Age Control 49
3.5.3 Modern $\delta^{18}O_{lw}$ 51
3.5.4 Modern $\delta^{18}O_{cal}$ and $\delta^{18}O_{lw}$ 53
3.5.5 Annual $\delta^{18}O_{cal}$ (AD 1797 to 2007) 53
3.5.6 $^{18}O_{cal}$ from 277 BC to AD 1797 55
3.6 DISCUSSION 57
3.6.1 Climatic significance of Pumacocha $\delta^{18}O_{cal}$ 57
3.6.2 The SASM and $\delta^{18}O$ 59
3.6.3 SASM precipitation during the MCA and LIA 60
3.6.4 Mechanisms of late Holocene climate change in tropical South America 63
3.6.5 SASM response to radiative forcing during the MCA and LIA 67
3.7 SUMMARY AND CONCLUSIONS 69
4.0 TROPICAL SOUTH AMERICAN HYDROLOGIC VARIABILITY DURING THE HOLOCENE: EVIDENCE FOR PRECIPITATION PARTITIONING BETWEEN THE ANDES AND THE AMAZON 71
4.1 ABSTRACT 71
4.2 INTRODUCTION 72
4.3 STUDY AREA 75
4.4 METHODS 77

4.4.1 Core collection 77
4.4.2 Core imaging 78
4.4.3 Modern sedimentation and limnology 78
4.4.4 Age control 79
4.4.5 Carbonate sampling and stable isotope measurements 81
4.5 RESULTS 82
4.5.1 General Sedimentology 82
4.5.2 Couplet Sedimentology 84
4.5.3 Age control 84
4.5.4 Modern controls on Pumacocha $\delta^{18}O_{lw}$ 86
4.5.5 Modern carbonate 88
4.5.6 Holocene oxygen isotope trends 88
4.6 DISCUSSION 90
4.6.1 Environmental significance of Pumacocha $\delta^{18}O_{cal}$ 90
4.6.2 Holocene precipitation trends 93
4.6.3 Holocene precipitation partitioning 102
4.7 SUMMARY AND CONCLUSIONS 104
5.0 SUMMARY AND CONCLUSIONS 107
BIBLIOGRAPHY 110

LIST OF TABLES

Table 1 Names, coring device, and length of the cores located in Figure 1c 11

Table 2 Results of ^{210}Pb and ^{137}Cs assays from core B-99 shown in Figure 4 11

Table 3 Radiocarbon ages and related data for samples from Blue Lake, Alaska..... 12

Table 4 Values of truncated varve thicknesses in Figure 3 23

Table 5 Regression statistics for the relationship between varve thickness at Blue Lake and annual climate data from Atigun Pass 25

Table 6 Name, type, and length of cores collected from Pumacocha. The (*) denotes which cores were used in the final composite record 42

Table 7 Pumacocha ^{210}Pb, ^{226}Ra and ^{137}Cs results from freeze core D-08 45

Table 8 Radiocarbon ages from Laguna Pumacocha..... 46

Table 9 Depths and ages of stratigraphic units in the Pumacocha core..... 48

Table 10 Name, type, and length of cores collected from Pumacocha. The (*) denotes which cores were used in the final composite record..... 77

Table 11 Pumacocha ^{210}Pb, ^{226}Ra and ^{137}Cs results from freeze core D-08 80

Table 12 Radiocarbon ages and associated data from Laguna Pumacocha..... 81

Table 13 Depths and ages of sediment transitions in the Pumacocha core 83

LIST OF FIGURES

Figure 1 (a) Map of the North American Arctic showing Blue Lake (white box) in the Brooks Range (dark grey shaded area) and other records discussed in the text (MtL = Mt. Logan, ML = Marcella Lake, US = Upper Soper Lake, DL = Donnard Lake, TB = Tuborg Lake, MrL = Murry Lake, and lake C2). (b) Topographic map of the Blue Lake drainage basin (shaded grey with a dashed outline), and the Blue Lake glacier in the upper part of the watershed. (c) Blue Lake with core locations (Table 1). 8

Figure 2 (a) Thin section photomicrograph from core A-99 showing the fine laminations characteristic of the varved sediments during the Little Ice Age. The lighter layers are the clay caps that overlie the darker silty portion of the varves. (b) High-resolution digital photograph of surface core D-06 showing the same interval represented by the thin section in part (a). The black line designates where the couplets were measured. (c) Image of core C-06 from the lower portion of the core (below 100 cm) where varve thickness increases. Note that the color and structure of the varves are the same as in (a) and (b), only thicker. 14

Figure 3 Varve thickness measurements from the network of cores from Blue Lake plotted by depth. Despite subtle differences, the varves have similar thicknesses and downcore thickness patterns across the lake. Layers identified as turbidites are designated with an astrix (*). The values are truncated in order to show the finer varves. Thicknesses of the clipped varves are reported in Table 4. 15

Figure 4 (a) ^{210}Pb (circles) and ^{137}Cs (squares) activity profiles in core B-99 (Table 2). (b) Geochronology results from ^{137}Cs (square) and ^{210}Pb (dashed line) analyses plotted with the age-depth model derived from varve counting (solid line). (c) ^{137}Cs assays (black square) are plotted with the AMS ^{14}C age (black circle; Table 3) and the age-depth model determined from varve counting (black line). The strong agreement between the ages based on varve counting and those from radiometric dating techniques support the conclusion that the couplets in the Blue Lake cores are deposited annually. (d) The complete varve derived age-depth model (black line) with ^{137}Cs (square) and ^{14}C (circle) measurements. Note the change in sedimentation rate at 730 AD. 16

Figure 5(a) Composite varve-thickness measurements from Blue Lake. The black line is a 5-point moving average; grey line is the annual values. (b) Bulk density from core B-99 shown as the standard deviation from the mean. Bulk density values are within 1σ from the mean at 1.5 cm, indicating that increasing varve thickness at the top of the core are not an artifact of uncompacted sediments. 18

Figure 6(a) Varve thickness plotted against average JJA temperatures from Atigun Pass (AD 1993-2005; black circles). The correlation between varve thickness and temperature is poor when all the data are considered (line a; $r^2 = 0.02$; $p = 0.65$). With AD 1998 removed, the correlation between varve thickness and temperature is significant at the 90% confidence interval (CI; line b; $r^2 = 0.28$; $p = 0.1$). Also plotted are the log-transformed varve-thickness data and average JJA Atigun Pass temperatures (open triangles) with AD 1998 excluded. The log-transformed data show a better correlation ($r^2 = 0.31$; $p = 0.08$; 92% CI; line c). (b) Varve thickness plotted against total JJA precipitation at Atigun Pass (AD 1983-2005). The correlation between varve thickness and precipitation is statistically insignificant (line a; $r^2 < 0.01$; $p = 0.82$),

even with AD 1998 removed (line b; $r^2 = 0.04$; $p = 0.38$). The linear regression equations and statistics are located in Table 5. 22

Figure 7 Blue Lake temperature reconstruction (black solid line) with the upper and lower 95% confidence intervals (grey lines) shown as the deviation from the last millennium average (4.2°C). The temperature reconstruction is derived for the period AD 730-2005. Temperatures prior to AD 730 are not reconstructed because varve thicknesses during this time are well beyond the range of the calibration period, reducing confidence in the results. We also suspect that increased varve thickness during this period reflects the role of enhanced precipitation on varve formation (see text for discussion)..... 25

Figure 8 (a) Blue Lake varve thicknesses plotted as the standard deviation from the mean thickness (5-point moving average). Black vertical bars indicate inferred cool intervals in the Brooks Range. (b) Blue Lake temperature reconstruction shown as the difference from the last millennium average (51-point moving average) with the grey lines denoting the upper and lower 95% CI. (c) Glacier fluctuations in the Brooks Range (Ellis and Calkin 1984). (d) Greater Yukon aridity as represented by the Marcella Lake $\delta^{18}O$ record (Anderson et al., 2007). The grey box highlights the period during which precipitation, rather than summer temperature, is believed to have dominated varve formation in Blue Lake..... 28

Figure 9 The 5-point moving average of normalized Blue Lake varve thicknesses compared with normalized 5-point moving average varve records from the eastern Canadian Arctic. (a) Blue Lake, (b) Donnard Lake, (c) Murray Lake, (d) Upper Soper Lake, (e) Tuborg Lake, and (f) Lake C2. The Blue Lake record is similar to Upper Soper Lake, Tuborg Lake, and Lake C2, showing a distinct and similarly phased LIA and post-LIA warming. The timing and magnitude of events

at Blue Lake do not match Donnard Lake and Murray Lake as clearly. The locations of the Canadian lakes is shown in Figure 1a. 34

Figure 10 Map of South America showing the location of records discussed in the text (CB= Cariaco Basin, MB = L. Mucubaji, PA = L. Pallcacocha, HIC = Huascaran Ice Core, PC = Pumacocha, QIC = Quelccaya Ice Cap, LT = L. Titicaca). The shaded regions denote the location of precipitation maxima during the austral summer (December, January, February; on the left) and winter (June, July, August; on the right). Maxima over the oceans are related to low-level convergence of the trade winds and subsequent rising motion associated with the Intertropical Convergence Zone (ITCZ). Maxima over South America are associated with the SASM. 40

Figure 11(a) Topographic map of the Pumacocha watershed and surrounding area. (b) Bathymetric map of Pumacocha showing the location were cores collected. 41

Figure 12 (a) Generalized stratigraphy of the upper 2 meters of the Laguna Pumacocha sediment record, (b) high-resolution digital image characteristic of the well-preserved couplets present in the upper 176.2 cm of the sediment column, and representative SEM images of light (c) and dark(d) colored laminations. 49

Figure 13 Results of radiometric age control and couplet-based ages from the upper portion of the Laguna Pumacocha record. 50

Figure 14 Modern (a) percent relative humidity (%RH), (b) lake level, and (c) monthly $\delta^{18}O_{lw}$ from Laguna Pumacocha. (d) Water isotope of samples collected from Pumacocha between June 2005 and May 2008 (open circles) are plotted with the so-called global meteoric water line (GMWL) and isotopic measurements from nearby lakes that exhibit open (black squares) and

closed (open triangles) hydrologies. (e) Scatter plot of d18olw and surface air temperature (red circles) and lake surface temperature (open blue squares). 52

Figure 15(a) $\delta^{18}O_{cal}$ of individual carbonate lamina sampled from Pumacocha. The light gray line represents the raw data and the thick black line is a 5-point moving average. (b) Estimated net radiative forcing (Crowley et al. 2000) of solar variability, aerosol loading, greenhouse gasses, and volcanic activity from AD 1797 to the present. 54

Figure 16 Wavelet power spectra of (a) average December, January, February sea surface temperatures in the NINO 3.4 region and (b) Pumacocha $\delta^{18}O_{cal}$ filtered with a 20 year high-pass Butterworth filter (N = 3) from AD 1871 to 2007. The NINO 3.4 and Pumacocha wavelet power spectra show significant variability between 2 and 8 years. 54

Figure 17(a) Wavelet power spectra of the Laguna Pumacocha δ18Ocal record for the last 2000 years. (b) Oxygen isotopic values from Laguna Pumacocha versus age data are shown in light gray with the thick black line denoting the 5-point moving average of the raw data. (c) 5-point moving average of δ18O from the Quelccaya Ice Cap, PE (Thompson et al. 1985). (d) Crowley et al. (2001) net radiative forcing (light gray line) and residual 14C (Δ14C) (black line). (e) Titanium concentration (%) in sediment cores from the Cariaco Basin (Haug et al. 2001). (f) Magnetic susceptibility (10-6) from Laguna Mucubaji, VE (Polissar et al., 2006). (g) Northern Hemisphere temperature reconstruction by Moberg et al. (2005). 57

Figure 18 Map of South American tropics with locations of sites discussed in the text. CB = Cariaco Basin, LVB = Laguna Verdes Baja, CTP = Cueva del Tigre Perdido, HIC = Huascaran ice core, LJ = Laguna Junin, AC = Laguna Azulcocha, LTCK = Laguna Taypi Chaka Kkota, LV = Laguna Viscachani, IIC = Illimani ice core, BC = Cueva Botuvera, NOR = Nordeste Region 76

Figure 19(a) Topographic map of the Pumacocha (long dash line) and Pucpush catchments (short dash line). (b) Bathymetric map of Pumacocha. 77

Figure 20 Composite stratigraphic column of the Pumacocha sediment record. (b) A high-resolution digital image from the upper portion of the Pumacocha sediment record showing a typical section of finely laminated millimeters scale varves. (c) Representative SEM image showing the euhedral calcite crystals that comprise the sediments in the light lamina from the varved portion of the Pumacocha sediment record. (d) Representative SEM image showing the organic matter that comprises the dark lamina form the varved portion of the Pumacocha record. 83

Figure 21 The left graph shows the varve-^{137}Cs-^{14}C age model for the upper 160 cm. Ages based on couplet counts have an estimated error of +/- 1% (shown with the increasing error range in black). Error ranges for ^{14}C are shown with horizontal bars for ages, and vertical bars for depth. The Right graph shows the entire age model for the last 11,500 years. A 6th order polynomial was fit to these data to derive the final age depth model. 85

Figure 22 Modern (a) percent relative humidity (%RH), (b) lake level, and (c) surface $\delta^{18}O_{lw}$ measurements from Pumacocha. (d) Plot of surface water and $\delta^{18}O_{lw}$ from Pumacocha (black circles) and other open (open squares) and closed (open triangles) tropical Andean lakes. These lakes comprise a local evaporation line that plots off the so-called global meteoric water line (GMWL). (e) Air and surface temperature plotted against lake water oxygen isotopic composition. 87

Figure 23(a) Plot of $\delta^{18}O_{cal}$ from Pumacocha (black line) between 11,200 cal yr B.P. and -57 varve yr B.P. (B.P. = AD 1950) plotted with Huascaran $\delta^{18}O$ (gray line; VSMOW). (b) Plot of $\delta^{13}C_{cal}$ and $\delta^{18}O_{cal}$ measurements from Pumacocha. 89

Figure 24 Plot comparing paleoclimate records from (a) Laguna Verdes Baja, VE, (b) Caverna Botuvera, BR, (c) Cueva del Tigre Perdido, PE, (d) Laguna Pumacocha, PE, (e) Huascaran ice core, PE, (f) Illimani ice core, BO, (g) Cariaco Basin, VE. The solid line in each profile is the calculated slope from 10,000 to 2400 cal yr B.P. and the dashed line is the slope calculated from 2400 cal yr B.P. to the present. 94

Figure 25 Stratigraphic profile of Laguna Azulcocha (-12.06825°, -75.67083°; 4450 m asl). Radiocarbon dates represented by black boxes constrain the middle Holocene transition from dry conditions indicated by grasses and peat in the core, to lake sediments between 5410 and 5070 cal yr B.P. Laminated sediments after 4420 cal yr B.P. indicate deepwater conditions..... 98

Figure 26 Differences between Andean and Amazonian precipitation are represented by the difference between the Pumacocha $\delta^{18}O_{cal}$ and Cueva del Tigre Perdido $\delta^{18}O_{cal}$ records ($\delta^{18}O_{Pumacocha}$-$\delta^{18}O_{CTP}$). 103

PREFACE

This research was supported by funding from the National Science Foundation. Special thanks are extended to Donald Rodbell, Nathan Stansell, Colin Cooke, Daniel Nelson, Byron Steinman, James Richardson III, Enrique Lopez, Jaime Escobar, Alejandro Chu, and Eden de Pumacocha for their invaluable assistance in the field. Special thanks are also extended to Jeffery Evans and Joseph Ortiz for their assistance with statistical analysis and Amy Wolfe and Dan Bain for their assistance with water chemistry data collection.

1.0 INTRODUCTION

Currently, one of the major objectives of paleoclimate research is to document and understand the causes of Holocene climate variability at annual to centennial scales because abrupt climate change at these time-scales has the potential to greatly affect human society. This goal has become more pressing in recent years, as it is increasingly apparent that the availability of some natural resources, such as fresh water, are being impacted by ongoing climate change (IPCC, 2007). Model simulations suggest that this situation will be exacerbated by continued increases in anthropogenic radiative influences (IPCC, 2007). In order to better understand how future climate change will impact natural resources that are sensitive to the mean climate state (e.g. glaciers, rivers, and lakes), we must first understand how the climate system responded to natural radiative variability in the past. This requires well-dated, high-resolution paleoclimate archives that capture climate variability during a range of mean global climate states from climatologically important regions, such as the Arctic and the tropics. It is important to understand the natural range of long-term climate variability in these regions because the Arctic amplifies climate change through ocean-atmosphere-cryosphere feedbacks, and variations in the tropical ocean-atmosphere system influence inter-hemispheric temperature and precipitation patterns.

Unfortunately, sub-centennially and annually resolved paleoclimate archives from the Arctic and tropical regions are rare. Tree rings, ice cores, and lake sediments are among the

best-resolved paleoclimate archives, but trees that display annual bands are not common in tropical settings (Christie et al., In Press), and ice caps suitable for ice core studies are restricted to particular climatic settings and are not always well distributed (Thompson et al., 2005). Lakes, in contrast, are well distributed across the Arctic and tropics, sensitive to high-frequency climate variability, and, with the correct environmental and geologic setting, capable of preserving annually resolved climate archives. These qualities make lacustrine records well suited for detailed paleoclimate investigations.

In the following chapters, new well-dated, annually- to decadally-resolved sediment archives from small alpine lakes in the Alaskan Arctic and tropical Andes are presented. With a multiproxy approach that incorporates physical sedimentology and geochemical analyses, these records document interannual to millennial-scale modes of climate change and allow an assessment of what mechanisms are responsible for the observed climatic shifts. The chapters of this dissertation are compiled from individual stand-alone papers that are intended for individual publication. Therefore, there is some redundancy between the chapters, particularly with respect to the study area description and methods outlined in Chapters 3 and 4.

Chapter 2 presents an annually resolved varve-based reconstruction of summer climate (June-July-August; JJA) from the Alaskan Arctic that spans the last 2000 years. This study was published in a special issue of the *Journal of Paleolimnology* that addressed Arctic climate change during the last 2000 years. Using modern varve thickness and regional climate datasets, JJA temperatures at Blue Lake, Brooks Range, Alaska were reconstructed from AD 730 to the present. Wet, and likely warm, conditions characterize the early part of the record from AD 10-730. After AD 730, temperatures cooled and precipitation declined. Although generally cool from AD 730-2005, three warm periods are apparent, AD 1350-1450, AD 1500-1620, and the

20th century, with the latter being the greatest in the last 1275 years. The longest cool period in the record occurred between AD 1620-1880, which is contemporaneous with the LIA (Mann and Jones, 2003; Moberg et al., 2005). Although LIA cooling and 20th century warming correspond to radiative minima and maxima, respectively, the relationship between radiative forcing and inferred temperature change is not clear throughout the record. This implies that other forcing mechanisms, possibly related to the mean state of the coupled Pacific ocean-atmosphere system, influence climate in this region.

Chapter 3 presents an oxygen isotope-based reconstruction of the South American summer monsoon (SASM), which spans the last 2300 years. Oxygen isotope ratios were measured on authigenic carbonate preserved in varved sediments from Laguna Pumacocha, which is located on the eastern flank of the central Andes, at 4300 m asl and 10°S. The most prominent features of the Pumacocha record are a period of high $\delta^{18}O_{cal}$ and reduced variability during the Medieval Climate Anomaly (MCA) from AD 920-1050, and a prolonged period of low $\delta^{18}O_{cal}$ during the LIA from AD 1415-1820 with significant variability from AD 1500-1770. These climate anomalies track changes in radiative forcing inferred from solar activity, green house gasses, aerosols, and volcanism (Crowley, 2000; Reimer et al., 2004). Because SASM variability is fundamentally linked to zonal and meridional sea surface temperature anomalies in the tropical Pacific (e.g. El N>Garreaud et al., 2003), covariance between the Pumacocha SASM reconstruction and reconstructions of radiative forcing and solar variability during the MCA and LIA (Crowley, 2000; Reimer et al., 2004) suggest that radiative forcing affected the tropical Pacific ocean-atmosphere system and that its response impacted the SASM. These findings concur with the dynamical response of the tropical Pacific to radiative forcing (Clement et al., 1996), which has also been suggested to influence Northern Hemisphere climate via El Niño-like

atmospheric teleconnections resembling the North Atlantic Oscillation (Emile-Geay et al., 2007). An atmospheric link between the tropical Pacific and Northern Hemisphere climate may explain the striking resemblance between the Pumacocha SASM reconstruction and Northern Hemisphere temperature during the last 2000 years (Moberg et al., 2005).

Chapter 4 expands the SASM reconstruction presented in Chapter 3 to encompass the entire Holocene and the end of the late Glacial at decadal resolution. The evolution of the SASM through the Holocene has been the focus on considerable research (e.g. Abbott et al., 2003; Abbott et al., 1997b; Baker et al., 2005; Baker et al., 2001a; Polissar et al., 2006a; Wirrmann and De Oliveira Almeida, 1987). However, previous studies have been limited by their temporal resolution and the lack of lowland SASM records for comparison. Comparing the Pumacocha SASM reconstruction with other tropical South American paleoclimate records (Behling and Hooghiemstra, 2000; Cruz et al., 2005; Polissar et al., 2006a; Ramirez et al., 2003; Thompson et al., 1995; van Breukelen et al., 2008; Wang et al., 2007) suggests that millennial scale Holocene climate change in the tropical South American Andes was synchronous and that millennial-scale changes in orbital insolation (Laskar et al., 2004) drove these long-term trends. However, differences between the Pumacocha record and decadally-resolved speleothem records from the Peruvian Amazon (van Breukelen et al., 2008) and the southeastern coast of Brazil (Cruz et al., 2005; Wang et al., 2007) shows that the evolution of the SASM was asymmetric between the Andes and Amazon basin, with the SASM becoming stronger over the Andes, despite similar forcing mechanisms (i.e. orbital insolation and radiative forcing). These results suggest that Andean climate, and the factors that influence it, are more sensitive to changes in radiative forcing than the Amazon basin, which is consistent with recent model simulations .

2.0 A 2000 YEAR VARVE-BASED CLIMATE RECORD FROM THE CENTRAL BROOKS RANGE, ALASKA

2.1 ABSTRACT

Varved minerogenic sediments from glacial-fed Blue Lake are used to investigate late Holocene climate variability. Varve-thickness measurements track summer (June-July-August) temperature recorded at Atigun Pass, located 41 km east at a similar elevation (r^2 = 0.31, p = 0.08). Results indicate that climate in the Brooks Range from AD 10-730 (varve yr) was warm with precipitation inferred to be higher than during the 20th century. The varve-temperature relationship for this period was likely compromised because the glacier was greatly reduced, or absent, exposing sub-glacial sediments to erosion from enhanced precipitation. Therefore, this portion of the varve record was not used in our temperature reconstruction. Varve inferred summer temperatures and precipitation decreased after AD 730, averaging 0.4°C above the LMA (last millennial average = 4.2°C) from AD 730-850, and 0.1°C above the LMA from AD 850-980. Cooling culminated between AD 980-1030 with temperatures 0.7°C below the LMA. Varve-inferred summer temperatures increased from AD 1030-1620 to the LMA, though the period from AD 1260-1350 was 0.2°C below the LMA. Although there is no equivalent to the European Medieval Warm Period in the Blue Lake record, two warm intervals occurred from AD 1350-1450 and AD 1500-1620 (0.4 and 0.3°C above the LMA, respectively). During the

Little Ice Age (LIA; AD 1620-1880), inferred summer temperature averaged 0.2°C below the LMA. After AD 1880, inferred summer temperature increased to 0.8°C above the LMA, glaciers retreated, but aridity persisted based on a number of regional paleoclimate records. Despite warming and glacial retreat, varve thicknesses have not achieved pre-AD 730 levels. This may reflect limited sediment availability and transport due to a less extensive retreat compared to the first millennium, and continued relative aridity. Overall, the Blue Lake record is similar to varve records from the eastern Canadian Arctic that document a cool LIA and 20th century warming. However, the occurrence and timing of these, and other, events, such as the Medieval Warm Period, varies considerably among records, suggesting heterogeneous climatic patterns across the North American Arctic.

2.2 INTRODUCTION

Late 20th century and early 21st century Northern Hemisphere warming is unprecedented within the context of instrumental records (IPCC, 2007; Rigor et al., 2000). This is particularly true in the Arctic where temperatures have increased more rapidly than the hemispheric average (IPCC, 2007; Stafford et al., 2000). Glaciers across the Brooks Range have retreated dramatically (Ellis and Calkin, 1984; Evison et al., 1996; Rabus and Echelmeyer, 1998), while Arctic sea ice reached a record low in September of 2007 (Stroeve et al., 2008). These changes amplify climate change through cryosphere-atmosphere-ocean dynamics (Maslanik et al., 1996; Mysak and Venegas, 1998). Improving our knowledge of climate variability in the Arctic over the past several thousand years is essential to place the observed 20th century warming in a longer

context. To this end we present an annually resolved 2000-year-long varve record from a small glacial-fed lake located in the central Brooks Range of arctic Alaska.

2.3 STUDY AREA

Blue Lake (68.0869° N, 150.4650° W, 1275 m asl) is a small (0.04 km^2), shallow (4 m) glacial-fed lake located in the Oolah Valley of the central Brooks Range near Atigun Pass, just north of the North American Continental Divide (Fig. 1a, b). The watershed is small (4.1 km^2) and has a simple morphology. The drainage basin encompasses a 3.2-km-long valley with a single small glacier (0.07 km^2) in the north-facing cirque at the valley's head. The talus-covered cirque walls rise to a maximum headwall elevation of 1880 m asl. Summer meltwater from the glacier carries a substantial sediment load, as observed during July 2006, and flows unimpeded into Blue Lake at its north end (Fig. 1b, c).

The watershed lithology consists of sandstones and conglomerates of the Upper and Lower Kanayut (lower Mississippian and upper Devonian) interbedded with the red Kayak Shale (lower Mississippian) in the upper, glaciated part of the catchment (lower Mississippian; Kelly, 1990). The friable Kayak Shale is extremely susceptible to glacial erosion and is the primary sediment source for Blue Lake, unlike the more resistant sandstones and conglomerates. This is reflected in the striking reddish hue of the Blue Lake sediments (Fig. 2). The glacially eroded Kayak Shale effectively provides an inexhaustible supply of sediment to Blue Lake. Changes in varve thickness at Blue Lake, therefore, are interpreted as variability in the delivery of sediment to the lake as controlled by glacial runoff and snowmelt, and not sediment availability.

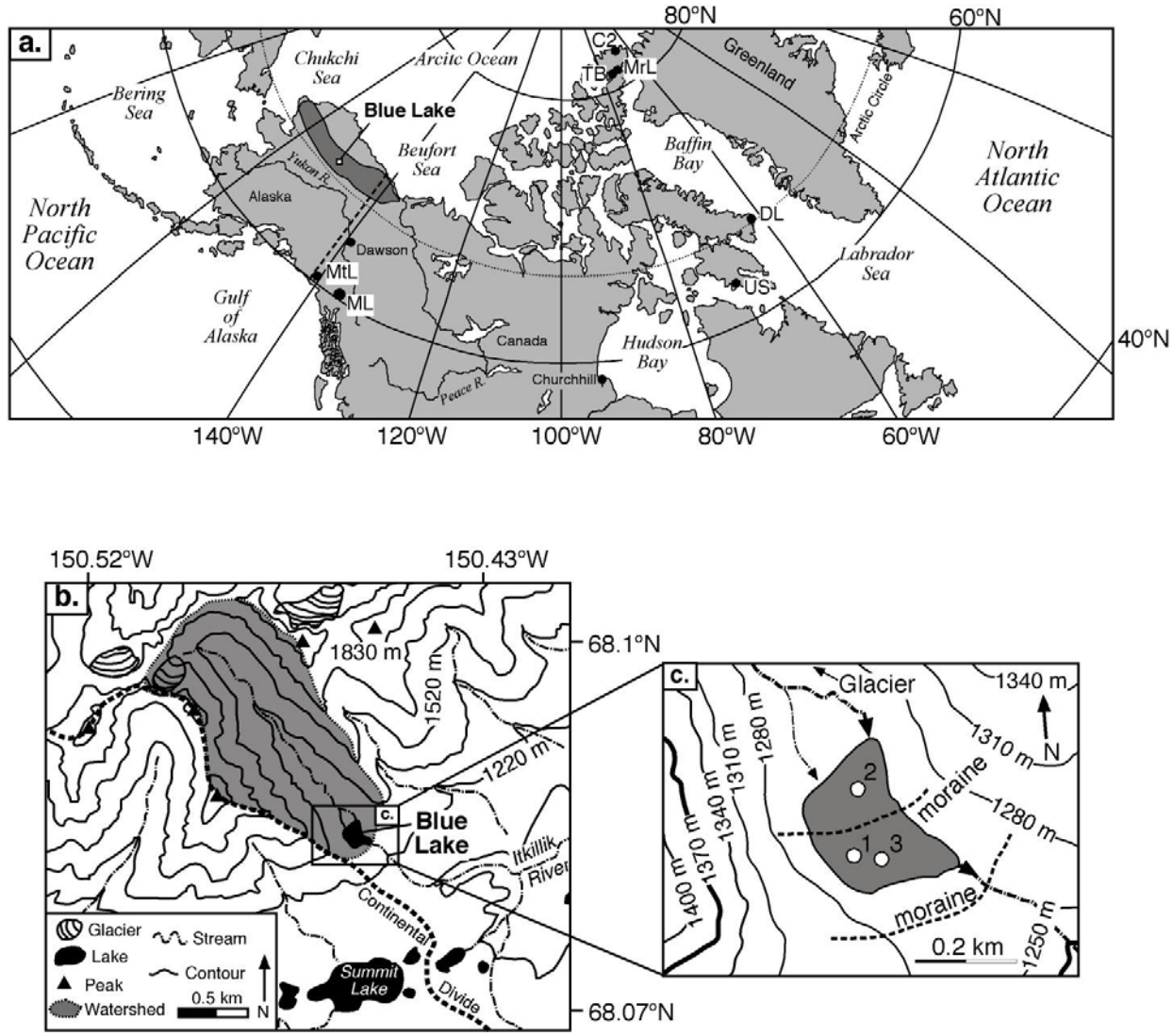

Figure 1 (a) Map of the North American Arctic showing Blue Lake (white box) in the Brooks Range (dark grey shaded area) and other records discussed in the text (MtL = Mt. Logan, ML = Marcella Lake, US = Upper Soper Lake, DL = Donnard Lake, TB = Tuborg Lake, MrL = Murry Lake, and lake C2). (b) Topographic map of the Blue Lake drainage basin (shaded grey with a dashed outline), and the Blue Lake glacier in the upper part of the watershed. (c) Blue Lake with core locations (Table 1).

Sediment accumulation rates in Blue Lake are an order of magnitude higher than in nearby lakes (Summit, Peanut, and Dumbbell) that are not glacially fed (Unpublished data). This reflects the abundant sediment available to Blue Lake. Unlike Blue Lake, the stratigraphy in nearby lakes is massive with occasional centimeter-scale bands. The mm-scale couplets in the

Blue Lake sediments are preserved due to rapid accumulation, despite an oxygenated water column. In addition, because the Kayak Shale is restricted to the upper most portion of the watershed where the glacier is, processes affecting this area are regarded as the most important in determining varve thickness.

Blue Lake is surrounded by moderately steep talus slopes (~35°) with a relatively flat area around the lake that shields it from direct rock fall and other mass wasting (Fig. 1b, c). The lake is divided into a shallower northern basin (~3 m) and a deeper southern basin (~4 m) by an east-west trending sill, likely a late-glacial moraine (Fig. 1c). This sill helps protect the southern basin from turbidity currents and turbulent flow, minimizing disturbances in the varves. Other moraines are located up valley, including a Little Ice Age moraine proximal to the present glacier margin (Sikorski et al. in press). No other moraine-dammed lakes are present in the watershed, and there is no evidence of temporary ponding or paleolakes that could have influenced sediment delivery to Blue Lake in the past. Vegetation surrounding the lake is tundra tussock grasses, mosses, and lichens.

2.4 CLIMATIC SETTING

The Brooks Range forms a physical boundary between the warmer, wetter Alaskan interior (mean annual temperature; MAT = 3.7°C, mean annual precipitation; MAP = 320 mm) and the cold, dry Arctic (MAT -12C, MAP 150 mm; Stafford et al., 2000). No climate data are available from the Blue Lake watershed. Temperature and precipitation trends for the lake, therefore, are inferred from the Natural Resources Conservation Service (NRCS) Snowpack Telemetry (SNOTEL) weather station at Atigun Pass (~41 km east of Blue at 1460 mASL; Abramovich and

Pattee, 1999). Temperature and precipitation data are available since AD 1993 and 1983, respectively. Since AD 1993, summer temperatures (June-July-August; JJA) have averaged 3.7°C, and winters (December-January-February; DJF) have averaged -14.8°C, with below-freezing temperatures September through May. The melt season, and therefore sediment input to the lake, is generally restricted to JJA when the lake is ice-free and above-freezing temperatures melt snow and glacial ice. Precipitation at Atigun Pass has averaged ~600 mm yr^{-1} since 1983 and is highly seasonal. Maxima occur from June through August (322 mm, 51% of MAP) with minima from November to April (150 mm, 24% of MAP).

2.5 METHODS

2.5.1 Core collection

A 1.8-m-long core (A-99) composed of two drives with 20 cm of overlap was collected in AD 1999 from the deepest part of Blue Lake (4 m) using a Livingstone square rod corer (Fig. 1c; Table 1; Wright et al., 1984). The sediment water interface was captured in core B-99, which was collected using an Aquatic Research percussion corer. Twelve additional cores, six long and six surface cores, were collected in July 2006 using a modified percussion piston corer with a 22.5 kg weight and an Aquatic Research percussion corer, respectively (Fig. 1c; Table 1; Nesje, 1992).

Table 1 Names, coring device, and length of the cores located in Figure 1c

Site	Core ID	Core Type	Length (cm)	Sediment Interface
1	A-99	Livingstone	180	Yes
	B-99	Surface	19	Yes
	A-06	Surface	40	Yes
	B-06	Percussion	254	No
	C-06	Percussion	325	No
	D-06	Surface	57	Yes
2	E-06	Surface	59	Yes
	F-06	Percussion	180	No
	G-06	Percussion	159	No
	H-06	Surface	75	Yes
3	I-06	Percussion	373	No
	J-06	Surface	78	Yes

2.5.2 Radiometric Age Control

Independent age control was established using ^{137}Cs, ^{210}Pb, and radiocarbon dating. Samples for ^{137}Cs and ^{210}Pb assays were collected at 0.5 cm intervals from core B-99 to a depth of 14 cm (Table 2). ^{137}Cs and ^{210}Pb activities were determined by gamma counting.

Table 2 Results of ^{210}Pb and ^{137}Cs assays from core B-99 shown in Figure 4

Depth (cm)	^{210}Pb Excess Bq/g	Error (+/-)	^{210}Pb Bq/g	Error (+/-)	^{137}Cs Activity (Bq/g)	^{137}Cs Bq/g Error (+/-)
0.25	9.79E-02		6.96E-03		1.46E-02	1.88E-03
0.75	8.16E-02		6.10E-03		1.40E-02	5.11E-04
1.25	5.67E-02		4.76E-03		1.66E-02	1.43E-03
1.75	2.40E-02		3.01E-03		1.61E-02	1.80E-03
2.25	2.48E-02		2.91E-03		1.70E-02	1.18E-03
2.75	2.72E-02		3.07E-03		1.64E-02	1.70E-03
3.25	2.92E-02		3.21E-03		2.12E-02	1.11E-03
3.75	3.25E-02		3.36E-03		2.98E-02	6.95E-04
4.25	2.08E-02		2.80E-03		3.32E-02	1.32E-03
4.75	2.07E-02		2.80E-03		5.21E-02	1.91E-03
5.25	2.18E-02		3.10E-03		1.05E-01	2.68E-03
5.75	2.10E-02		3.01E-03		6.36E-02	1.74E-03
6.25	2.52E-02		3.24E-03		3.19E-02	1.15E-03
6.75	1.65E-02		3.21E-03		4.37E-03	9.92E-04
7.25	1.63E-02		2.73E-03		0.00E+00	0.00E+00
7.75	1.13E-02		2.42E-03			
8.25	7.00E-03		2.01E-03			

Terrestrial macrofossils were isolated for AMS ^{14}C dating by sieving samples from five depth intervals (Table 3). Samples were cleaned and pretreated at the University of Pittsburgh Radiocarbon Laboratory following standard acid/alkaline/acid pretreatment protocols (Abbott and Stafford, 1996) and measured at the University of California Irvine Keck AMS Radiocarbon Laboratory. All ages are reported as the 2-sigma median age with uncertainties one half of the 2-sigma age range. Ages were calibrated to years AD/BC using the online software CALIB 5.0 (Reimer et al., 2004; Stuiver and Reimer, 1993). Ages determined from ^{137}Cs and ^{210}Pb profiles, and ^{14}C were stratigraphically extrapolated between cores based on similar varve patterns.

Table 3 Radiocarbon ages and related data for samples from Blue Lake, Alaska

CI #	Core	Core depth (cm)	Material	Fraction modern	^{14}C yr BP	Error (+/-)	2-Sigma calibrated age (AD/BC)	2-Sigma median calibrated age (AD/BC)	Median error (+/-)
37556	B-06	23.9	Terrestrial plant	0.9634	300	25	1511-1601 AD	1561 AD	45
37557	B-06	209.2	Terrestrial plant	0.6948	2925	20	1213-1045 BC	1130 BC	85
37635	C-06	95.3	Terrestrial plant	0.8478	1325	30	650-722 AD	680 AD	35
37636	C-06	283.5	Terrestrial plant	0.6172	3875	45	2470-2270 BC	2360 BC	100
37558	I-06	273.6	Terrestrial plant	0.6242	3785	25	2288-2140 BC	2220 BC	75

2.5.3 Thin-section preparation

Thin sections for detailed sediment fabric analysis were prepared using a resin-impregnation method (Francus and Asikainen, 2001; Hughen et al., 1996; Lamoureux, 1994). Undisturbed sediment was collected continuously down core with ~1 cm of overlap between sample sections to ensure that all couplets were represented. The sediment was flash-frozen in liquid nitrogen and immediately freeze-dried under high vacuum. Four-component Spurr low-viscosity epoxy resin was used to impregnate the sediment under low vacuum for 2 hours. After curing 48

additional hours at 50°C, the samples were cut into sub-sections at a 45° angle to ensure that no couplets were lost due to the thickness of the cutting blade. The final thin sections were prepared by Texas Petrographic Services, Inc.

2.5.4 Core imaging and couplet measurements

Couplet measurements were made from scanned thin-section images and high-resolution (20 to 30 pixels mm^{-2}) digital images of core surfaces. Thin sections were scanned using a standard desktop flat-bed scanner with a resolution of 2400 dots per inch. Digital images were acquired using a line-scanning system with polarized full-spectrum fluorescent lights in a fixed position with respect to the cameras for consistent lighting of the core surface. The final color-calibrated images and scanned thin sections were imported into Adobe Photoshop 7.0 where the couplets were measured following Francus et al. (2002a). Some sediment disturbance in the form of bowed couplets occurred as a result of the coring process (Fig. 2b, c). To maximize accuracy and consistency, the couplets were measured at the apex of the bowed sediments (Fig. 2b).

Scanning electron microscope (SEM) images of the thin sections were made at the University of Pittsburgh SEM Laboratory using a Philips XL-30 field emission SEM equipped with detectors for imaging in secondary electron (SE) and backscatter electron (BSE) modes.

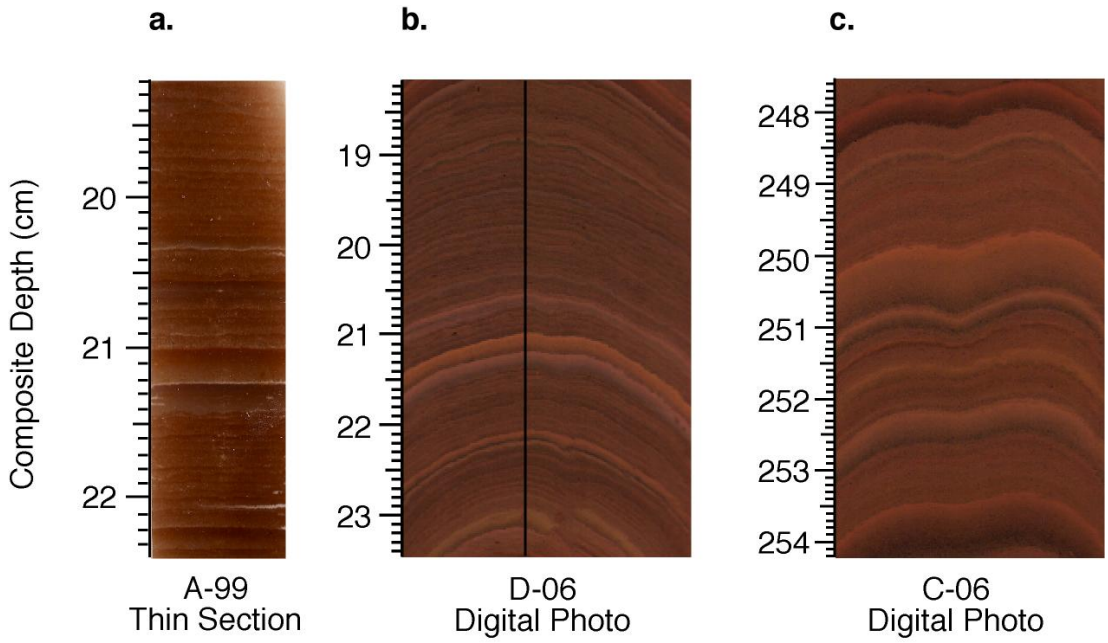

Figure 2 (a) Thin section photomicrograph from core A-99 showing the fine laminations characteristic of the varved sediments during the Little Ice Age. The lighter layers are the clay caps that overlie the darker silty portion of the varves. (b) High-resolution digital photograph of surface core D-06 showing the same interval represented by the thin section in part (a). The black line designates where the couplets were measured. (c) Image of core C-06 from the lower portion of the core (below 100 cm) where varve thickness increases. Note that the color and structure of the varves are the same as in (a) and (b), only thicker.

2.6 RESULTS

The Blue Lake varve data reported in this study are available online at the World Data Center for Paleoclimatology (ftp://ftp.ncdc.noaa.gov/pub/data/paleo/paleolimnology/northamerica/usa/alaska/blue2008.txt).

2.6.1 Sedimentology

The sediments in Blue Lake are finely laminated to bedded couplets of inorganic glacially-derived siliciclastics. Throughout the core, the couplets are made up of dark reddish-brown silt (5YR 4/3) capped by lighter tan clay (5YR 5/4), and range from 0.17 to 10.78 mm (Figs. 2, 3). Couplets are present throughout the core, indicating continuous rhythmic deposition. SEM photographs of thin sections show that the transition between the coarse basal layer and fine cap is abrupt, not graded, indicating these they were formed by discrete depositional events without sub-layers within the lower couplet that typically mark varves impacted by precipitation events (e.g. Lamoureux et al., 2001).

A sustained decrease in the mean couplet thickness occurs above ~100 cm depth (Fig. 4d, 5). The physical features of the couplets (i.e. grain size, texture, color) do not change, however,

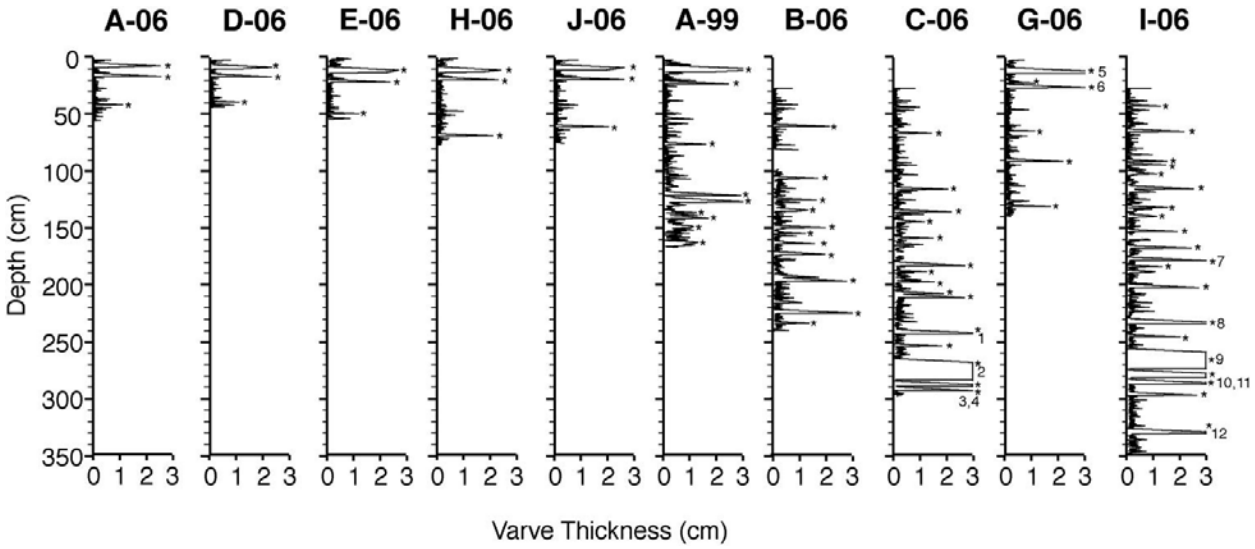

Figure 3 Varve thickness measurements from the network of cores from Blue Lake plotted by depth. Despite subtle differences, the varves have similar thicknesses and downcore thickness patterns across the lake. Layers identified as turbidites are designated with an astrix (*). The values are truncated in order to show the finer varves. Thicknesses of the clipped varves are reported in Table 4.

suggesting that the couplets below ~100 cm are formed by similar sedimentological processes as those above 100 cm (Fig. 2b, c). These couplets are therefore considered varves and included in the varve chronology.

Twenty-one anomalously thick layers, ranging from 1.10 to 18.14 cm thick were also identified in the cores (Fig. 3). Based on sedimentological characteristics (i.e. presence of graded bedding) the layers were identified as turbidites and excluded from the thickness record and varve chronology.

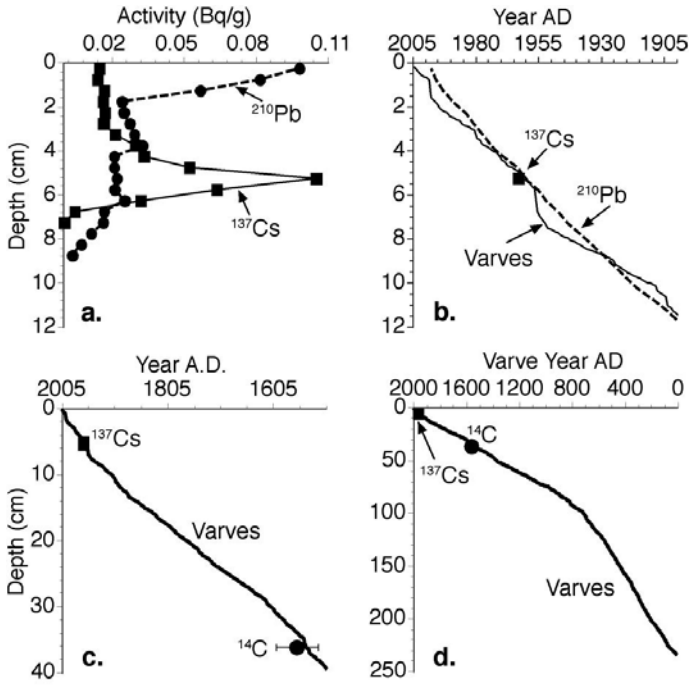

Figure 4 (a) ^{210}Pb (circles) and ^{137}Cs (squares) activity profiles in core B-99 (Table 2). (b) Geochronology results from ^{137}Cs (square) and ^{210}Pb (dashed line) analyses plotted with the age-depth model derived from varve counting (solid line). (c) ^{137}Cs assays (black square) are plotted with the AMS ^{14}C age (black circle; Table 3) and the age-depth model determined from varve counting (black line). The strong agreement between the ages based on varve counting and those from radiometric dating techniques support the conclusion that the couplets in the Blue Lake cores are deposited annually. (d) The complete varve derived

age-depth model (black line) with ^{137}Cs (square) and ^{14}C (circle) measurements. Note the change in sedimentation rate at 730 AD.

2.6.2 Radiometric age control

2.6.2.1 *^{137}Cs and ^{210}Pb*

^{137}Cs and ^{210}Pb results are in agreement with ages determined from couplet counting (Fig. 4a, b; Table 2). The AD 1963 ^{137}Cs peak occurs between 5.0 and 5.5 cm, the same depth interval that contains the AD 1963 couplet as determined by couplet counting. ^{210}Pb shows a general exponential decrease with depth, though with much variability, suggesting varying sedimentation rates. The linear ^{210}Pb age model estimates the age of the ^{137}Cs peak within four years of the expected date of AD 1963.

2.6.2.2 *^{14}C*

One AMS ^{14}C age (UCI 37556; 1560 +/- 45 AD) agrees well with those from couplet counting (Table 3; Fig 4c, d). This age was measured on terrestrial vegetation collected from an interval of typical and undisturbed couplets. The age of the couplet is AD 1543 based on couplet counts, well within the AMS ^{14}C age range (Fig. 4c). The other four ages are older than expected from couplet counting and not in stratigraphic order (Table 3). These samples were collected from layers that were later identified as turbidites. We suspect that these ages were measured on reworked vegetation fragments that were washed into the lake during flood events. The ages were therefore discarded.

^{137}Cs, ^{210}Pb, and AMS ^{14}C results support the interpretation that the sediment couplets in Blue Lake are varves (Fig. 4b-d). We therefore use ages determined by varve counting (one couplet = one year) for our age model (Fig. 4d).

2.6.3 Varve Chronology

Varves were measured at least three times on cores used in the chronology to ensure data quality and consistency. We estimate an approximate 1% cumulative error based on replicate counts; however, couplets incorrectly identified as varves or indistinguishable varves have an

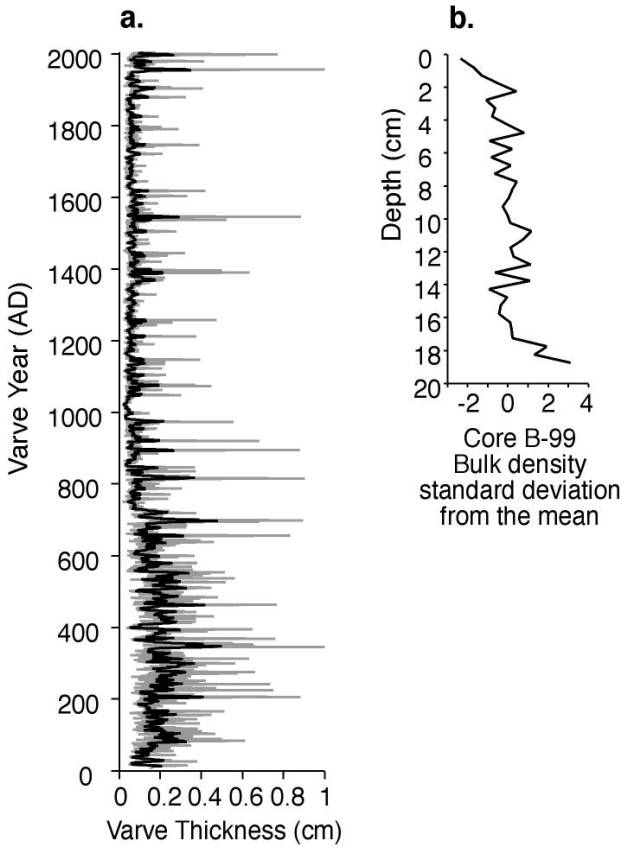

Figure 5(a) Composite varve-thickness measurements from Blue Lake. The black line is a 5-point moving average; grey line is the annual values. (b) Bulk density from core B-99 shown as the standard deviation from the mean. Bulk density values are within 1σ from the mean at 1.5 cm, indicating that increasing varve thickness at the top of the core are not an artifact of uncompacted sediments.

unquantifiable impact on the chronology. We used four cores to develop the chronology; additional cores could help refine the age model and reduce potential chronological errors.

Analyses of multiple surface and long cores from different parts of the lake show consistent depositional patterns (Fig. 3). Slight variations in couplet thicknesses among cores may reflect subtle differences in accumulation due to sediment focusing or disturbances during the coring process. Overall, the entire lake responds coherently to the seasonal influx of sediment as indicated by the consistency of individual varve thicknesses among cores.

We created a composite varve chronology using cores with the least-disturbed sediments and easily identifiable couplets (Fig. 5a). Surface cores D-06 and H-06 were used for the upper section, core C-06 was used for the main body, and a ~10 cm section from core I-06 was used to bridge a 3.5 cm gap in core C-06, where it was cut in the field for transport.

2.6.4 Varve thickness trends

Varves in Blue Lake are thickest between AD 10-730, averaging 1.89 mm with a maximum of 10.26 mm and a minimum of 0.33 mm (Fig. 5a). After AD 730, varve thicknesses and sedimentation rates decrease abruptly (Fig 4d, 5). Two shifts from AD 730-850 (average = 0.99 mm) and from AD 850-980 (average = 0.84 mm) mark the transition to a 50 year period of very thin varves between AD 980-1030 (average thickness = 0. 41 mm). From AD 1030-1620, varves average 0.76 mm, reach a maximum of 8.84 mm, and a minimum of 0.20 mm in thickness. Another period of thin varves occurs between AD 1620-1880, where they average 0.62 mm and have a maximum and minimum of 3.89 and 0.21 mm, respectively. Varve thickness increases from AD 1880 to the present, averaging 1.05 mm with a maximum of 10.78 mm and a minimum of 0.19 mm. Increased varve thickness after AD 1880 is not due to reduced compaction. The

bulk density of sediment from core B-99 reaches average values by 1.5 cm depth (Fig. 5b). Furthermore, the surface cores collected in AD 2006 were allowed to dewater in the field over several days to ensure that the uppermost sediments were not disturbed during transport. Therefore, the uppermost sediments settled and had low water content when varve thicknesses were measured.

2.7 DISCUSSION

2.7.1 Varve thickness and the instrumental record

Varve-thickness records from glacial-fed lakes in the Arctic are often interpreted in terms of summer temperature because warmer summers result in higher discharge of sediment-laden melt-water from glaciers and snow melt (e.g. Hardy, 1996; Moore et al., 2001). However, several studies demonstrate that other factors, such as extreme precipitation events, can play an important role in varve formation for certain climatic and geomorphic settings (Cockburn and Lamoureux, 2007; Lamoureux, 2000; Lamoureux et al., 2001). This typically results in varves with multiple summer sub-layers representing major rain events and large numbers of thick turbidites, neither of which are observed in the Blue Lake sediment. Additional factors, including glacial, fluvial, geomorphic, terrestrial-biologic, and inter-basin processes, have also been shown to influence varve formation (e.g. Hodder et al., 2007). We believe that the oligotrophic status of Blue Lake combined with the simple basin morphology and high accumulation rate greatly limits the influence these additional factors.

At Blue Lake our ability to discern the relative contributions of climatic and internal processes is limited by the availability of modern observations and instrumental meteorological data. We therefore restrict our analysis to comparison with data from the NRCS SNOTEL station at Atigun Pass, the nearest available instrumental record. The statistical relationship between varve thicknesses and meteorological data was assessed using linear regression (Fig. 6a, b; Table 4).

Average JJA temperature and varve thicknesses between AD 1993 and 2005 show a weak positive relationship when all the data are considered ($r^2 = 0.02$, $p = 0.65$; Fig. 6a; Table 4). With one anomalous year, AD 1998, removed from the varve series, the correlation improves ($r^2 = 0.28$, $p = 0.10$; Fig. 6a; Table 4). Anomalous deposition during AD 1998 may reflect an isolated extreme precipitation event or some other intra-basin, non-climate-related event. A log transformation of the varve-thickness and temperature data further improves the varve-temperature relationship ($r^2 = 0.31$, $p = 0.08$; Fig. 6a; Table 4). This suggests a nonlinear relationship between spring/summer melt, sediment transport, and temperature, in which small changes in temperature are amplified within the sedimentary system. Similar logarithmic relationships have been observed in other glacial-fed Arctic and alpine lakes (Hardy, 1996; Leemann and Neissen, 1994; Leonard, 1985). Summer precipitation and varve thickness show no statistically significant relationship, regardless of whether or not the AD 1998 varve is removed from the time series (Fig. 6b; Table 4). This suggests that summer precipitation is not a significant factor in varve formation during the period represented by the instrumental record.

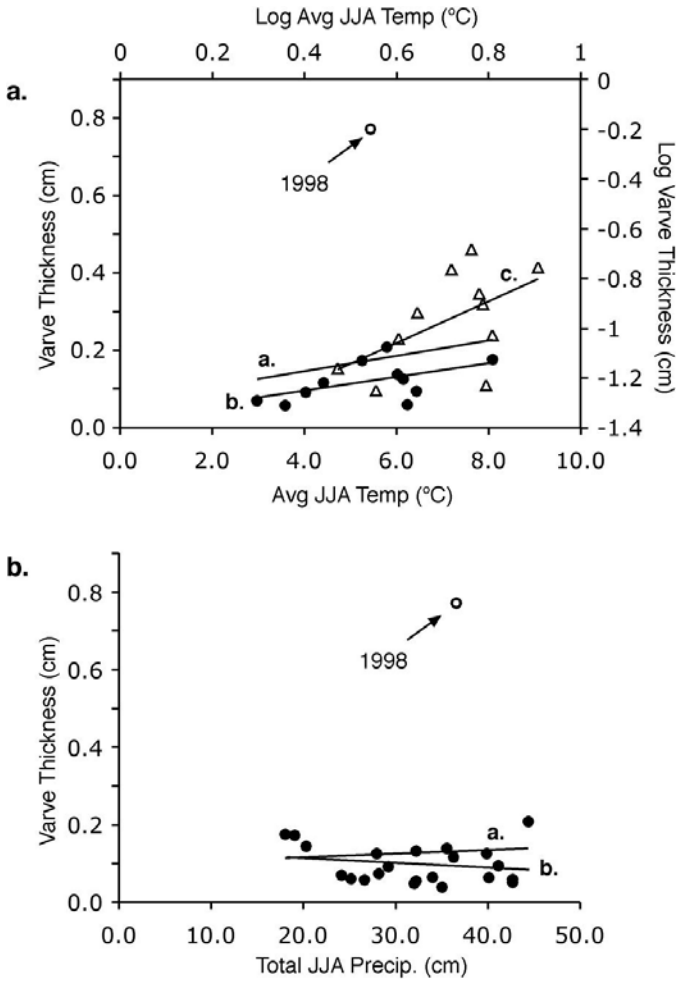

Figure 6(a) Varve thickness plotted against average JJA temperatures from Atigun Pass (AD 1993-2005; black circles). The correlation between varve thickness and temperature is poor when all the data are considered (line a; $r^2 = 0.02$; $p = 0.65$). With AD 1998 removed, the correlation between varve thickness and temperature is significant at the 90% confidence interval (CI; line b; $r^2 = 0.28$; $p = 0.1$). Also plotted are the log-transformed varve-thickness data and average JJA Atigun Pass temperatures (open triangles) with AD 1998 excluded. The log-transformed data show a better correlation ($r^2 = 0.31$; $p = 0.08$; 92% CI; line c). (b) Varve thickness plotted against total JJA precipitation at Atigun Pass (AD 1983-2005). The correlation between varve thickness and precipitation is statistically insignificant (line a; $r^2 < 0.01$; $p = 0.82$), even with AD 1998 removed (line b; $r^2 = 0.04$; $p = 0.38$). The linear regression equations and statistics are located in Table 5.

Table 4 Values of truncated varve thicknesses in Figure 3

Core	Varve #	Thickness (cm)
C-06	1	4.0
	2	18.2
	3	4.7
	4	3.1
G-06	5	4.4
	6	3.2
I-06	7	3.3
	8	4.6
	9	16.8
	10	6.7
	11	4.5
	12	4.2

Although not significant at the conventional 95% confidence interval (CI; $p = 0.05$), the log-transformed varve-temperature relationship is significant at the 92% CI. The results indicate that 31% of varve thickness in Blue Lake is explained by temperature at Atigun Pass since AD 1993. The remaining component of varve thickness not related to Atigun Pass temperature may be attributable to differences in temperature between the two sites or additional factors, such as variable winter precipitation, the intensity of snowmelt, or other intra-basin processes.

The limited duration of the instrumental record is the greatest source of uncertainty in our varve-temperature calibration. Temperatures inferred from varve thicknesses that are beyond the range of those in the calibration period are subject to greater error. A longer calibration period that incorporates the full range of observed varve thicknesses would help improve the varve-temperature relationship and the model's predictive ability. Monitoring intra-basin and glacial processes, including glacier discharge and sedimentation dynamics, would further help to quantify the relative contributions of various influences on varve formation at Blue Lake, and thus improve the varve-climate model.

Given the limited process data from Blue Lake, and the significant correlation between varve thickness and average JJA temperatures, we propose a simple interpretive model of varve

thickness in which increased (decreased) sediment transport and subsequent deposition in Blue Lake is the result of enhanced (diminished) glacier-ice and snowmelt during warmer (cooler) summers. We recognize that the extent to which summer temperature controls varve thickness may have changed through time, especially during different climate states (Blass et al., 2007). Therefore, we strongly advocate caution when extrapolating this relationship downcore, but given the high quality and temporal resolution of the Blue Lake sedimentary sequence, interpret its climatic implications.

2.7.2 Temperature reconstruction

Keeping in mind the limitations of the varve-temperature relationship, we used least-squares regression of the log-transformed data to estimate JJA temperatures from AD 730-2005 (Fig. 7; Table 5). The period from AD 10-730 is excluded from the reconstruction because varve thicknesses during this interval are well beyond the range of the calibration data, and because previously published paleoclimate studies from elsewhere in the region suggest that temperature may not have been the dominant control on varve thickness prior to AD 730 (discussed below). The temperature reconstruction was smoothed with a 51-year moving average to reduce the 'noise' from non-climate-related events and to highlight long-term summer temperature trends (Fig. 7).

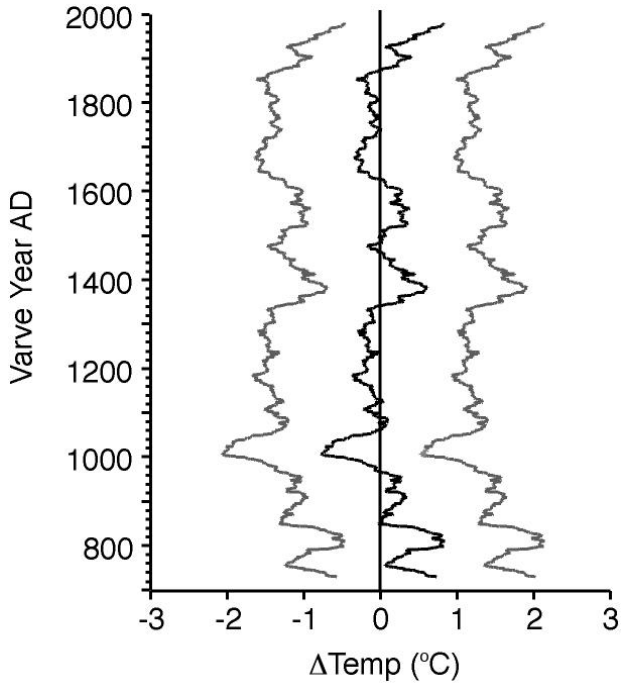

Figure 7 Blue Lake temperature reconstruction (black solid line) with the upper and lower 95% confidence intervals (grey lines) shown as the deviation from the last millennium average (4.2°C). The temperature reconstruction is derived for the period AD 730-2005. Temperatures prior to AD 730 are not reconstructed because varve thicknesses during this time are well beyond the range of the calibration period, reducing confidence in the results. We also suspect that increased varve thickness during this period reflects the role of enhanced precipitation on varve formation (see text for discussion).

Table 5 Regression statistics for the relationship between varve thickness at Blue Lake and annual climate data from Atigun Pass

Variable	Time period AD	Years excluded	Line[2]	Regression equations	r^2	p
JJA Avg.	1993 to 2005	1996[1]	a.	Temp = 5.185 + 1.065(Thickness)	0.02	0.65
Temp (°C)	1993 to 2005	1998	b.	Temp = 3.528 + 15.49(Thickness)	.28	0.10
Log JJA Avg. Temp (°C)	1993 to 2005	1998	c.	Log[Temp] = 1.0676 + 0.3677 (Log[Thickness])	0.31	0.08
JJA Total	1983 to 2005	None	a.	Precip = 31.987 + 2.67(Thickness)	< 0.01	0.82
Precip (cm)	1983 to 2005	1998	b.	Precip = 35.295 - 32.322(Thickness)	0.04	0.38

[1] JJA temperature data are incomplete for 1996 AD and so are not included in any of the temperature correlations
[2] See Figure 6 for regression lines

Despite the sparse calibration data, the Blue Lake JJA temperature reconstruction shows similarities with other paleo-temperature estimates from the Brooks Range (Ellis and Calkin, 1984; Jacoby et al., 1999). Our reconstruction indicates that the Little Ice Age (LIA) was 0.2°C below the last millennium average (AD 1000-2000; LMA = 4.2°C). This is equivalent to 0.6 to 1.0°C cooler than modern, depending on the reference period used (1880-2005 AD average = 4.7°C or AD 1950-2005 average = 5.1°C, respectively). Similar estimates were derived from tree-ring studies by Jacoby et al. (1999) and lake-based studies by Clegg et al. (2005), which suggest a 0.6°C and 1.5 to 2°C LIA cooling, respectively. Ellis and Calkin (1984) suggested a 1°C or 3-4°C LIA cooling based on environmental lapse rate calculations and glaciologic-meteorologic measurements in the Brooks Range between AD 1977 and 1988. However, this reference period was unusually warm, so the upper end of these estimates is likely too high. While we recognize the uncertainty in our reconstruction, the similarities with independent temperature estimates is encouraging, suggesting that changes in varve thickness at Blue Lake capture general summer temperature trends.

The temperature reconstruction presented in the discussion uses the LMA as the reference period. All JJA temperature estimates are inferred from varve thicknesses, unless otherwise stated, and shown as the difference from the LMA (ΔT). Temperatures above the LMA are denoted with a positive sign (+), while temperatures below the LMA are denoted with a negative sign (-).

2.7.3 Regional paleoenvironmental records

To aid in the interpretation of the Blue Lake varve-thickness and inferred-temperature trends, comparisons were made with previously published paleoenvironmental records from the region (Fig. 8a-d). The chronology of glacier fluctuations in the central Brooks Range is based on the number of moraines of particular ages as determined by lichenometric and radiocarbon dating (Fig. 8c; Calkin and Ellis, 1980; Ellis and Calkin, 1984). Hydrologic variability in the Yukon is inferred from several $\delta^{18}O$ isotope records (Anderson et al., 2007; Blotzer et al., 2008). Marcella Lake (Anderson et al. 2007) is presented as a representative record of hydrologic change in the Yukon since trends in this lake are similar to those observed in other Yukon lakes, suggesting a regionally coherent hydrological response (Fig. 8d; Blotzer et al. 2008). Marcella Lake is a closed-basin lake with authigenic carbonate sediments located in the southern Yukon near the British Columbia border. The lake is evaporatively enriched with respect to meteoric $\delta^{18}O$ so that isotopic shifts reflect changes in precipitation and evaporation (P/E balance). Accordingly, positive (negative) values reflect drier (wetter) conditions.

2.7.4 AD 10 to 730: first millennium wet period

Varves are thickest in Blue Lake between AD 10-730 (Fig. 8a), implying that this was the warmest period of the last 2000 years, assuming that varve thickness is predominantly related to temperature. During the same interval, Ellis and Calkin (1984) identified the most sustained glacial retreat in the Brooks Range since the onset of Neoglaciation at ~5000 yr BP (Fig. 8c).

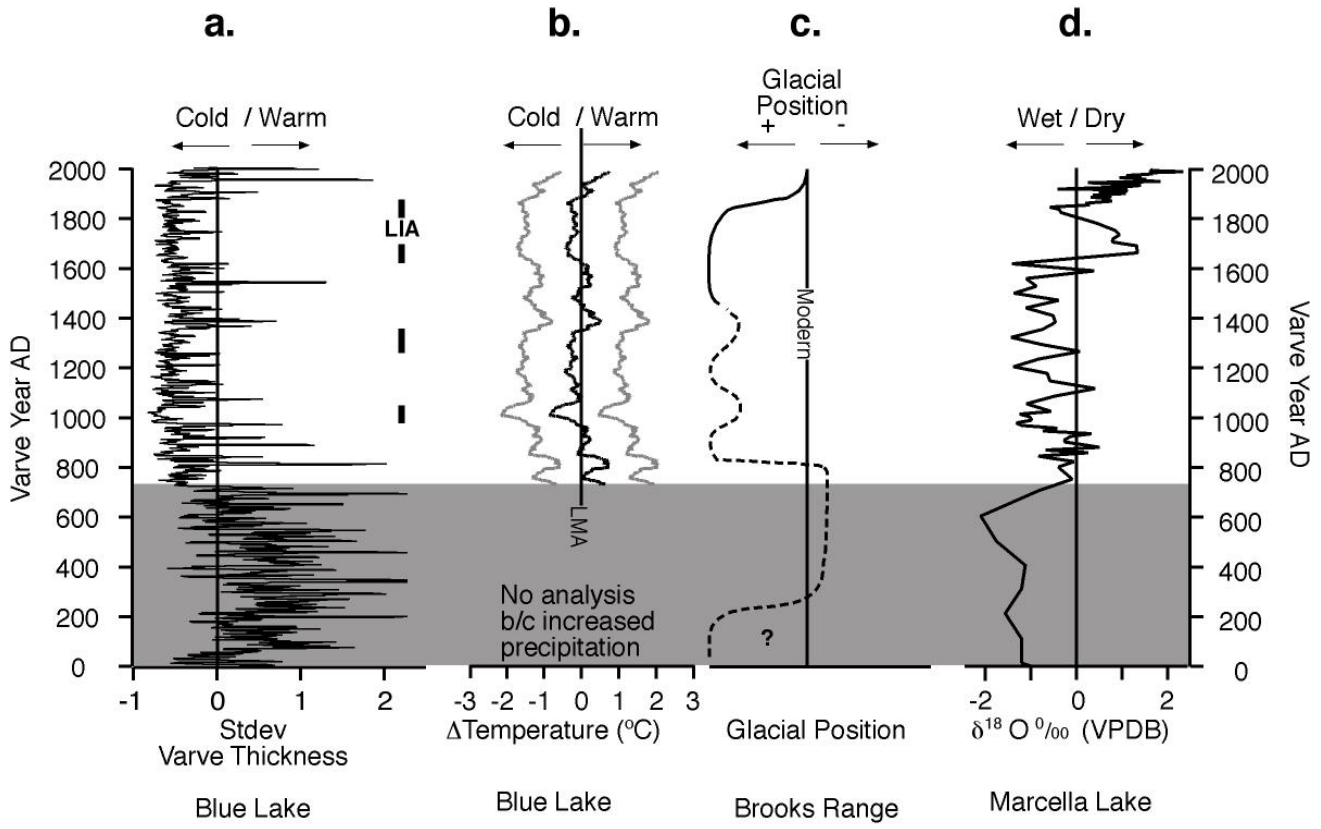

Figure 8 (a) Blue Lake varve thicknesses plotted as the standard deviation from the mean thickness (5-point moving average). Black vertical bars indicate inferred cool intervals in the Brooks Range. (b) Blue Lake temperature reconstruction shown as the difference from the last millennium average (51-point moving average) with the grey lines denoting the upper and lower 95% CI. (c) Glacier fluctuations in the Brooks Range (Ellis and Calkin 1984). (d) Greater Yukon aridity as represented by the Marcella Lake $\delta^{18}O$ record (Anderson et al., 2007). The grey box highlights the period during which precipitation, rather than summer temperature, is believed to have dominated varve formation in Blue Lake.

Though recessed, many cirque glaciers remained in the Brooks Range (Ellis and Calkin, 1984). Together, these records support the occurrence of a warm interval from 10-730 AD. However, isotopic evidence from the Yukon strongly indicates that this same period was the wettest in the last 2000 years. $\delta^{18}O$ values from Marcella Lake are persistently -1 to -2‰, the lowest values during the late Holocene, indicating wet conditions (Fig. 8d). Lake-level reconstructions from Marcella Lake also support a first millennium wet phase, showing contemporaneous high lake levels (Anderson et al., 2005).

We suspect that increased precipitation during this period of glacier recession influenced varve thicknesses at Blue Lake. With the Blue Lake glacier recessed, large amounts of unconsolidated sub-glacial sediment would have been exposed in the upper reaches of the catchment and subsequently available for transport. We suggest that enhanced sediment availability, in combination with increased precipitation, amplified sediment delivery to Blue Lake, resulting in thicker varves that were not directly related to temperature controlled summer melt. This inference is supported in part by higher sedimentation rates from AD 10-730 (Fig. 4d).

2.7.5 AD 730 to 1620: late Neoglacial cooling

Varve thickness and sedimentation rates in Blue Lake decreased abruptly after 730 AD (Fig. 8a). Contemporaneously, glaciers in the Brooks Range advanced (Ellis and Calkin 1984) and Marcella Lake $\delta^{18}O$ values increased (Fig. 8c, d; Anderson et al. 2007). These trends indicate an abrupt regional shift to colder and drier conditions. With an expanded Blue Lake glacier, previously exposed unconsolidated sediment would no longer have been available to summer hillslope runoff, reducing sediment delivery to the lake. We propose that glacial processes and

snowmelt influenced by summer temperature became the dominant influence on Blue Lake varve thickness at this time, establishing the varve-temperature relationship.

After AD 730, varve thicknesses declined in two steps between AD 730-850, and AD 850-980. Estimated JJA temperatures averaged +0.4°C and +0.1°C for these periods, respectively (Fig. 8a, b). Varve thicknesses abruptly decreased again after AD 980, and remained low for a 50 year period until AD 1030, indicating an abrupt and severe cold event with estimated JJA temperatures averaging -0.7°C (Fig. 8a, b).

From AD 1030-1620, JJA temperatures averaged the LMA, except between AD ~1260-1350 when JJA temperatures averaged -0.2°C. Although there is no distinct interval at Blue Lake that corresponds with the European Medieval Warm Period (MWP; AD 1000-1300; Crowley and Lowery, 2000), two periods of relative warmth occurred from AD 1350-1450 and AD 1500-1620 with average temperatures of +0.4°C and +0.3°C, respectively (Fig. 8b).

2.7.6 AD 1620 to 1880: the Little Ice Age

Although cold overall (average -0.2°C), inferred temperatures during the LIA were variable (Fig. 8a, b). The coldest phase of the LIA occurred between AD 1620-1720, with average JJA temperatures of -0.3°C (Fig. 8b). Warming between AD ~1720-1800, with temperatures averaging the LMA, was followed by a 0.2°C cooling from AD 1800-1850. After AD 1850, JJA temperatures increased to the LMA between AD 1850-1950 and rose to +0.8°C by AD 1950-2005 (Fig. 8b). As previously discussed, LIA temperature estimates appear reasonable as they are consistent with other independent temperature reconstructions (Ellis and Calkin 1984; Jacoby et al. 1999; Clegg et al. 2005).

During the LIA, the number of moraines formed in the Brooks Range reached a maximum, indicating a cool period when glaciers stabilized in advanced positions (Fig. 8c; Ellis and Calkin 1984). The lowering of equilibrium-line altitudes during the LIA (ΔELA) across the Brooks Range was minimal, however, suggesting decreased winter precipitation limited extensive glacier growth (Sikorski et al., In Press). This is in contrast to Clegg et al. (2005) who suggest increased winter precipitation during LIA based on $\delta^{18}O$ measurements from Takahula Lake in the southern Brooks Range. However, LIA aridity is also suggested for the Yukon by highly enriched $\delta^{18}O$ values from Marcella Lake and other lakes in the region, as well as by increased salinity in Lake U60 (Fig. 8d; Anderson et al., 2007; Blotzer et al., 2008; Pienitz et al., 2000).

Despite some evidence for aridity in Alaska during the LIA, other studies suggest the LIA experienced enhanced precipitation. Hu et al. (2001), for example, concluded that the LIA was a period of increased effective moisture at Farewell Lake in the northwestern Alaska Range. However, arid conditions appear to characterize the early LIA at Farewell Lake, compared to more humid conditions at ~AD 1700 toward the end of the LIA. This pattern of early LIA aridity followed by decreasing, but still arid, conditions is similar to that observed in the Marcella Lake $\delta^{18}O$ record (Fig. 8d; Anderson et al. 2007). Mann et al. (2002b) also concluded that conditions were wetter during the LIA based on an inferred reduction of dune activity at the Great Kobuk Sand Dunes. The dune field is ~375 km southwest of Blue Lake (~115 km east of the Chukchi Sea) on the southern foot hills of the Brooks Range between 60 to 80 m asl. Climatic conditions at this location may be influenced by its proximity to the Chukchi Sea and low elevation, and therefore may not reflect high-elevation conditions in the Brooks Range.

Together, these data show a regionally consistent trend in cooler temperatures during the LIA, but a complex hydrological response. Additional records of LIA hydrologic variability from the greater Alaska and Yukon regions are needed to address the spatial expression of LIA precipitation for this region.

2.7.7 AD 1880 to 2005: post-Little Ice Age warming

Increasing varve thicknesses after AD 1880 is consistent with post-LIA warming (Fig. 8a). This period is marked by glacier retreats in the central Brooks Range approaching the extent of the first millennium retreat (Fig. 8c, Ellis and Calkin 1984). Despite a ~1.0°C (+0.8°C from the LMA) temperature increase and widespread glacier retreat, varve thicknesses have not achieved pre- AD 730 levels (Fig. 8a, b). At first glance, this suggests that the 20th century may not be as great as pre-AD 730 warming; however, we suggest that varve thickness did not increase dramatically following the LIA because effective moisture did not increase to its pre- AD 730 level. As well, the Blue Lake glacier retreat may not yet be as extensive as the first millennium retreat, thereby limiting the excess sediment available to Blue Lake.

Aridity in the Yukon after AD 1880 is evidenced by increasing $\delta^{18}O$ values from Marcella Lake (Fig. 8d; Anderson et al. 2007). A major post-LIA shift is also noted in the Mt. Logan Prospector Col $\delta^{18}O$ ice-core record from the southwestern Yukon at ~AD 1850 (Fisher et al., 2004). This shift is interpreted as an increase in meridional atmospheric circulation and a strengthened/eastward Aleutian Low that is a response to warmer sea surface temperatures in the tropical Pacific and along the western coast of North America (Fisher et al. 2004). Such circulation results in increased precipitation over the coastal mountain ranges of Alaska, and decreased precipitation in interior regions because of the rain shadow effect from the coastal

Alaskan ranges (Stafford et al., 2000). The effects of this circulation change have been observed in the instrumental record of precipitation in northern Alaska, where precipitation has steadily decreased during the last 50 years (Stafford et al., 2000). These results support the idea that the increase in varve thickness at Blue Lake after AD 1880 is the result of increased temperature in the absence of increased precipitation.

2.7.8 Comparisons with Arctic basin records

Comparison of the Blue Lake varve record with varve records from the eastern Canadian Arctic show variable relationships (Fig. 1, 9). As with the Blue Lake record, varve records from the eastern Canadian Arctic are interpreted in terms of melt season temperatures, with thicker varves corresponding to warmer melt season temperatures. Varve-thickness trends between Blue Lake, Donnard Lake (Baffin Island; Moore et al., 2001) and Murray Lake (Ellesmere Island; Besonen et al., 2008) do not show a consistent phase relationship (Fig. 9a-c). For instance, the LIA at Donnard Lake began ~AD 1375, much earlier than the inferred AD 1620 onset at Blue Lake, although there is evidence for glaciation at Blue Lake during this time, and in Murray Lake, the onset of the LIA was later (~AD 1700) compared to Blue Lake. Prior to the LIA, Murray Lake and Donnard Lake show a pronounced interval of thicker varves that is contemporaneous with the European MWP (~AD 1100-1375). An equivalent period is not observed at Blue Lake (Fig. 9). Despite these differences, Blue Lake compares well with the shorter records from Lake C2 (Ellesmere Island; Hardy, 1996), Tuborg Lake (Ellesmere Island; Smith et al., 2004), and Upper

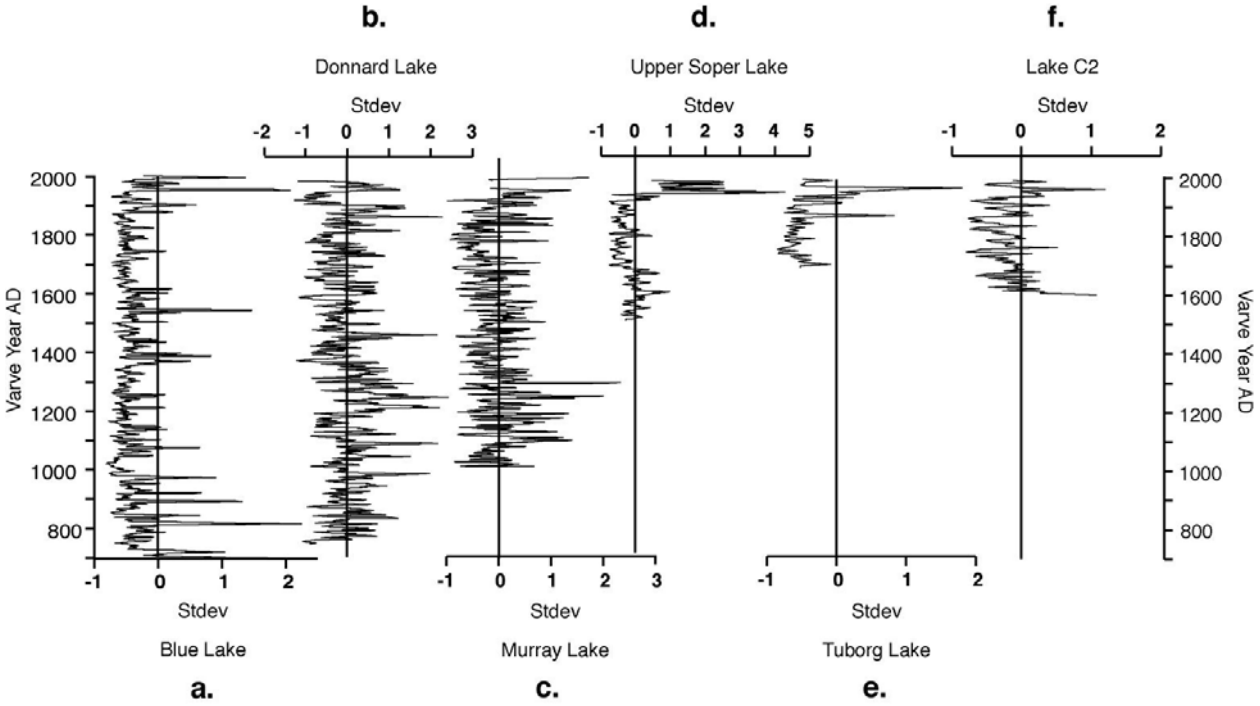

Figure 9 The 5-point moving average of normalized Blue Lake varve thicknesses compared with normalized 5-point moving average varve records from the eastern Canadian Arctic. (a) Blue Lake, (b) Donnard Lake, (c) Murray Lake, (d) Upper Soper Lake, (e) Tuborg Lake, and (f) Lake C2. The Blue Lake record is similar to Upper Soper Lake, Tuborg Lake, and Lake C2, showing a distinct and similarly phased LIA and post-LIA warming. The timing and magnitude of events at Blue Lake do not match Donnard Lake and Murray Lake as clearly. The locations of the Canadian lakes is shown in Figure 1a.

Soper Lake (Baffin Island; Fig. 9a, d-f; Hughen et al., 2000), which all show a cool LIA followed by 20th century warming. These relationships illustrate that the North American Arctic may not respond uniformly to climate change during the late Holocene. However, post-LIA warming appears to be consistent in these two regions.

2.8 SUMMARY

The Blue Lake varve-thickness record is the first annually-resolved reconstruction of summer climate from northern Alaska spanning the last 2000 years. The Blue Lake watershed and depositional system are relatively simple, adding confidence to varve-based paleoenvironmental investigations. Though modern instrumental climate data are temporally limited, Blue Lake varve thickness correlates well with temperature data from the nearest weather station at Atigun Pass. With the limitations imposed by a short calibration data set in mind, we used this correlation to infer summer (JJA) temperatures at Blue Lake from AD 730 to the present. Together with regional paleoenvironmental records, the Blue Lake varve-thickness record shows that the Brooks Range was warm and wet between AD 10 and 730. Glacial recession during this time likely exposed unconsolidated sub-glacial sediments that were subsequently mobilized by enhanced summer precipitation. Because influences other than temperature appear to have affected varve formation, temperatures were not estimated for this period.

The abrupt decrease in varve thickness at AD 730 was accompanied by advancing glaciers in the Brooks Range and aridity in the Yukon, suggesting a shift to cooler temperatures and drier conditions (0.3°C above the last millennium average, LMA = 4.2°C). Cooling culminated in an extreme-cold event between AD 980 and 1030 when estimated JJA temperatures averaged 0.7°C below the LMA. From AD 1030-1620, JJA temperatures varied around the LMA. One exception is a 90-year cold event (~AD 1260-1350) when JJA temperatures fell to 0.2°C below the LMA. There is no clear evidence for a warm event at Blue Lake coincident with the European MWP (AD 1000-1300). Two warm periods, however, occurred from AD 1350-1450 and AD 1500-1620 (0.4 and 0.3°C above the LMA, respectively).

Summer temperatures at Blue Lake during the LIA (AD 1620-1880) averaged 0.2°C below the LMA (1.0°C below the AD 1950-2005 average). This estimate agrees with independent regional temperature estimates that suggest the LIA was most likely between 0.6 and 2.0°C cooler. Other published evidence, but not all, suggests the LIA was arid in northern Alaska and the Yukon. After AD 1880, JJA temperatures increased to 0.8°C above the LMA by AD 2005, and glaciers retreated in the Brooks Range. Relative aridity, however, has persisted. Notably, post-LIA varve thicknesses do not achieve pre- AD 730 levels. We suggest that this reflects the relatively recent glacier retreat that is still occurring, and not yet as extensive as the prolonged first millennium retreat. Large amounts of unconsolidated sub-glacial sediment, therefore, remain protected by the glacier and are not available for transport to the lake. In subsequent decades as the glacier retreats further, we project that sediment influx to the lake will increase.

Climate trends inferred from Blue Lake varve thicknesses, in comparison with records from the eastern Canadian Arctic, suggest differences in the existence, timing and magnitude of events such as the MWP and LIA onset between the eastern and western North American Arctic. However, the Blue Lake varve thickness record compares well with some varve records from the eastern Canadian Arctic (i.e. Lake C2, Upper Soper Lake, and Tuborg Lake) with respect to the timing and magnitude of LIA cooling and post-LIA warming.

3.0 SOUTH AMERICAN SUMMER MONSOON VARIABILITY DURING THE LITTLE ICE AGE AND MEDIEVAL CLIMATE ANOMALY

3.1 ABSTRACT

We present a 2300-year-long reconstruction of the South American summer monsoon (SASM) based on $\delta^{18}O$ measurements of authigenic calcite ($\delta^{18}O_{cal}$) preserved in varved sediments from Laguna Pumacocha in the central Peruvian Andes. Average lake water oxygen isotopic composition ($\delta^{18}O_{lw}$) since AD 2006 is identical with the isotopic composition of mean annual precipitation ($\delta^{18}O_{precip}$) predicted from IAEA-GNIP data, indicating that $\delta^{18}O_{lw}$ reflects $\delta^{18}O_{precip}$. Modern $\delta^{18}O_{cal}$, in turn, tracks $\delta^{18}O_{lw}$, and provides the physical basis for using down core measurements of $\delta^{18}O_{cal}$ to infer changes in $\delta^{18}O_{precip}$ associated with changes in the strength of the SASM. A period of high $\delta^{18}O_{cal}$ values with reduced variability occurs between AD 920-1050, which is contemporaneous with the Medieval Climate Anomaly (MCA) and suggests that the SASM was weakened and less variable during this time. An abrupt transition to low $\delta^{18}O_{cal}$ and enhanced variability begins at AD 1265 and culminates from AD 1415-1820 with the greatest degree of variance from AD 1500-1770. These trends mark the Little Ice Age at Pumacocha and suggest that the SASM was greatly enhanced and highly variable during this interval. We attribute the inferred SASM dynamics during the MCA to weakened easterly tropospheric flow and reduced ENSO frequency and amplitude, and, during the LIA, to greatly

enhanced easterly tropospheric flow and increased ENSO frequency and amplitude. These changes in tropical atmospheric circulation may be the expression of the tropical Pacific's response to enhanced radiative forcing during the MCA, and reduced radiative forcing during the LIA as described by the ocean dynamical thermostat model (Clement et al., 1996). Recent studies have suggested that the dynamical response of the tropical Pacific may influence Northern Hemisphere climate via teleconnections with the North Atlantic. Such a connection may explain, in part, the striking similarities between the Pumacocha SASM reconstruction and Northern Hemisphere temperature reconstructions.

3.2 INTRODUCTION

Our understanding of modern interannual and decadal South American summer monsoon (SASM) variability has improved dramatically as a result of long-term instrumental data collection and satellite monitoring that now spans decades. From these data, it is apparent that meridional and zonal sea surface temperature (SST) dynamics in the tropical Pacific and tropical Atlantic largely control high frequency SASM variability (Villar et al., 2008; Vuille et al., 2003a; Zhou and Lau, 1998). However, high-frequency SASM dynamics are poorly understood beyond the instrumental period because paleoclimate records capable of capturing this level of detail are exceedingly rare. Indeed, the 1500-year-long ice core from the Quelccaya Ice Cap is the longest annually resolved climate archive from tropical South America currently available (Thompson et al., 1985).

Here, we present a 2300-year-long oxygen isotope record from Laguna Pumacocha, a varved alkaline lake in the central Peruvian Andes. This record captures changes in the strength

of the SASM during the late Holocene at interannual- to centennial-scales and provides new insight into how this system responded to changes in the global mean climate state. The last two millennia are an excellent backdrop against which to assess SASM variability because the mean global climate varied between generally warm conditions during the Medieval Climate Anomaly (MCA; 900-1300) and cool conditions during the Little Ice Age (LIA; 1300-1900; Crowley, 2000; Mann and Jones, 2003; Moberg et al., 2005). By constraining SASM dynamics during these climatic intervals, we may better understand how changes in the mean state of the global climate affect SASM variability.

3.3 STUDY AREA

Laguna Pumacocha is a small cirque lake in the eastern Peruvian Andes at 4300 meters above sea level (asl; -10.69882, -76.06110; Fig. 10, 11a). The basin has an area of 1.7 km^2 and a headwall elevation of 4600 m asl. The catchment is unglaciated and there is no evidence of glaciation during the Holocene. However, there are several lateral and recessional moraines in the valley that may date to the last local glacial maximum (Fig. 11a). Today, the watershed is free of trees and dominated by tussock grasses. The lake is deep (23.5 m deep) with a unique morphology that is characterized by very steep sides and a flat bottom (Fig. 11b). This allows the lake to maintain a permanently stratified water column with anoxic conditions below 8 m depth and a large volume (1.37×10^6 m^3) despite a small surface area (0.09 km^2; Fig. 11b). Deepwater anoxia precludes benthic organisms from colonizing the lake floor, which allows sediment to accumulate undisturbed. The lake is surrounded on all sides by a broad marshy area

that varies between 10 and 50 m in width. This fringing wetland limits allochthonous material from being washed into the lake during the wet season and thereby restricts sediment supply to autochthonous and/or eolian materials. Bedrock within the watershed is comprised largely of Jurassic marine limestone (Quispensivana, 1996), which supplies dissolved HCO_3^- and Ca^{2+} ions to the lake via two springs that are located to the north and south of the basin margin (Fig. 11a).

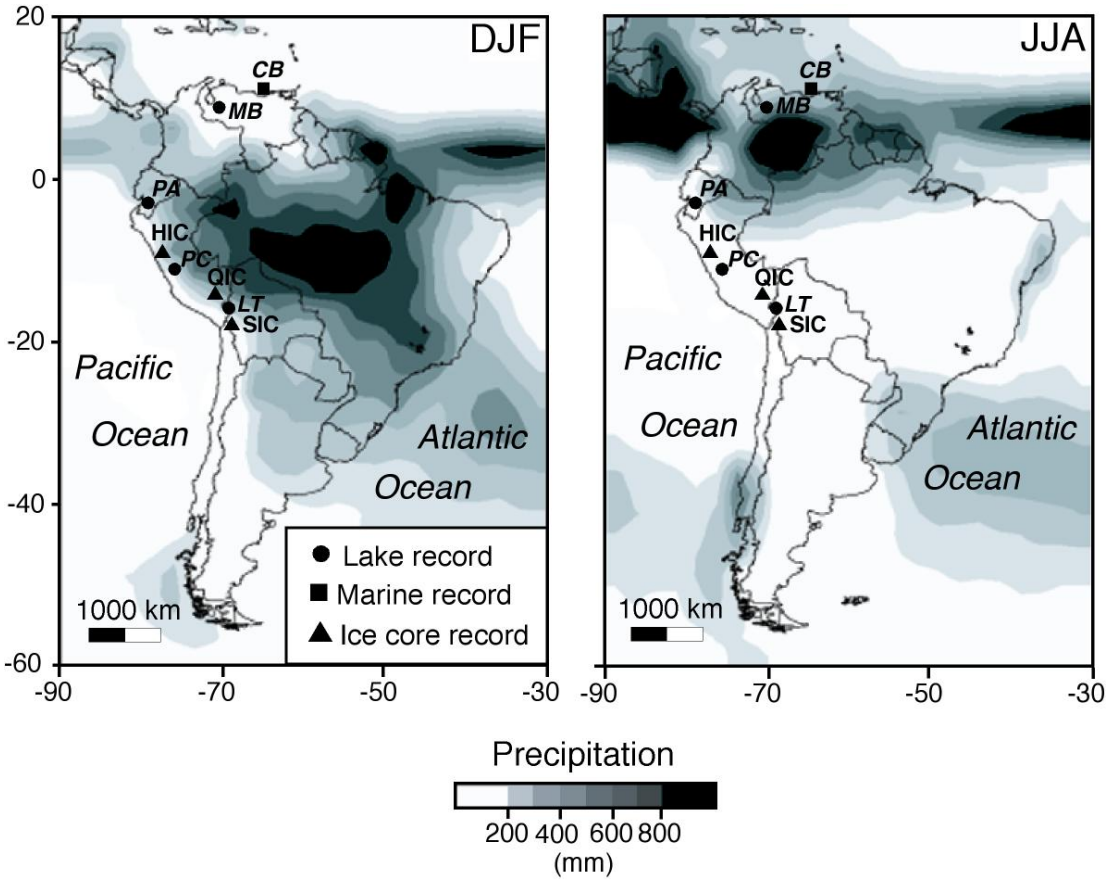

Figure 10 Map of South America showing the location of records discussed in the text (CB= Cariaco Basin, MB = L. Mucubaji, PA = L. Pallcacocha, HIC = Huascaran Ice Core, PC = Pumacocha, QIC = Quelccaya Ice Cap, LT = L. Titicaca). The shaded regions denote the location of precipitation maxima during the austral summer (December, January, February; on the left) and winter (June, July, August; on the right). Maxima over the oceans are related to low-level convergence of the trade winds and subsequent rising motion associated with the Intertropical Convergence Zone (ITCZ). Maxima over South America are associated with the SASM.

As a result, Laguna Pumacocha maintains a high alkalinity (140-220 ppm HCO_3^-) and saturation with respect to calcite throughout the year. The inflow from these springs is small relative to the amount of precipitation received during the summer monsoon (~1,100 to 1,500 mm at Cerro de Pasco, 22 km west of the Pumacocha basin) (Peterson et al., 1998). The volume of monsoonal precipitation that falls over the watershed is nearly double that of the lake's volume, indicating the residence time of water in the lake is extremely short, perhaps one year or less. Laguna Pumacocha drains year round to the east via a small outlet stream that flows ~100 m before entering nearby Laguna Pucpush (Fig 11b). Laguna Pumacocha's limnological characteristics of and geologic setting allow it to precipitate authigenic calcite that is preserved in finely laminated varves and uncontaminated by detrital carbonate from the watershed. Together, the above characteristics make Laguna Pumacocha an ideal setting for preserving high-fidelity archives of hydrologic variability on long time-scales.

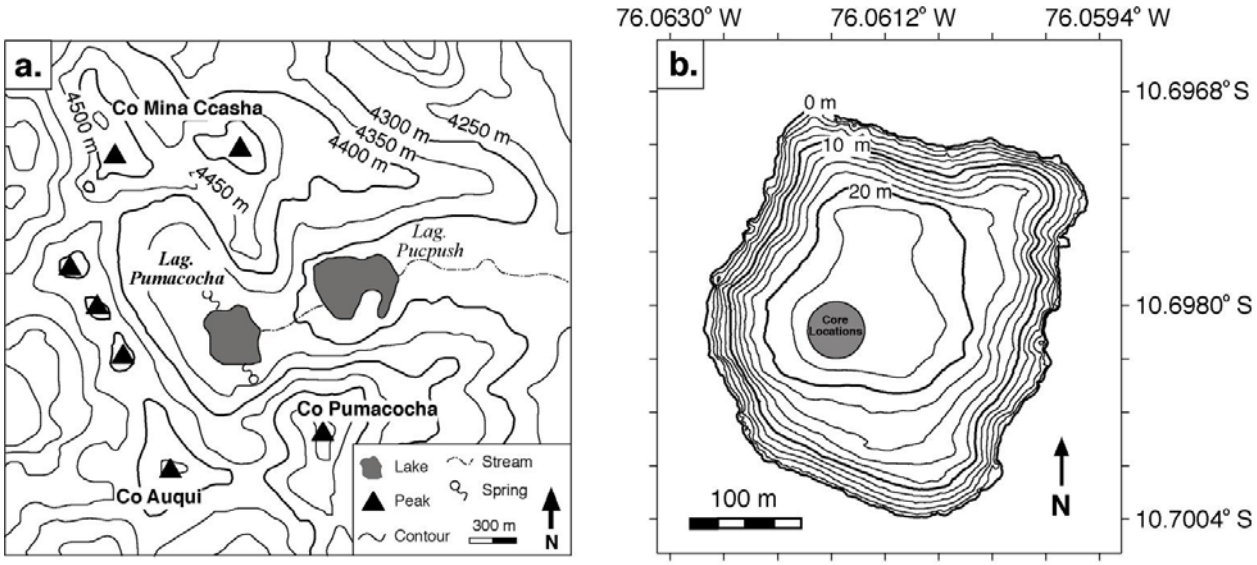

Figure 11(a) Topographic map of the Pumacocha watershed and surrounding area. (b) Bathymetric map of Pumacocha showing the location were cores collected.

3.4 METHODS

3.4.1 Sediment core recovery

Sediment cores were retrieved from Laguna Pumacocha in a water depth of 23.5 m in June 2005 and August 2006 using a modified Livingstone square-rod corer (Fig. 11b; Wright et al., 1984). Successive 1-meter-long drives were overlapped by 20 cm to ensure continuous sediment recovery. A network of freeze cores, which captured the undisturbed sediment-water interface, was collected from the deepest part of the lake in August 2006 and May of 2007 and 2008 (Table 6). In total, 579.0 cm of sediment were recovered from the lake. Indurated glacial deposits below 579.0 cm prevented additional sediment recovery. A single composite record of the upper 176.2 cm, the interval with which this work is concerned, was made by correlating the physical and geochemical characteristics of freeze cores B-08, B-07, D-07 and Livingstone cores A-05 and C-06.

Table 6 Name, type, and length of cores collected from Pumacocha. The (*) denotes which cores were used in the final composite record

Core	Type	Length (cm)	Sediment interface
A-05*	Livingstone	535	No
B-05	Surface	70	Yes
C-06*	Livingstone	579	No
D-06	Surface	145	Yes
E-06	Freeze core	55	Yes
A-07	Freeze core	62	Yes
B-07*	Freeze core	58	Yes
C-07	Freeze core	60	Yes
D-07*	Freeze core	65	Yes
A-08	Freeze core	69	Yes
B-08	Freeze core	72	Yes
C-08	Freeze core	72	Yes
D-08*	Freeze core	69	Yes
E-08	Freeze core	70	Yes
F-08	Freeze core	74	Yes

3.4.2 Sediment imaging and mineralogy

High-resolution digital images of the Livingstone cores were acquired at the University of Minnesota Limnological Research Center using a fixed position line-scanning digital camera with polarized full-spectrum lighting. Freeze core images were acquired at the University of Pittsburgh with a fixed position digital camera housed in a light box with full spectrum fluorescent lights. Sediment textures were imaged using a Philips XL-30 field emission scanning electron microscope (SEM). Sediment mineralogy was identified by X-ray diffraction (XRD) using a Philips X'pert diffractometer. SEM and XRD analyses were performed at the Materials Micro-Characterization Laboratory of the Department of Mechanical Engineering and Materials Science, Swanson School of Engineering, University of Pittsburgh.

3.4.3 Modern sedimentation and Limnology

Modern carbonate was collected in sediment traps that were deployed in the deepest part of the Pumacocha basin from August 2006 to May 2007 and from littoral vegetation in August 2006 and May 2008. The lake's characteristics and local climatic conditions were measured at 4-hour intervals between May 29, 2007 and May 11, 2008. Lake-level and lake-surface temperature was measured with a Solinst® Levellogger® data logger deployed in a fixed position 125 cm below the lake surface. Air temperature and barometric pressure at the lake were measured with a land-based Solinst® Barologger® device. A LogTag® data recorder placed ~500 m down valley at 4200 m asl recorded percent relative humidity and air temperature. Depth profiles of lake water temperature, pH, dissolved oxygen, and specific conductivity were measured with a Hydrolab® MiniSond® 4a at ~1 m intervals in June 2005, August 2006, and May 2007.

Samples for alkalinity measurments and lake water isotopic composition ($\delta^{18}O_{lw}$, δD_{lw}) were collected from the coring site during field seasons between June 2005 and May 2008. Additional samples for $\delta^{18}O_{lw}$ and δD_{lw} were collected monthly between August 15, 2006 and May 25, 2008. Water samples for oxygen and hydrogen isotopic analysis and alkalinity determinations were also collected from the springs feeding the lake in May 2007 and 2008.

Alkalinity was measured in the field with a Hach® alkalinity kit by titrating water samples to an end point pH of 4.0 with 1.6 N H_2SO_4. The volume of acid consumed was used to calculate moles of HCO_3^-. Oxygen and hydrogen isotopic ratios of lake water were measured at the University of Arizona Environmental Isotope Laboratory. The reported precision is 0.08‰ for $\delta^{18}O$ and 0.11‰ for δD. All values are reported as the per mil (‰) deviation from Vienna standard mean ocean water (VSMOW).

3.4.4 Radiometric age control

Samples for ^{210}Pb, ^{226}Ra, and ^{137}Cs were collected at ~1 cm intervals between 0.0 and 30.0 cm from freeze core D-08 and measured by direct gamma counting using an EG & G Ortec GWL high purity germanium well detector (Appleby et al., 1986; Schelske et al., 1994) at the University of Florida's Land Use and Environmental Change Institute (Table 7). Radium-226 activity was measured at each depth to estimate supported 210Pb activity. Unsupported ^{210}Pb activity was estimated by subtraction of supported activity from the total activity measured at each level. Sediment ages were determined using the constant rate of supply model and linear accumulation (Appleby & Oldfield, 1978). Eighteen radiocarbon (^{14}C) ages were determined by accelerator mass spectrometry (AMS) on selected charcoal fragments at the University of California, Irvine, W. M. Keck Carbon Cycle Accelerator Mass Spectrometry Laboratory (Table

8). All samples were cleaned and pretreated according to standard protocols at the University of Pittsburgh's Radiocarbon Laboratory (Abbott and Stafford, 1996). All AMS ^{14}C ages were calibrated to years before present (cal yr B.P.; present = AD 1950) with the online program CALIB 5.0 (Stuiver and Reimer, 1993). The reported ages are the 2σ median probability age with errors that are one-half of the 2σ age range.

Table 7 Pumacocha ^{210}Pb, ^{226}Ra and ^{137}Cs results from freeze core D-08

Top depth (cm)	Bottom depth (cm)	Dry BD g/cc	Pb-210 activity (dpm/g)	Pb-210 1σ error	Ra-226 activity (dpm/g)	Ra-226 1σ error	Excess Pb-210 activity (dpm/g)	Excess Pb-210 activity 1σ error	Cs-137 activity (dpm/g)	Cs-137 1σ error
0	0.85	0.0364	18.328	0.623	1.989	0.672	16.521	0.926	0.000	0.010
0.85	1.75	0.0454	29.019	0.871	1.895	0.816	27.434	1.207	0.000	0.007
1.75	3.1	0.0536	23.525	0.958	1.219	0.988	22.565	1.392	0.000	0.005
3.1	4.2	0.0521	16.231	0.855	0.507	0.660	15.907	1.093	0.000	0.007
4.2	5.3	0.0645	32.196	0.775	1.024	1.306	31.539	1.537	0.139	0.037
5.3	6.25	0.0965	28.543	1.014	1.084	0.339	27.789	1.082	0.000	0.017
6.25	7.45	0.0719	22.291	0.986	0.698	0.930	21.854	1.372	0.244	0.066
7.45	8.7	0.0568	26.211	1.269	0.684	0.990	25.838	1.629	0.000	0.008
8.7	10.5	0.0808	30.815	1.087	1.486	1.379	29.689	1.777	0.790	0.103
10.5	11.05	0.1139	29.697	0.473	2.348	0.135	27.688	0.499	0.005	0.011
11.05	12.1	0.1252	22.434	0.719	2.429	0.151	20.258	0.743	0.000	0.003
12.1	13.1	0.1063	25.177	0.726	2.583	0.909	22.881	1.178	0.000	0.014
13.1	14.45	0.1042	19.369	0.756	0.597	0.179	19.012	0.787	0.082	0.035
14.45	15.45	0.1119	17.914	0.655	0.747	0.723	17.388	0.988	0.080	0.030
15.45	16.5	0.0861	18.642	0.764	1.060	0.760	17.810	1.091	0.161	0.046
16.5	17.5	0.1324	11.980	0.282	1.208	0.418	10.912	0.511	0.000	0.007
17.5	18.5	0.1096	10.103	0.464	1.087	0.392	9.136	0.615	0.000	0.003
18.5	19.7	0.1529	6.955	0.344	1.144	0.573	5.890	0.677	0.013	0.016
19.7	20.5	0.1244	6.560	0.273	1.037	0.203	5.583	0.344	0.017	0.014
20.85	21.7	0.1762	4.442	0.156	0.879	0.562	3.611	0.591	0.018	0.009
21.7	22.9	0.1934	4.178	0.144	0.831	0.072	3.394	0.164	0.011	0.008
22.9	24.3	0.1881	3.699	0.190	1.502	0.139	2.228	0.239	0.043	0.014
24.3	25.35	0.1756	2.072	0.157	0.997	0.130	1.091	0.207	0.000	0.003
25.35	26.4	0.1735	2.619	0.137	1.079	0.312	1.564	0.346	0.000	0.003
26.4	27.5	0.1771	1.419	0.156	0.590	0.329	0.840	0.369	0.026	0.015
27.5	28.75	0.1799	1.845	0.147	1.046	0.171	0.811	0.229	0.000	0.003
28.75	29.75	0.1366	2.368	0.217	1.460	0.124	0.922	0.254	0.000	0.004
29.75	30.7	0.1521	1.128	0.142	0.789	0.365	0.344	0.398	0.000	0.003

Table 8 Radiocarbon ages from Laguna Pumacocha

UCI #	Core	Core depth (cm)	Material	Fraction modern	^{14}C yr BP	Error (+/-)	2σ calibrated age (AD/BC)	2σ median calibrated age (AD/BC)	Median error (+/-)
7556	B-06	23.9	Charcoal	0.9634	300	25	1510-1600 AD	1560 AD	45
7557	B-06	209.2	Charcoal	0.6948	2925	20	1210-1050 BC	1130 BC	85
37635	C-06	95.3	Charcoal	0.8478	1325	30	650-720 AD	680 AD	35
37636	C-06	283.5	Charcoal	0.6172	3875	45	2470-2270 BC	2360 BC	100
37558	I-06	273.6	Charcoal	0.6242	3785	25	2290-2140 BC	2220 BC	75

3.4.5 Couplet-based age control

Couplets comprised of organic and carbonate rich sediments (see sedimentology discussion below) were counted from high-resolution digital images of freeze core cores B-08 and Livingstone core C-06 to a depth of 104.5 cm following the methods outlined by Francus et al. (2002). At least four counts were performed on each core to ensure the data's quality and to derive an estimate of cumulative age error (1%). Ages based on couplet counts are referred to as varve years AD/BC.

3.4.6 Carbonate sampling and stable isotope measurements

The uppermost 210 carbonate laminations (1 year per lamina) were individually sampled from freeze cores B-08, B-07, and D-07 for carbonate isotope ($\delta^{18}O_{cal}$, $\delta^{13}C_{cal}$) analysis. Livingstone cores C-06 and A-05 were also sampled for carbonate isotopes at 1 mm intervals (averaging 1.25 years per sample). All samples were soaked in 7% H_2O_2 for at least 24 hours and sieved at 63 μm. The < 63 μm fraction was then soaked in a 50% commercial bleach solution for 6 to 8 hours, rinsed three times with deionized water, vacuum freeze dried, and homogenized. Carbonate isotope samples were measured at the University of Pittsburgh using a GV

Instruments, Ltd. (now Isoprime, Ltd., a subsidiary of Elementar Analysensysteme) Isoprime™ stable isotope ratio mass spectrometer and Multi-Prep™ inlet module and Gilson autosampler. Stable isotope measurements were also completed at the University of Arizona using an automated carbonate preparation device (Thermo Finnigan KIEL-III) coupled to a gas-ratio mass spectrometer (Finnigan MAT 252). Powdered samples were reacted with dehydrated phosphoric acid under vacuum at 70°C (Arizona) and 90°C (Pittsburgh). Results are reported in conventional delta notation as the per mil (‰) deviation from Vienna Pee Dee Belemnite (VPDB). Results were calibrated with repeated measurements of the standards NBS-19 and NBS-18. Precision for $\delta^{18}O_{cal}$ is ± 0.1 and 0.13‰ and ± 0.06‰ and 0.09‰ for $\delta^{13}C$ (1σ), at the University of Arizona and the University of Pittsburgh, respectively. Replicate sample measurements yielded an internal sample reproducibility of ± 0.02‰ for $\delta^{18}O_{cal}$ and ± 0.03‰ for $\delta^{13}C_{cal}$.

3.4.7 Data filtering and wavelet analysis

The Pumacocha $\delta^{18}O_{cal}$ data were interpolated by linear regression at one-year increments and subsequently filtered with a 20-year high-pass Butterworth filter (n = 3). Wavelet power spectra were calculated using the interpolated and filtered zero padded data using an online Interactive Wavelet program (Torrence and Compo, 1998). Significance was calculated at the 90% confidence interval relative to red noise variability.

3.5 RESULTS

3.5.1 Sedimentology

This paper focuses on the upper 176.2 cm of the 579.0-cm-long Pumacocha record. See Chapter 4 for a complete core description. With the exception of four discrete 'massive' intervals of alternating light to dark green centimeter-scale bands that occur between 176.2 and 104.5 cm, the couplets are continuous and well preserved from 0 to 176.2 cm (Fig. 12a, b; Table 9). The couplets between 0.0 and 176.2 cm consist of discrete dark green lamina overlain by tan to white calcite crystals (Fig. 12c, d). The euhedral shape of the calcite crystals indicates that that they were precipitated directly from the water column, most likely during the austral winter when lake water alkalinity and pH are elevated. The dark colored sediments are organic-rich and most likely formed during the austral summer, possibly from algal blooms resulting from enhanced nutrient flux caused by increased runoff and surface wind mixing during the SASM (Fig. 12d). Couplet structure and compositional regularity as indicated by SEM and XRD analysis of down-core smear slides suggests that these structures represent continuous rhythmic deposition seasonal, climatically-driven limnological variability. Distinct couplets are easily recognizable and can be traced throughout the network of cores, and demonstrates that sedimentation is spatially coherent throughout the lake.

Table 9 Depths and ages of stratigraphic units in the Pumacocha core

Depth (cm)	Age AD/BC	Time unit	Sediment type
0 to 104.5	2007 to 840	varve yr B.P.	Laminated couplets
104.5 to 123.5	840 to 460	cal yr B.P.	Massive & banded
123.5 to 158.5	460 to -54	cal yr B.P.	Laminated couplets
158.5 to 162.5	-54 to -106	cal yr B.P.	Massive & banded
162.5 to 166.5	-106 to -160	cal yr B.P.	Laminated couplets
166.5 to 171.0	-160 to -216	cal yr B.P.	Massive & banded
171.0 to 176.2	-216 to -277	cal yr B.P.	Laminated couplets

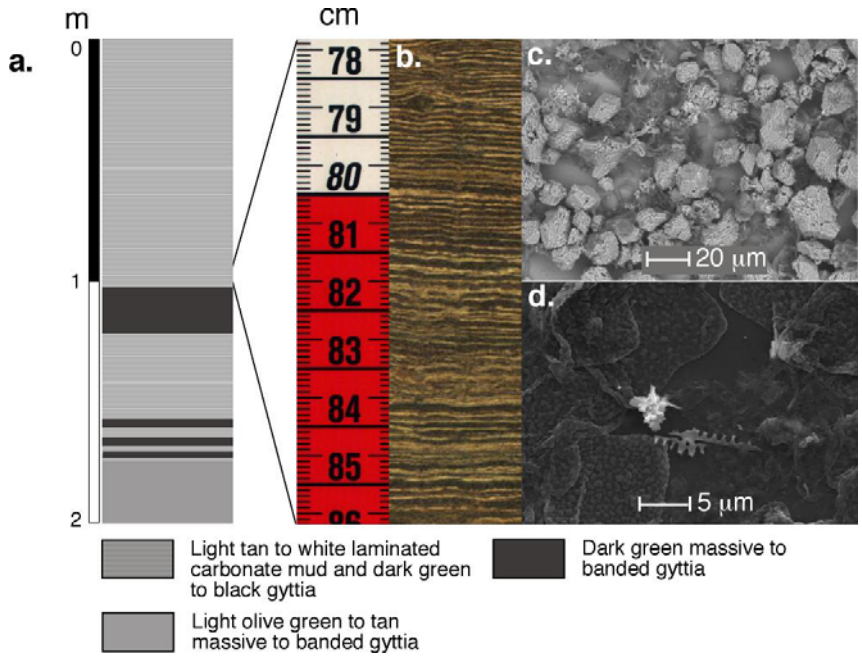

Figure 12 (a) Generalized stratigraphy of the upper 2 meters of the Laguna Pumacocha sediment record, (b) high-resolution digital image characteristic of the well-preserved couplets present in the upper 176.2 cm of the sediment column, and representative SEM images of light (c) and dark(d) colored laminations.

3.5.2 Age Control

Cesium-137 activity peaks between 8.7 and 10.5 cm, which indicates that sediment within this depth interval was deposited at, or just prior to, AD 1963 (Fig. 13). Using the mean depth of this sample, we estimated an average sedimentation rate of 0.21 cm yr^{-1} (Fig. 13; Table 7). The 8.7 to 10.5 cm depth interval also contains the AD 1963 couplet (Fig. 13). Sedimentation rates calculated using the depth of the AD 1963 couplet yields an average sedimentation rate of 0.20 cm yr^{-1}, which agrees well with the ^{137}Cs-based sedimentation rate. These results indicate that the couplets are varves and, therefore, we rely on linear interpolation between varve ages for age control between 0.0 and 104.5 cm. Varve-based ages have an estimated 1% cumulative error, which is represented by the increasing width of the black cone (Fig. 13).

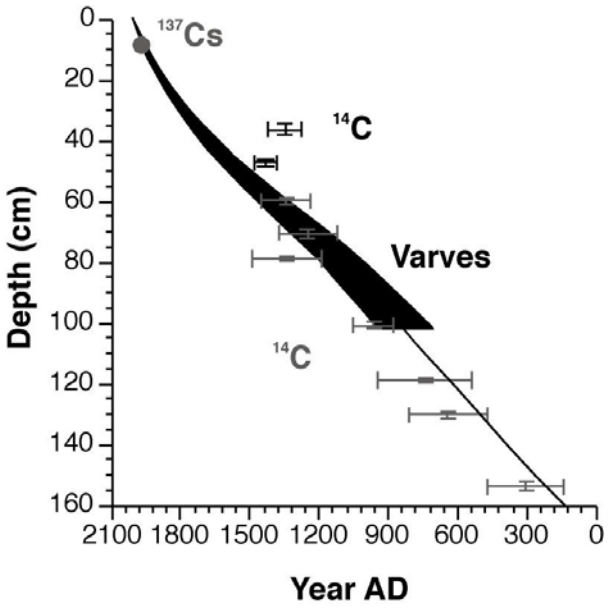

Figure 13 Results of radiometric age control and couplet-based ages from the upper portion of the Laguna Pumacocha record.

Three of the six AMS ^{14}C ages from the upper 105 cm of the Pumacocha record are in good agreement with the ^{137}Cs and couplet-based ages, while three show age reversals (Table 8). These anomalous ages may represent old carbon being washed into the system, contamination of the sample with aquatic matter, or emergent littoral vegetation, which partially received its carbon from the lake water, that was burned and introduced to the sediments. The good agreement between the unreversed AMS ^{14}C ages and the couplet-based ages supports the idea that the couplets are deposited annually (Fig. 13).

Unsupported ^{210}Pb is constant in the uppermost sediments between 0.0 and 8.7 cm. Below 8.7 cm, unsupported ^{210}Pb decreases exponentially (Table 7). The unsupported ^{210}Pb sediment accumulation rate (0.35 cm $^{yr-1}$) was determined using a linear accumulation model. This rate is higher than that calculated from couplet counts and ^{137}Cs and underestimates the age of the ^{137}Cs peak and AD 1963 couplet. Uniform ^{210}Pb activities in surface sediments can result

from sediment mixing caused by bioturbation or the coring process (Appleby and Oldfield, 1983). However, these mechanisms are ruled out by the fact that the Pumacocha sediments preserve finely laminated couplets to the sediment-water interface. Instead, we suggest that there exists a mobile ^{210}Pb fraction at the colloid or dissolved level that is able to migrate through interstitial pore waters until sediment compaction precludes its movement (Abril, 2003). This phenomenon is capable of affecting the ^{210}Pb profile while not influencing ^{137}Cs (Abril, 2003).

Based on the strong agreement between ^{137}Cs, AMS ^{14}C, and couplet counts, we conclude that the Pumacocha couplets are varves, and rely solely on these ages in the upper 104.5 cm of the Pumacocha record. Below 104.5 cm we use the remaining 12 AMS ^{14}C ages (Table 8). The final composite age/depth model is based on linear interpolation between varve-based ages and a 6th order polynomial fit to the AMS ^{14}C age/depth data (Fig. 13).

3.5.3 Modern $\delta^{18}O_{lw}$

Between August 2006 and May 2008, $\delta^{18}O_{lw}$ varied by a maximum of 1.7‰ with the highest values occurring during October 2006 (-12.1‰) and the lowest values occurring during April 2007 (-13.8‰; Fig. 14). Over the same time period, monthly $\delta^{18}O_{lw}$ was inversely correlated with lake-level and percent relative humidity (%RH). No clear relationship was observed between $\delta^{18}O_{lw}$ and air temperature or lake-surface temperature. Mean annual $\delta^{18}O_{lw}$ (-13.00 ‰) is identical within error to mean annual $\delta^{18}O_{precip}$ (-13.10‰ ± 1.5‰) estimated from gridded IAEA-GNIP data for the exact location and elevation of the Pumacocha watershed (Bowen and Wilkinson, 2002; Bowen and Revenaugh, 2003; Bowen et al., 2005).

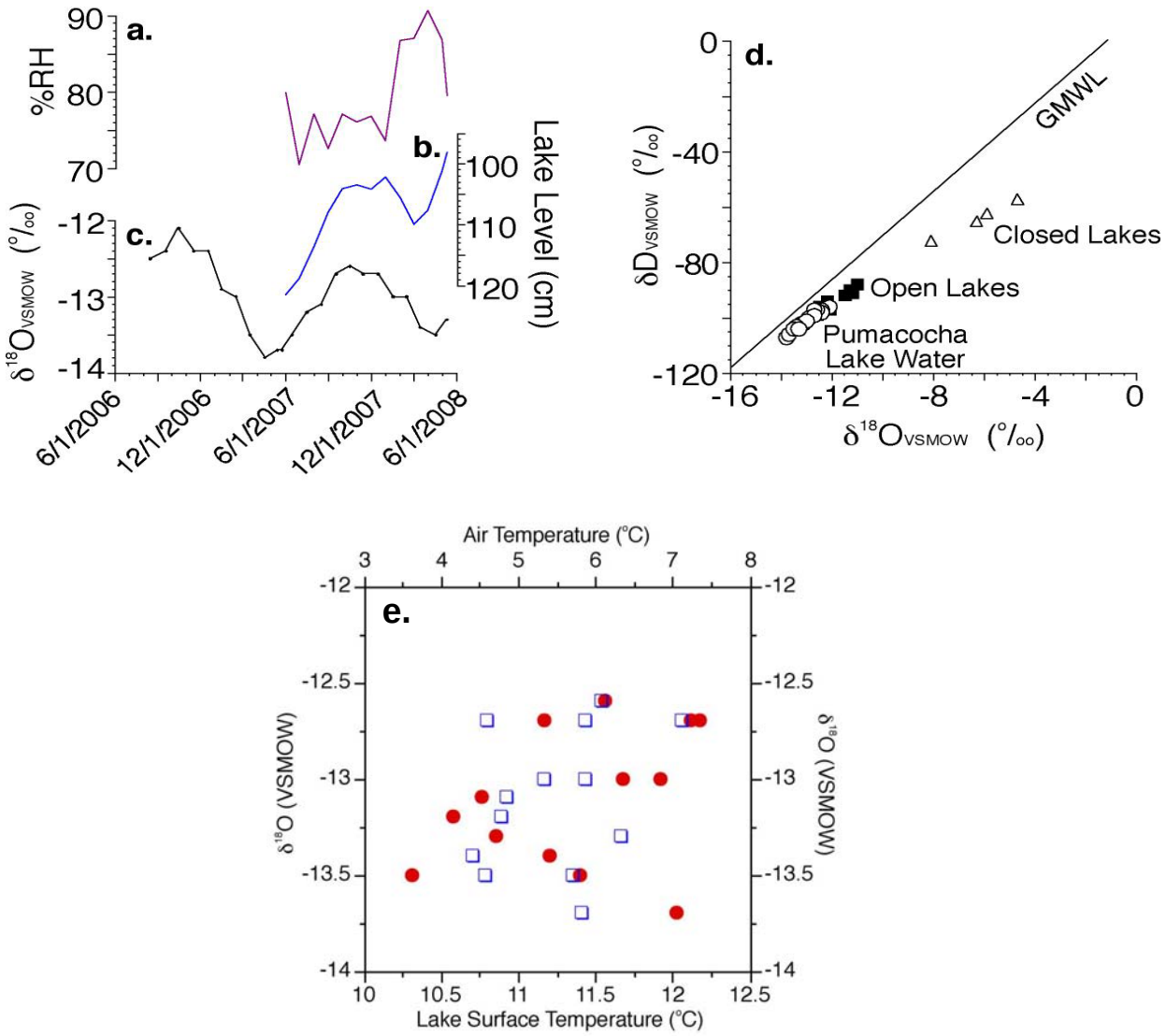

Figure 14 Modern (a) percent relative humidity (%RH), (b) lake level, and (c) monthly $\delta^{18}O_{lw}$ from Laguna Pumacocha. (d) Water isotope of samples collected from Pumacocha between June 2005 and May 2008 (open circles) are plotted with the so-called global meteoric water line (GMWL) and isotopic measurements from nearby lakes that exhibit open (black squares) and closed (open triangles) hydrologies. (e) Scatter plot of d18olw and surface air temperature (red circles) and lake surface temperature (open blue squares).

3.5.4 Modern $\delta^{18}O_{cal}$ and $\delta^{18}O_{lw}$

Authigenic carbonate collected within the littoral zone of the Pumacocha basin in August 2006 and May 2008 exhibited $\delta^{18}O_{cal}$ values averaging -12.2‰ and -12.4‰, respectively. Sediment trap $\delta^{18}O_{cal}$ averaged -12.8‰ with a maximum of -12.4‰ and a minimum of -13.2‰ between August 2006 and May 2007. Converted to VSMOW, sediment trap and littoral zone average $\delta^{18}O_{cal}$ values (-13.3‰) match average $\delta^{18}O_{lw}$ (-13.0‰). Individual annual $\delta^{18}O_{cal}$ measured on carbonate from littoral vegetation and sediments traps also matches $\delta^{18}O_{lw}$ during the corresponding time intervals. No relationship was observed between $\delta^{18}O_{cal}$ and air or lake surface temperature.

3.5.5 Annual $\delta^{18}O_{cal}$ (AD 1797 to 2007)

Oxygen isotopic variability in the uppermost 210 carbonate laminations is dominated by centennial-scale variability with decadal- and interannual-scale variability superimposed (Fig. 15a). From AD 1797-2007, $\delta^{18}O_{cal}$ averages -13.3‰ with a maximum of -11.7‰ and a minimum of -15.0‰. Oxygen isotopic values were relatively low from AD 1797-1825. Between AD 1825 and 1908, $\delta^{18}O_{cal}$ was high, but variable. Oxygen isotopic values decreased abruptly after AD 1908, but increased gradually to the present. Superimposed upon these long-term trends is decadal-scale variability, which is characterized by cycles that range in length from 11 to 27 years with an average of 20 years per cycle. During these cycles, $\delta^{18}O_{cal}$ values varied by as much as 2.6‰. Interannual variability from AD 1797-2007 is strongest at the 2.5 to 8 year period (Fig. 16).

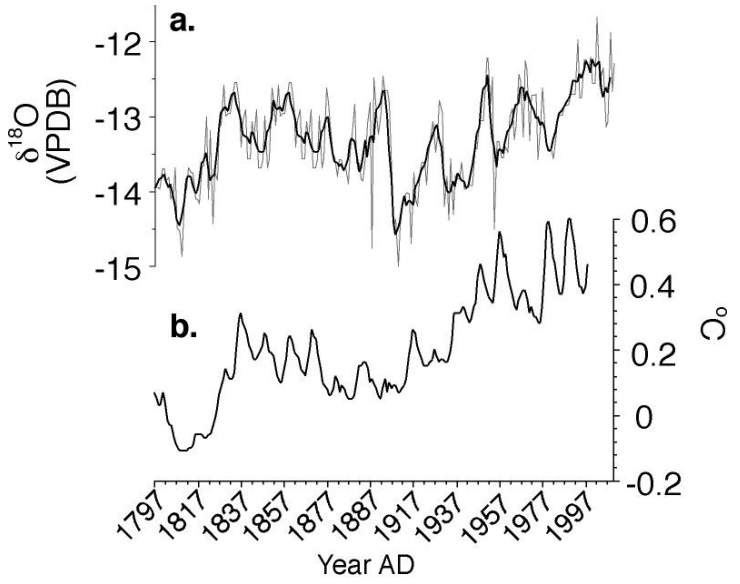

Figure 15(a) $\delta^{18}O_{cal}$ of individual carbonate lamina sampled from Pumacocha. The light gray line represents the raw data and the thick black line is a 5-point moving average. (b) Estimated net radiative forcing (Crowley et al. 2000) of solar variability, aerosol loading, greenhouse gasses, and volcanic activity from AD 1797 to the present.

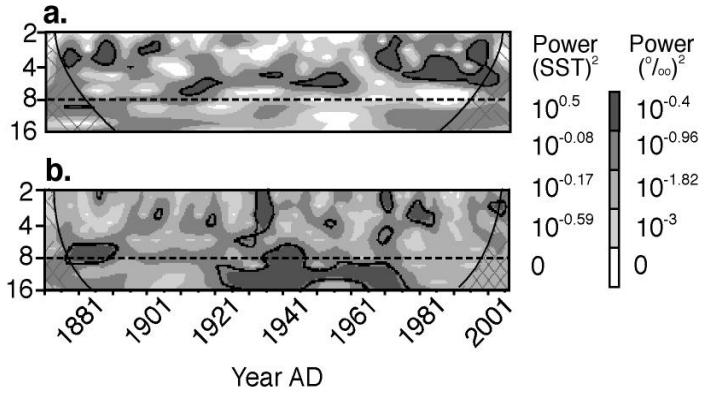

Figure 16 Wavelet power spectra of (a) average December, January, February sea surface temperatures in the NINO 3.4 region and (b) Pumacocha $\delta^{18}O_{cal}$ filtered with a 20 year high-pass Butterworth filter (N = 3) from AD 1871 to 2007. The NINO 3.4 and Pumacocha wavelet power spectra show significant variability between 2 and 8 years.

3.5.6 $\delta^{18}O_{cal}$ from 277 BC to AD 1797

Between 277 BC and AD 1797, $\delta^{18}O_{cal}$ values ranged between -10.7‰ and -15.8‰, with an average of -13.4‰ (Fig. 17b). From 277 BC to AD 920, $\delta^{18}O_{cal}$ was highly variable, ranging from -11.9 to -15.3‰ around a mean of -13.2‰. After AD 920, $\delta^{18}O_{cal}$ values increased sharply with two discrete peaks centered at AD 950 (-11.3‰) and AD 1010 (-10.7‰). Carbonate $\delta^{18}O$ values decreased after AD 1050 to an average of -13.4‰ with a minimum of -14.6‰ and a maximum of -12.2 ‰ until AD 1265. After AD 1265, $\delta^{18}O_{cal}$ dropped steeply, although with much variability, until reaching a sustained minimum between AD 1415-1700 where $\delta^{18}O_{cal}$ averages -14.3‰ with a maximum of -12.9‰ and a minimum of -15.8‰. After AD 1700 there was a series of abrupt stepwise increases in $\delta^{18}O_{cal}$. The first major shift occurred at AD 1700 with a second shift at AD 1780, and a third shift at AD 1825.

Interannual $\delta^{18}O_{cal}$ variability is present throughout the composite Pumacocha record at the 4-8 year period; however, it is strongest between ~AD 1430 and 1700 (Fig. 17a). After ~AD 1770, interannual variability is reduced with a shift to more annual scale variability. Other periods of enhanced interannual variability occurred between ~AD 800-1000, and ~AD 1250-1400 (Fig 17a).

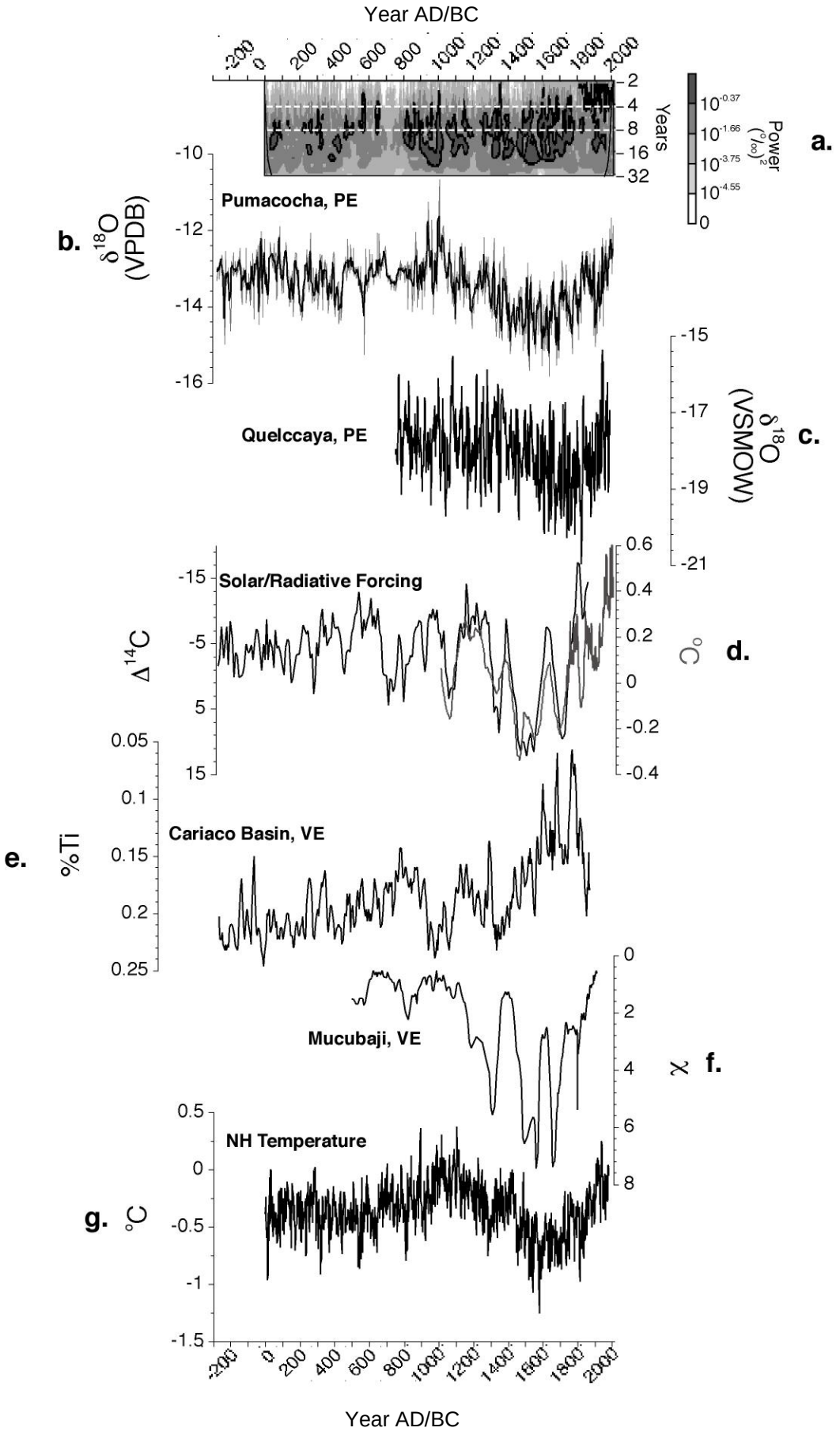
Year AD/BC
-200
0
200
400
600
800
1000
1200
1400
1600
1800
2000
2
4
8
16
32
Years
Power (‰)²
10^-0.37
10^-1.66
10^-3.75
10^-4.55
0
a.
b.
δ18O (VPDB)
Pumacocha, PE
Quelccaya, PE
c.
δ18O (VSMOW)
d.
Solar/Radiative Forcing
Δ14C
‰
e.
%Ti
Cariaco Basin, VE
Mucubaji, VE
χ
f.
NH Temperature
g.
°C
Year AD/BC

Figure 17(a) Wavelet power spectra of the Laguna Pumacocha δ18Ocal record for the last 2000 years. (b) Oxygen isotopic values from Laguna Pumacocha versus age data are shown in light gray with the thick black line denoting the 5-point moving average of the raw data. (c) 5-point moving average of δ18O from the Quelccaya Ice Cap, PE (Thompson et al. 1985). (d) Crowley et al. (2001) net radiative forcing (light gray line) and residual 14C (Δ14C) (black line). (e) Titanium concentration (%) in sediment cores from the Cariaco Basin (Haug et al. 2001). (f) Magnetic susceptibility (10-6) from Laguna Mucubaji, VE (Polissar et al., 2006). (g) Northern Hemisphere temperature reconstruction by Moberg et al. (2005).

3.6 DISCUSSION

3.6.1 Climatic significance of Pumacocha $\delta^{18}O_{cal}$

Variations in lake water and calcite $\delta^{18}O$ at Laguna Pumacocha may be caused by temperature variability at the time of precipitation and temperature effects at the time of calcite formation in the lake. Temperature is not considered a major contributing factor because modern isotopic shifts in $\delta^{18}O_{cal}$ from deepwater sediment traps (0.79‰) are 2.5 times larger than can be explained by observed surface water temperature variability alone (0.32‰). Oxygen isotopic variability may also be caused by the changes isotopic composition of precipitation, evaporative modification of surface water transported to the lake, the isotopic composition of groundwater feeding the lake, evaporation from the lake surface, surface outflow, and groundwater outflow. At Laguna Pumacocha, only $\delta^{18}O_{precip}$ changes significantly influence lake water oxygen isotopic composition. Surface runoff after rainfall events experiences minimal evaporative modification because the watershed has a very small area and runoff does not travel far before being

incorporated into the lake. The small watershed area also reduces groundwater storage capacity and residence time, and thereby minimizes the influence that extra-basin groundwater may have on the isotopic mass balance of the lake. Additionally, the watershed is elevated above, and topographically separated from, other nearby watersheds. This isolates the lake from regional overland and groundwater flow that may have been isotopically modified. Evaporative modification of lake water is limited by the fact that overflow occurs year round and has a residence time one year or less. Inferred minimal evaporative enrichment of lake water is supported by long-term average $\delta^{18}O$ measurements since June 2005 (-13.0‰) that closely match mean annual $\delta^{18}O_{precip}$ values (-13.1‰ ± 1.5‰) estimated from gridded IAEA-GNIP data (Bowen and Wilkinson, 2002; Bowen and Revenaugh, 2003; Bowen et al., 2005). The agreement between $\delta^{18}O_{precip}$ and $\delta^{18}O_{lw}$ also suggests that groundwater and surface outflow from the lake do not greatly influence lake water oxygen isotopic composition. Given the limited influence of other factors, we conclude that changes in $\delta^{18}O_{precip}$ are the dominant control on $\delta^{18}O_{lw}$ variability at Pumacocha. The weak relationship ($r^2 = 0.39$; $p < 0.001$) between $\delta^{18}O_{cal}$ and $\delta^{13}C_{cal}$ during the last 2300 years suggests that the Pumacocha basin has been hydrologically open during at least the late Holocene and that the relationship between $\delta^{18}O_{lw}$ and $\delta^{18}O_{precip}$ has been stable during this time (Li and Ku, 1997). It could be argued that evaporation may become important during periods of extreme aridity. However, $\delta^{13}C_{cal}$-$\delta^{18}O_{cal}$ covariance remains weak ($r^2 = 0.05$, $p < 0.001$) even during the early Holocene when aridity was at its greatest, suggesting that Pumacocha has been hydrologically open for the duration of the Holocene (see Chapter 4). Additional support for robustness of the Laguna Pumacocha $\delta^{18}O_{cal}$-$\delta^{18}O_{precip}$ relationship through time comes from the striking correlations between the sediment core $\delta^{18}O$ record and oxygen and hydrogen isotopic records from the Huascaran ($r^2 = 0.77$, $p < 0.001$) and Illimani (r^2

= 0.73, $p < 0.001$) ice cores during the Holocene, respectively (see Chapter 4). Although initially interpreted in terms of temperature (Thompson et al., 2000), multiple lines of evidence strongly suggest that $\delta^{18}O$ in Andean ice cores reflects precipitation variability (Hastenrath et al., 2004; Hoffmann et al., 2003; Vuille et al., 2003b). The strong correlations between Pumacocha and these records supports that $\delta^{18}O_{cal}$ in Pumacocha reflects precipitation variability driven by changes in the strength of the SASM and that evaporation has not influenced Pumacocha. With this reasoning, we utilize down-core measurements of $\delta^{18}O_{cal}$ as a proxy for $\delta^{18}O_{precip}$.

3.6.2 The SASM and $\delta^{18}O$

Precipitation in the tropical Andes is largely controlled by the prevailing direction of middle- and upper-level tropospheric winds during the core of the SASM season (December-January-February; DJF). Changes in these winds regulate moisture transport to the high Andes from the Amazon Basin, which affects the strength of the SASM and $\delta^{18}O_{precip}$ (Garreaud et al., 2003; Garreaud et al., In Press; Hastenrath et al., 2004; Villar et al., 2008; Vuille and Werner, 2005). Strengthened easterly flow enhances upslope moisture transport from the Amazon basin to the Andes, resulting in increased precipitation and lower $\delta^{18}O_{precip}$ (i.e., the amount effect). Conversely, westerly flow over the Andes advects dry air from the Pacific coast, inhibiting moist convection, weakening the Andean SASM and increasing $\delta^{18}O_{precip}$. Variations in the direction of middle- and upper-tropospheric flow and thereby $\delta^{18}O_{precip}$ are fundamentally linked to zonal and meridional sea surface temperature anomalies (SSTAs) in the eastern tropical Pacific (ETP) and western equatorial Atlantic (WEA) (Bradley et al., 2003; Garreaud et al., 2003; Vuille et al., 2003a). However, tropical SSTAs in the WEA lag those in the ETP by up to several months,

indicating that SSTAs in the ETP are important in establishing the overall state of the Pacific-Atlantic ocean-atmosphere system (Czaja et al., 2002). Warm SSTAs in the ETP and northern WEA characteristic of El Niño events and the positive phase of the Pacific Decadal Oscillation (+PDO) correspond to reductions in precipitation over the tropical Andes is due to enhanced advection of dry air caused by westerly flow in the middle and upper troposphere (Garreaud et al., 2003; Garreaud et al., In Press). The opposite response is true for cool SSTAs in the ETP that typify La Niña events and the negative phase of the PDO.

3.6.3 SASM precipitation during the MCA and LIA

The Laguna Pumacocha sediment core $\delta^{18}O$ record suggests that the SASM is a dynamic system that has experienced considerable variability over a range of time-scales during the last 2300 years. However, the MCA (AD 920-1050) and LIA (AD 1410-1820) are clearly the largest climate anomalies during the late Holocene and will therefore be the focus of this discussion.

The MCA is not widely recognized in tropical South America because, with the exception of the Quelccaya ice core, there are no high-resolution terrestrial climate records that span this interval. Despite this limitation, lower-resolution records appear to agree that an arid interval, which may correspond with the MCA, spans the transition from the first to second millennia. Closest to the Pumacocha watershed, the Huascaran ice core (100 yrs per sample) shows an increase in $\delta^{18}O$ from ~ AD 900-1400. Given the ongoing debate with regard to the interpretation of ice core oxygen and hydrogen isotopes, we limit our interpretation of ice core $\delta^{18}O$ to cool/wet (low $\delta^{18}O$) and warm/dry (high $\delta^{18}O$). Based on this interpretation, the Huascaran ice core record suggests that the MCA was an arid and/or warm period at this location (Thompson et al., 1995). To the south, Lake Titicaca lake-level reconstructions (Abbott et al.,

1997a) indicate that water levels dropped between AD 1050 and 1450, roughly contemporaneous with, although slightly later than, the MCA at Laguna Pumacocha and Huascaran. The MCA is less distinct in ice core oxygen isotopic records from Quelccaya, but two large increases in $\delta^{18}O$ centered on ~AD 1000 and ~1080 may correspond to the periods of MCA aridity noted in the Pumacocha record (Fig. 17c; Thompson et al., 1985). Accumulation rates at Quelccaya show a more distinct reduction in accumulation during the MCA, suggesting that aridity persisted on the Altiplano between AD 1030-1300 (Thompson et al., 1985). This agrees well with the timing of the MCA at Lake Titicaca, but, again, is later than the inferred onset of drying in the Pumacocha basin, suggesting that north-south differences in the timing of the MCA may exist, specifically manifest as a latter MCA occurrence in the south. Finally, no glacial moraines in the tropical Andes have been identified that date to the MCA. This may indicate persistent warm/dry conditions when glaciers did not advance or that LIA advances were greater. The above records suggest that the MCA was an arid interval in the tropical Andes, which may also have experienced enhanced warmth. Although differences in the timing of this event exist between the southern and northern portion of the tropical Andes, the expression of the MCA in these records agrees well with the MCA at Pumacocha, suggesting that this event was widespread, and relatively synchronous.

In contrast with the MCA, the LIA appears to have been wetter and cooler than the present. Decreasing $\delta^{18}O_{cal}$ in the Pumacocha record at AD 1265 marks an intensification of the SASM at the beginning of the LIA (Fig. 17b). Minimum $\delta^{18}O_{cal}$ at Laguna Pumacocha between AD 1415 and 1700 and inferred $\delta^{18}O_{precip}$ suggests that the SASM was stronger during this time than at any other point in the last 2300 years (Fig. 17b). After AD 1700, $\delta^{18}O_{cal}$ increased, but by less than 1‰ on average, suggesting that the SASM weakened slightly. At Huascaran,

oxygen isotopic values during the LIA show a similar decrease, suggesting that cool/wet conditions were synchronous with Pumacocha (Thompson et al., 1995). Pollen evidence from the Sajama Ice Cap to the south supports the Pumacocha and Huascaran records, indicating very wet conditions on the Altiplano between AD 1500-1700 and greater aridity after AD 1700 (Liu et al., 2005). These results contrast somewhat with the isotopic data from Sajama, which show a prolonged wet/cool phase from AD1400 to the present (Thompson et al., 1998). Like Huascaran, however, the Sajama ice core is limited to 100 year averages per sample, which precludes a more detailed view of late Holocene climate events. Wet conditions during the LIA are also indicated by rising water levels at Lake Titicaca after AD 1450 (Abbott et al., 1997a). However, there is no clear evidence for a decrease in lake levels during the latter half of the LIA as indicated by the Sajama pollen data and Pumacocha $\delta^{18}O_{cal}$ record. Consistent with the Sajama pollen record and Pumacocha $\delta^{18}O_{cal}$, accumulation rates from the Quelccaya Ice Cap show a two phased LIA with greater accumulation between AD 1490-1650 and reduced accumulation between AD 1650-1850 (Thompson et al., 1985). Oxygen isotope values at Quelccaya do not track accumulation. Instead, $\delta^{18}O$ begins to decrease at ~ AD 1500 and remains low during the latter half of the LIA, despite the reduction in accumulation (Fig. 17c; Thompson et al., 1985). This discrepancy has been suggested to indicate that temperature has a greater influence on $\delta^{18}O$ at Quelccaya and that the early part of the LIA was wet and cool, and the latter half of the LIA was dry and colder (Thompson et al., 1985). However, $\delta^{18}O$ values at Quelccaya since AD 1915 are significantly and inversely correlated with lake level changes at Lake Titicaca, suggesting that precipitation variability (i.e., the amount effect) is the primary signal captured by Quelccaya $\delta^{18}O$ (Hastenrath et al., 2004). This suggests that other factors, such as sublimation or wind scour, may have affected the Quelccaya accumulation record and obscured the $\delta^{18}O$-accumulation relationship;

this has been noted for other South American ice cores (Hastenrath et al., 2004). Regardless of the controversy surrounding the interpretation of water isotopes in tropical ice cores, the overall expression of the LIA in the tropical Andes is similar between independent records from different regions. This indicates that the LIA was spatially coherent and generally synchronous.

Similar to the southern tropical Andes, sites to the north show a distinct LIA interval. Magnetic susceptibility measured within sediment cores from Laguna Mucubaji in the Venezuelan Andes (3570 m asl; 8.7833° N, 70.8333° S) is interpreted to reflect variations in contribution of glacially eroded terrestrial material to the lake. Increases in magnetic susceptibility between ~ AD 1375-1800 suggests that glaciers advanced in the watershed during the LIA in response to cooler temperatures and increased precipitation (Fig. 17f; Polissar et al., 2006b). In contrast, decreasing %Ti in the Cariaco Basin during the LIA are interpreted to reflect dry conditions in the northern tropics during the LIA (Fig. 17e; Haug et al., 2001). The discrepancy between these records may indicate that the Venezuelan Andes are sensitive to Southern Hemisphere atmospheric forcing and that the Cariaco Basin is responding to precipitation variability in regions further to the north or restricted to the Venezuelan coast (see Chapter 4).

3.6.4 Mechanisms of late Holocene climate change in tropical South America

The MCA and LIA were major climate events in the tropical Andes that were largely synchronous, widespread, and interhemispheric. This requires a common forcing mechanism that is capable of affecting changes in large-scale tropical atmospheric circulation. Several studies exploring the underlying causes of climate change during the last millennia agree that radiative forcing (i.e. the net influence of solar variability, volcanism, aerosols, and greenhouse

gasses) was a primary driver of late Holocene climate (Crowley, 2000; Mann and Jones, 2003). Although these studies primarily focused on the Northern Hemisphere (NH), model simulations that incorporated tropical paleoclimate data suggest that variations in radiative forcing influenced tropical Pacific SSTs during at least the last 1000 years (Mann et al., 2005), which, given their documented influence on modern tropical and global climate, may have impacted global-scale climate change in the past.

We assess the existence of a link between radiative forcing and the SASM during the last two millennia by comparing the Laguna Pumacocha $\delta^{18}O_{cal}$ record with reconstructions of net radiative forcing and solar variability (Fig. 17d). The net radiative forcing reconstruction accounts for the various influences on the Earth's radiation budget, such as solar variability, volcanism, aerosol loading, and greenhouse gas concentrations (Crowley, 2000). Unfortunately, this reconstruction is only available for the past 1000 years. Therefore, we use $\Delta^{14}C$, a proxy record of solar variability, as a rough indicator of the solar component of radiative forcing prior to AD 1000 (Bard et al., 2000; Bard et al., 1997). Given the similarities between net radiative forcing and $\Delta^{14}C$, this seems a reasonable first order approximation (Fig. 17d). However, it must be acknowledged that solar variability is only one component of net radiative forcing and that aerosols, greenhouse gasses, and volcanic activity are important factors that are required for the most accurate representation of radiative variability (Bertrand et al., 2002).

Although $\Delta^{14}C$ is typically used as a proxy for solar activity (high $\Delta^{14}C$ = low solar activity = negative radiative forcing, and vice versa), high-frequency variations in geomagnetic intensity may play an important, but unconstrained, role in $\Delta^{14}C$ variability (Snowball and Muscheler, 2007). This suggests that factors other than solar radiation, such as cosmic rays, may exert an influence on multidecadal- to centennial-scale climate variability. However, whether

solar irradiance, cosmic ray flux, or some combination of these two, produces the radiative forcing signal captured by $\Delta^{14}C$, the sign of the forcing is the same. For example, enhanced cloud cover (negative radiative forcing) is proposed to occur during periods of enhanced cosmic ray flux to Earth's upper atmosphere (Courtillot et al., 2007; Marsh and Svensmark, 2000). This would appear as a positive excursion in $\Delta^{14}C$, which is in the same direction as if reduced solar irradiance alone (negative radiative forcing) were driving $\Delta^{14}C$ variability. However, there is still considerable debate regarding the link between cosmic ray flux and cloud cover (Bard and Delaygue, 2008). As our understanding of how geomagnetic variations influence $\Delta^{14}C$ and the relationship between cosmic rays and Earth's climate evolves, the mechanisms driving radiative variability may change, but the sign of the forcing will likely remain the same.

A link between radiative forcing and the SASM is evident when Pumacocha $\delta^{18}O_{cal}$ is compared with net radiative forcing and $\Delta^{14}C$ (Fig. 15b, 17b, d). The long-term and decadal $\delta^{18}O_{cal}$ trends track radiative forcing from ~AD 1797 to the present, where positive radiative anomalies generally correspond to high $\delta^{18}O_{cal}$ (i.e. a weakened SASM), and vice versa. Comparing the entire Pumacocha $\delta^{18}O_{cal}$ record with $\Delta^{14}C$ shows that this relationship is consistent through time (Fig. 17b and d). The radiative forcing-SASM relationship is particularly strong during the MCA and LIA, but is present throughout the last 2300 years. One apparent reversal in this relationship occurred between ~ AD 1175-1250, when $\Delta^{14}C$ was high, but $\delta^{18}O_{cal}$ trended toward low values (Fig. 17b). Notably, this period is characterized by elevated tropical volcanic activity (data not shown; Mann et al., 2005), which suggests the important modifying effects of other radiative components, and underscores that caution must be used when relying solely on $\Delta^{14}C$ as an indicator of net radiative forcing. Although the strong correspondence between Pumacocha $\delta^{18}O_{cal}$ and $\Delta^{14}C$ suggests that radiative forcing has been a

primary driver of SASM variability during the last 2300 years, $\delta^{18}O_{cal}$ and $\Delta^{14}C$ do not vary linearly (Fig. 15, 17b and d). This suggests that other factors, such as internal climate dynamics and feedbacks, nonlinear climate system responses to radiative variability, or other factors not yet identified, exert an important influence on the SASM.

The sun-climate link has long been debated, because it is not clear how small changes in solar irradiance (~0.1% change between solar cycles) affect global climate. Suggested feedback mechanisms include the influence of solar UV rays on stratospheric ozone production (Haigh, 1994; Haigh, 2003), solar modulation of cosmic rays, which, as previously mentioned, may affect cloud formation and distribution (Svensmark, 1998; Usoskin, 2004), and the influence of solar irradiance on tropical and subtropical SST (Shindell et al., 2001). More recently, it has been proposed that ENSO transmits subtle changes in solar irradiance throughout the climate system. Using a state-of-the-art climate model, Emile-Geay et al. (2007) demonstrated that reductions in solar irradiance during the LIA were sufficient to produce a warming in the ETP that resembled an El Niño state and thereby increase the frequency and amplitude of ENSO (El Niño and La Niña). This response is consistent with the ocean dynamical thermostat model (ODT) first described by Clement et al. (1996). The ODT states that the tropical Pacific responds in a zonally asymmetric fashion to an imposed radiative forcing (cool ETP = warm WTP and vice versa) and that interannual variability becomes stronger (weaker) and more (less) regular during cool (warm) periods. Emile-Geay et al. (2007) went on to demonstrate that warming in the ETP during an El Niño event produces persistent northeasterly surface wind anomalies over the Fram and Denmark straits in the North Atlantic that are reminiscent of those during negative phases of the North Atlantic Oscillation (NAO). These wind anomalies produced cooling over the North Atlantic in a pattern consistent with the spatial distribution of

enhanced ice rafted debris in the North Atlantic during the LIA (Bond et al., 2001). Model simulations show that cooling in the North Atlantic during the LIA strengthened the descending limb of the Atlantic Hadley Cell, enhancing the northeasterly trade winds, which further cooled the tropical Atlantic by wind induced evaporation, and shifted the Atlantic Intertropical Convergence Zone (ITCZ) southward (Broccoli et al., 2006; Chiang and Bitz, 2005). These changes in tropical atmospheric circulation would have strengthened the SASM by increasing easterly tropospheric flow over the tropical Andes and enhancing moisture transport to this region. Easterly tropospheric flow would have been further enhanced during the LIA by reduced land-sea thermal gradients (Vizy and Cook, 2007). The implication of these results is that the tropical Pacific ocean-atmosphere response to radiative forcing is capable of driving global climate change and may be responsible for a significant portion of NH cooling during the LIA which then impacted the SASM though ocean-atmosphere dynamics. During periods with enhanced radiative forcing, such as the MCA, the opposite responses would be expected.

3.6.5 SASM response to radiative forcing during the MCA and LIA

The modeled responses to radiative forcing outlined above agree well with climate variability inferred from the Pumacocha record. Interannual $\delta^{18}O_{cal}$ variability is strongest within the sediment core record from the Pumacocha basin during the LIA, when radiative forcing was at its lowest during the last 2300 years (Fig. 17a). Conversely, interannual variability was more subdued during the MCA when radiative forcing was elevated (Fig. 17a). Coral-based SST and ENSO reconstructions from the central tropical Pacific support these observations, indicating that SSTs in the NINO 3.4 region were higher and that ENSO frequency and amplitude were greater during the LIA (Cobb et al., 2003). Further support for an enhanced ENSO comes from a

terrestrial record of El Niño-driven erosional events from Laguna Pallcacocha, Ecuador (2.76°, N79.23° W; 4060 m asl), which shows an increase in clastic sediment flux during the LIA that suggests enhanced El Niño-related precipitation during this interval (Rodbell et al., 1999). Despite the inferred increase in the amplitude and frequency of ENSO during the LIA – modern El Niño events are associated with a weak SASM in the tropical Andes and Amazon basin – overall low $\delta^{18}O_{cal}$ at Pumacocha during the LIA suggests that the SASM was greatly enhanced during this time (Fig. 17b, g). We suggest that this reflects enhanced easterly flow over the tropical Andes in response to the southerly displacement of the ITCZ and enhanced northeasterly trade winds as a result of El Niño-induced cooling in the North Atlantic (Broccoli et al., 2006).

The inferred ITCZ movements and trade wind variability during the LIA and MCA are supported by proxy data from the Cariaco Basin (Fig. 17e). Percent titanium from the Cariaco Basin is interpreted to reflect changes in continental erosion related to precipitation variability controlled by the mean position of the ITCZ where increased (decreased) %Ti reflected wetter (Drier) conditions over the northern Tropics (Haug et al., 2001). Comparing this record with Pumacocha shows that the ITCZ was displaced southward (northward) during the LIA (MCA) when wet conditions prevailed over Pumacocha. Inferred trade wind strength from foraminifera species concentrations in sediments from the Cariaco Basin further supports the model being discussed by showing that the trade winds were strong during the LIA between AD 1400-1570 and AD 1655-1750 (Black et al., 1999), which agrees well with the period of maximum precipitation at Pumacocha.

The influence of the tropical Pacific on NH temperatures and subsequent feedbacks to the tropics via the position of the ITCZ and the strength of the northeasterly trade winds is supported by the striking similarity between Pumacocha $\delta^{18}O_{cal}$ and NH temperature (Moberg et al., 2005).

Like the Pumacocha record, the two most prominent features of NH temperature change during the last 2000 years are the MCA and LIA (Fig. 17g). The timing of these events between the two records are essentially synchronous, showing a weak SASM (high Pumacocha $\delta^{18}O_{cal}$) coincident with warm NH temperatures during the MCA and a strong and highly variable SASM (low and variable Pumacocha $\delta^{18}O_{cal}$) coincident with NH cooling during the LIA. The idea that the ocean-atmosphere response of the tropical Pacific to radiative forcing is transmitted to the North Atlantic via ENSO-like atmospheric teleconnections is consistent with results from a recent European tree-ring study (Trouet et al., 2009). This record shows that the NAO was in a persistent positive phase during the MCA, and was variable, but more negative during the LIA. A modern link between the tropical Pacific and the NAO was described by Hoerling et al. (2001), who documented a positive trend in the NAO during the last 50 years in response to modern warming in the western tropical Pacific.

3.7 SUMMARY AND CONCLUSIONS

The Laguna Pumacocha sediment core $\delta^{18}O_{cal}$ record and inferred SASM intensity reconstruction provides new insight into the modes and mechanisms of tropical and global climate variability over the last 2300 years. In this time frame, the MCA and LIA appear to be the most prominent climate anomalies. Aridity and reduced interannual variability between AD 920-1050 are inferred for the MCA, while a strong SASM from AD 1265-1820 with enhanced interannual variability from AD 1500-1770 is inferred for the LIA. Aridity during the MCA was the combined result of weakened easterly flow over the tropical Andes and a northerly ITCZ due to cooling in the ETP and NH warming driven by positive radiative forcing. During the LIA, the

SASM was enhanced by strong easterlies over the tropical Andes as a result of cooling in the North Atlantic that strengthened the northeasterly trade winds shifted the ITCZ southward. Interannual SASM variability was also stronger during the LIA due to an increase in the amplitude and frequency of ENSO. These climatic responses during the MCA and LIA are the manifestation of the tropical Pacific ocean-atmosphere response to changes in net radiative forcing, which are subsequently transmitted through the global climate system via ENSO teleconnections. During the LIA, negative net radiative forcing produced warming in the ETP and increased ENSO frequency and amplitude as described Clement et al. (1996). Stronger El Niño events enhanced North Atlantic cooling which, in turn, strengthened the northeasterly trade winds and shifted the ITCZ southward. Positive net radiative forcing during the MCA cooled the ETP, which reduced ENSO frequency and amplitude, enhanced warming over the North Atlantic and allowed the ITCZ to maintain a more northerly position. These results indicate that the tropical Pacific is an important component of the global climate system and that it has played a central role in abrupt climate events during at least the late Holocene, and possibly longer.

4.0 TROPICAL SOUTH AMERICAN HYDROLOGIC VARIABILITY DURING THE HOLOCENE: EVIDENCE FOR PRECIPITATION PARTITIONING BETWEEN THE ANDES AND THE AMAZON

4.1 ABSTRACT

An 11,200-year-long decadally resolved oxygen isotope record from Laguna Pumacocha, central Andes Peru, is presented and compared with previously published paleoclimate records from the tropical Andes and recent speleothem records from lowland South America. Oxygen isotope measurements of modern lake water ($\delta^{18}O_{lw}$) and authigenic calcite ($\delta^{18}O_{cal}$) collected in sediment traps and from littoral vegetation indicate that Laguna Pumacocha $\delta^{18}O_{cal}$ tracks $\delta^{18}O_{lw}$, which is identical with mean annual $\delta^{18}O_{precip}$ predicted from gridded IAEA-GNIP data. These relationships provide the basis for using sediment core measurements of $\delta^{18}O_{cal}$ to infer changes in $\delta^{18}O_{precip}$ through time, which, in turn, is controlled by the changing strength of the South American summer monsoon (SASM) through the amount effect. Maximum $\delta^{18}O_{cal}$ values (averaging -10.4‰) characterize the early Holocene between ~10,300 and 9700 cal yr B.P., following an initial abrupt increase at the end of the late Glacial Period. Calcite $\delta^{18}O$ values decreased between 9700 cal yr B.P. and 300 varve year B.P., where minimum $\delta^{18}O_{cal}$ values (averaging -15.8‰) occurred between 700 and 300 varve yr B.P. After 300 varve yr B.P., $\delta^{18}O_{cal}$ increased to the present (-12.4‰). These results are similar to $\delta^{18}O$ and δD from the

lower-resolution Huascaran and Illimani ice cores, respectively, and with $\delta^{18}O$ from Laguna Verdes Baja in the Venezuelan Andes, indicating that the trends in Pumacocha $\delta^{18}O_{cal}$ reflect the general pattern of Holocene climate change observed in records from northern and southern tropical South America. Similarities between the Laguna Pumacocha $\delta^{18}O_{cal}$ record and recently published speleothem $\delta^{18}O_{cal}$ records (archives of low elevation $\delta^{18}O_{precip}$) from lowland South America shows that both regions have become wetter during the Holocene. Differences between the records, however, indicate that the tropical Andes have become wetter relative to lowland tropical South America through the Holocene. Abrupt increases in Andean precipitation inferred from the Laguna Pumacocha record occurred at 5000, 2400 cal yr B.P., and 700 varve yr B.P. The timing of these transitions coincide with major climate shifts in the tropical Andes, such as the reestablishment of the Quelccaya Ice Cap and increasing Lake Titicaca water levels at ~5000 cal yr B.P., high lake stands in Bolivia and further increases in the level of Lake Titicaca at ~2400 cal yr B.P., and the initiation of extreme wet conditions and glacial advances across the Andes between ~700 and 500 cal yr B.P. Notably, globally recognized late Holocene climate events, such as the Medieval Climate Anomaly and Little Ice Age (LIA), are subdued in the lowland speleothem records, but are pronounced in records from the tropical Andes. This suggests that common forcing mechanisms during the late Holocene had a greater impact on the tropical Andes than on lowland tropical South America.

4.2 INTRODUCTION

Hydrologic variability in tropical South America during the late Glacial Period and Holocene has been the focus of considerable research (Abbott et al., 2003; Abbott et al., 1997a; Abbott et al.,

1997b; Baker et al., 2001a; Polissar et al., 2006a; Seltzer et al., 2000; van Breukelen et al., 2008; Wirrmann and De Oliveira Almeida, 1987). Ice cores, lakes sediments, and speleothems suggest that wet/cool conditions prevailed during the late Glacial and that an abrupt shift to arid conditions during the early Holocene was followed by a long-term precipitation increase to the present. These millennial-scale hydrologic changes generally track the precessional increase of Southern Hemisphere insolation during the last 10,000 years, illustrating the importance of orbital forcing on precipitation in tropical South America.

The majority of paleoclimate records used to infer precipitation dynamics over tropical South America during the Late Glacial and Holocene are from the high Andes. This bias in sample locations primarily reflects the lack of sites from the Amazon that contain adequate Holocene-length paleoclimate records. Using high-elevation sites from the Andes to infer large-scale precipitation dynamics over tropical South America relies on an *a priori* assumption that hydrologic shifts in the Andes reflect similar shifts in the hydrology of the Amazon basin. This may be a valid assumption, but the lack of lowland records with sufficient temporal resolution has made this difficult to assess. An additional limitation of previous hydrologic reconstructions is that the interpretation of some of these records (specifically, those from ice caps) is debated with respect to the relative influences of temperature and precipitation.

Recently published oxygen isotope records from speleothems in the Andean foothills of the Peruvian Amazon and southeastern coastal Brazil provide new information about the lowland expression of the SASM from the Late Glacial through the Holocene (Cruz et al., 2005; van Breukelen et al., 2008; Wang et al., 2007). These speleothem records indicate that generally wet conditions during the end of the Late Glacial were replaced by more arid conditions at the beginning of the Holocene, which were then followed by a prolonged increase in precipitation

through the Holocene. Despite being separated by complex topography and tens of degrees of latitude and several degrees of longitude, there are similarities between the speleothem records and their high-elevation counterparts. However, there are subtle, but significant, differences between the low elevation speleothem records and the high elevation lake and ice core records. These differences suggest that there may be unique, elevation-dependent hydrologic responses to similar forcing mechanisms in tropical South America through the Holocene. Unfortunately, the relatively low temporal resolution and age uncertainty in published Andean ice core and lake records precludes sub-millennial-scale comparisons with the low-elevation speleothem records, some of which are decadally-resolved. In order to characterize differences in the evolution of the SASM between the Andes and the Amazon basin during the Holocene, higher-resolution records of Andean hydrology are needed.

Here, we present a new, decadally-resolved, 11,200-year-long $\delta^{18}O$ record from Laguna Pumacocha, a small alkaline lake in the central Peruvian Andes at 10°S and 4300 m above sea level (m asl). Isotopic measurements of modern lake water ($\delta^{18}O_{lw}$) and calcite precipitates ($\delta^{18}O_{cal}$) indicate that Pumacocha $\delta^{18}O_{cal}$ primarily reflects changes in the isotopic composition of precipitation ($\delta^{18}O_{precip}$) and, by inference, the strength of the SASM, with minimal influence from temperature and evaporation changes. We compare our results with previously published ice core and lake sediment records from the high Andes, which demonstrates that precipitation changes are the primary signal captured in these records and that the tropical Andes have responded coherently at millennial time-scales to SASM variability during the Holocene. We then examine precipitation partitioning between the high Andes and the Amazonian lowlands over the last 10,000 years by comparing the Laguna Pumacocha $\delta^{18}O_{cal}$ record with newly available speleothem records of SASM variability from the Amazon basin.

4.3 STUDY AREA

Laguna Pumacocha is a small alkaline headwater lake within the Amazon basin that is located on the eastern flank of the Peruvian Andes at 4300 meters above sea level (m asl; 10.69882°S, 76.06110°W; Fig. 18, 19a). The lake is 0.1 km^2 and is set in a glacially carved cirque with headwalls that reach a maximum elevation of 4600 m asl and an area of 1.7 km^2. The catchment is currently unglaciated, and there is no evidence of glaciation during the Holocene, although there are several lateral and recessional moraines that were likely deposited during the Last Glacial Maximum (Fig. 19b). Presently, the watershed is free of trees and the landscape is dominated by tussock grasses. The lake basin is 23.5 m deep with a flat bottom and steep sides (Fig. 19b). A broad marshy area that varies between 10 and 50 m in width surrounds the lake. This fringing wetland reduces the influx of allochthonous material to the lake during wet season storm events, which in turn limits the sediment composition to autochthonous (i.e., authigenic mineral precipitates and organic matter produced in lake) and eolian material.

The modern lake is at its overflow point and has a volume of 1.37 x 10^6 m^3 and a surface area of 0.094 km^2 (Fig. 19a). Although Pumacocha overflows year-round, dry season discharge is small relative to the overall lake volume. Two small springs to the north and south feed the basin, but this inflow is negligible compared to the amount of precipitation received during the SASM (~1,100 to 1,500 mm at Cerro de Pasco, ~30 km east of the Pumacocha watershed). Laguna Pumacocha is considered a meromictic lake, and the water column is therefore perennially stratified with the oxycline, chemocline and thermocline occupying depths between ~6 and 8 m. Bedrock within the watershed is comprised of primarily of Jurassic marine limestone of the Chambara Formation (Quispensivana, 1996). Chemical weathering of this

formation supplies significant quantities of dissolved HCO_3^- and Ca^{2+} ions to the basin, promoting alkaline conditions (140 to 220 ppm HCO_3^-) within the lake and saturation with respect to calcite throughout the year.

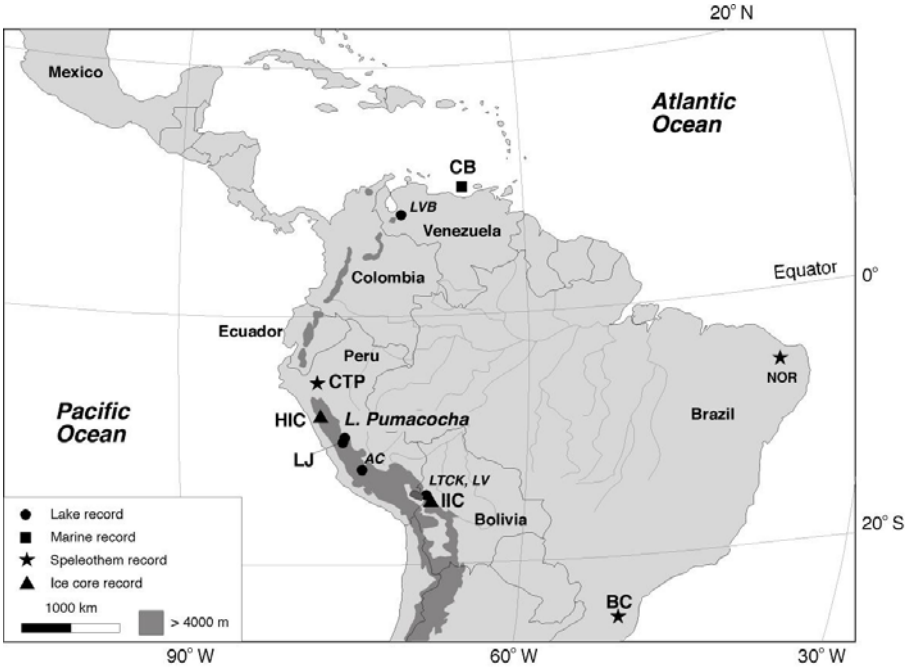

Figure 18 Map of South American tropics with locations of sites discussed in the text. CB = Cariaco Basin, LVB = Laguna Verdes Baja, CTP = Cueva del Tigre Perdido, HIC = Huascaran ice core, LJ = Laguna Junin, AC = Laguna Azulcocha, LTCK = Laguna Taypi Chaka Kkota, LV = Laguna Viscachani, IIC = Illimani ice core, BC = Cueva Botuvera, NOR = Nordeste Region

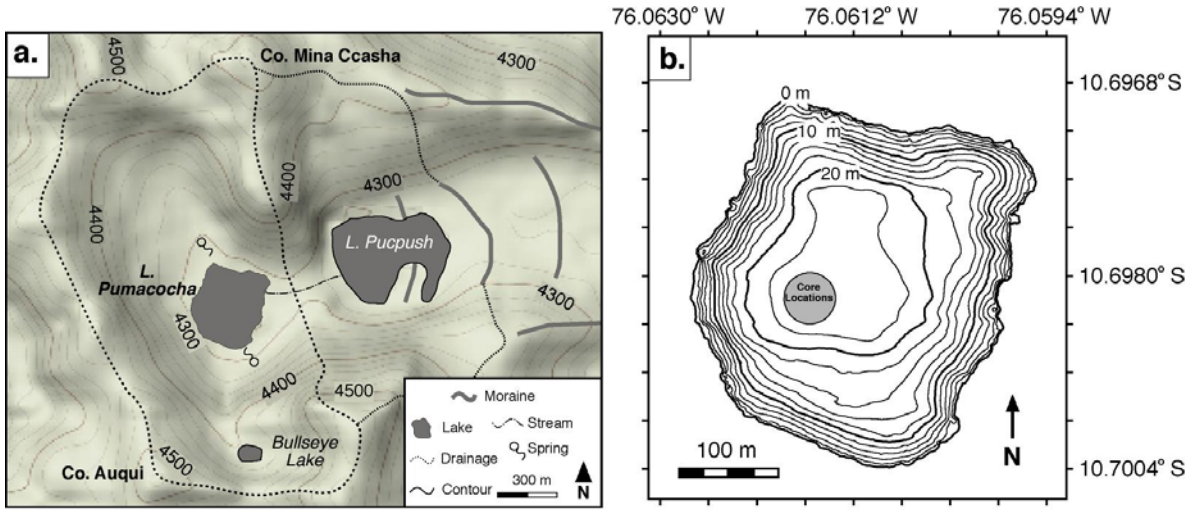

Figure 19(a) Topographic map of the Pumacocha (long dash line) and Pucpush catchments (short dash line). (b) Bathymetric map of Pumacocha.

4.4 METHODS

4.4.1 Core collection

Multiple sediment cores were retrieved from the deepest part of Laguna Pumacocha in 2005 and 2006 using a modified Livingstone square-rod piston corer (Fig. 19b; Wright et al., 1984). Consecutive drives were overlapped by ~20.0 cm to ensure continuous sediment recovery. Undisturbed surface sediments were captured in several freeze cores collected between 2006 and 2008 (Table 10). In total, a composite 579.0 cm record of sediment accumulation was extracted from the lake. Dense glacial deposits below this depth prevented further core recovery.

Table 10 Name, type, and length of cores collected from Pumacocha. The (*) denotes which cores were used in the final composite record

Core	Type	Length (cm)	Sediment interface
A-05*	Livingstone	535	No
B-05	Surface	70	Yes
C-06*	Livingstone	579	No
D-06	Surface	145	Yes
E-06*	Freeze core	55	Yes
A-07	Freeze core	62	Yes
B-07*	Freeze core	58	Yes
C-07	Freeze core	60	Yes
D-07*	Freeze core	65	Yes
A-08	Freeze core	69	Yes
B-08*	Freeze core	72	Yes
C-08	Freeze core	72	Yes
D-08	Freeze core	69	Yes
E-08	Freeze core	70	Yes
F-08	Freeze core	74	Yes

4.4.2 Core imaging

High-resolution digital images of the Livingstone cores were acquired with a line-scanning digital camera at the University of Minnesota Limnological Research Center. Digital images of the freeze cores were acquired at the University of Pittsburgh with a fixed position digital camera housed in a light box. Cameras at both sites were equipped with full spectrum fluorescent lights.

Scanning electron microscope (SEM) images of the sediments were with a Philips XL-30 field emission SEM equipped for imaging in secondary electron and backscatter electron modes. Sediment mineralogy was determined by X-ray diffraction (XRD) using a Philips X'pert diffractometer. SEM and XRD analyses were performed at the Materials Micro-Characterization Laboratory of the Department of Mechanical Engineering and Materials Science, Swanson School of Engineering, University of Pittsburgh.

4.4.3 Modern sedimentation and limnology

Modern authigenic carbonate was captured in sediment traps deployed in the deepest part of Laguna Pumacocha between August 2006 and May 2007 and collected from littoral vegetation in August 2006 and May 2008. Lake dynamics and watershed climate are represented by lake-level and lake-surface temperature from a Solinst® Levellogger® deployed in a fixed position 125 cm below the lake surface, air temperature and barometric pressure from a land-based Solinst® Barologger®, and relative humidity and air temperature from a LogTag® data recorder located ~500 m down valley. These variables were measured continuously at 4-hour intervals from May 29, 2007 to May 11, 2008. Temperature, pH, dissolved oxygen and specific conductivity were measured with a Hydrolab® MiniSond® 4a at ~1 m intervals in June 2005 August 2008 and

May 2007. Water samples for oxygen and hydrogen isotopic analysis and alkalinity were collected from the coring site during summer field season between June 2005 and May 2008. Water samples were for oxygen and hydrogen isotopic analysis were also collected monthly between August 15, 2006 and May 25, 2008. Springs feeding Pumacocha were sampled for water isotopes and alkalinity in May 2007 and 2008.

Alkalinity was measured in the field using a Hatch® digital tritrator kit with 1.6 N H_2SO_4. Samples were titrated to an endpoint pH of 4.0 and the volume of acid consumed was used to calculate moles of HCO_3^-. Oxygen and hydrogen isotopic ratios were measured at the University of Arizona Environmental Isotope Laboratory. The reported precision is 0.08‰ for $\delta^{18}O$ and 0.11‰ for δD. All values are reported in standard delta notation as the per mil (‰) deviation from Vienna standard mean ocean water (VSMOW).

4.4.4 Age control

Age control was established using both radiometric techniques and couplet counting. Lead-210, ^{226}Ra, and ^{137}Cs was measured at ~1 cm intervals between 0.0 and 30.0 cm from freeze core D-08 by direct gamma counting using an EG & G Ortec GWL high purity germanium well detector (Appleby et al., 1986; Schelske et al., 1994) at the University of Florida's Land Use and Environmental Change Institute (Table 11). Eighteen radiocarbon (^{14}C) ages were measured by accelerator mass spectrometry (AMS) on selected charcoal fragments at the University of California, Irvine, W. M. Keck Carbon Cycle Accelerator Mass Spectrometry Laboratory (Table 12). All AMS ^{14}C samples were cleaned and pretreated at the University of Pittsburgh's Radiocarbon Laboratory according to standard protocols (Abbott and Stafford, 1996). AMS ^{14}C ages were calibrated to years before present (cal yr B.P.; present = AD 1950) with the online

program CALIB 5.0 (Stuiver and Reimer, 1993). The reported ages are the 2σ median probability age with errors that are one-half of the 2σ age range.

Couplet-count-based ages constrain the upper 104.5 cm. Couplets were counted from high-resolution digital images of freeze core B-08 and the uppermost sediments from Livingstone core C-06 following the methods of Francus et al. (2002). A minimum of four counts were performed on each core to ensure data quality and to derive a cumulative age error estimate (1%). Ages based on couplet counts are referred to as varve years before present (varve yr B.P.; present = AD 1950).

Table 11 Pumacocha ^{210}Pb, ^{226}Ra and ^{137}Cs results from freeze core D-08

Top depth (cm)	Bottom depth (cm)	Dry BD g/cc	Pb-210 activity (dpm/g)	Pb-210 1σ error	Ra-226 activity (dpm/g)	Ra-226 1σ error	Excess Pb-210 activity (dpm/g)	Excess Pb-210 activity 1σ error	Cs-137 activity (dpm/g)	Cs-137 1σ error
0	0.85	0.0364	18.328	0.623	1.989	0.672	16.521	0.926	0.000	0.010
0.85	1.75	0.0454	29.019	0.871	1.895	0.816	27.434	1.207	0.000	0.007
1.75	3.1	0.0536	23.525	0.958	1.219	0.988	22.565	1.392	0.000	0.005
3.1	4.2	0.0521	16.231	0.855	0.507	0.660	15.907	1.093	0.000	0.007
4.2	5.3	0.0645	32.196	0.775	1.024	1.306	31.539	1.537	0.139	0.037
5.3	6.25	0.0965	28.543	1.014	1.084	0.339	27.789	1.082	0.000	0.017
6.25	7.45	0.0719	22.291	0.986	0.698	0.930	21.854	1.372	0.244	0.066
7.45	8.7	0.0568	26.211	1.269	0.684	0.990	25.838	1.629	0.000	0.008
8.7	10.5	0.0808	30.815	1.087	1.486	1.379	29.689	1.777	0.790	0.103
10.5	11.05	0.1139	29.697	0.473	2.348	0.135	27.688	0.499	0.005	0.011
11.05	12.1	0.1252	22.434	0.719	2.429	0.151	20.258	0.743	0.000	0.003
12.1	13.1	0.1063	25.177	0.726	2.583	0.909	22.881	1.178	0.000	0.014
13.1	14.45	0.1042	19.369	0.756	0.597	0.179	19.012	0.787	0.082	0.035
14.45	15.45	0.1119	17.914	0.655	0.747	0.723	17.388	0.988	0.080	0.030
15.45	16.5	0.0861	18.642	0.764	1.060	0.760	17.810	1.091	0.161	0.046
16.5	17.5	0.1324	11.980	0.282	1.208	0.418	10.912	0.511	0.000	0.007
17.5	18.5	0.1096	10.103	0.464	1.087	0.392	9.136	0.615	0.000	0.003
18.5	19.7	0.1529	6.955	0.344	1.144	0.573	5.890	0.677	0.013	0.016
19.7	20.5	0.1244	6.560	0.273	1.037	0.203	5.583	0.344	0.017	0.014
20.85	21.7	0.1762	4.442	0.156	0.879	0.562	3.611	0.591	0.018	0.009
21.7	22.9	0.1934	4.178	0.144	0.831	0.072	3.394	0.164	0.011	0.008
22.9	24.3	0.1881	3.699	0.190	1.502	0.139	2.228	0.239	0.043	0.014
24.3	25.35	0.1756	2.072	0.157	0.997	0.130	1.091	0.207	0.000	0.003
25.35	26.4	0.1735	2.619	0.137	1.079	0.312	1.564	0.346	0.000	0.003
26.4	27.5	0.1771	1.419	0.156	0.590	0.329	0.840	0.369	0.026	0.015
27.5	28.75	0.1799	1.845	0.147	1.046	0.171	0.811	0.229	0.000	0.003
28.75	29.75	0.1366	2.368	0.217	1.460	0.124	0.922	0.254	0.000	0.004
29.75	30.7	0.1521	1.128	0.142	0.789	0.365	0.344	0.398	0.000	0.003

Table 12 Radiocarbon ages and associated data from Laguna Pumacocha

UCI #	Core	Top depth (cm)	Bottom depth (cm)	Material	Fraction modern	^{14}C age (yr B.P.)	2-σ median calibrated age range (cal yr B.P.)	2-σ calibrated median age (cal yr B.P.)	One-half 2-σ calibrated range (years ±)
32685	A-05	37.5	41.5	Charcoal	0.9314	570	578-652	600	35
25283	A-05	49.5	51.5	Charcoal	0.9454	450	483-530	510	25
22751	A-05	62	64	Charcoal	0.9258	620	551-658	600	55
32683	A-05	72.6	75.6	Charcoal	0.9108	750	646-773	690	65
22752	A-05	81.5	82.5	Charcoal	0.9267	610	520-673	600	75
22753	A-05	103	105	Charcoal	0.8754	1070	929-1016	980	45
22754	A-05	121	123	Charcoal	0.8546	1260	1077-1283	1200	105
32682	A-05	129	131	Charcoal	0.8420	1380	1220-1390	1300	85
22756	A-05	156	159	Charcoal	0.8064	1730	1549-1714	1640	85
32681	A-05	171.7	173.7	Charcoal	0.7456	2360	2299-2621	2430	160
25284	A-05	177.7	179.7	Charcoal	0.7233	2605	2695-2794	2740	50
32684	A-05	211.45	215.45	Charcoal	0.7309	2520	2466-2745	2590	140
25285	A-05	273.9	275.9	Charcoal	0.6844	3045	3205-3356	3270	75
25286	A-05	351.3	353.3	Charcoal	0.5959	4160	4576-4772	4700	100
25287	A-05	381.3	383.3	Charcoal	0.5949	4170	4572-4837	4710	135
43544	E-06	420.7	421.7	Charcoal	0.4722	6030	6675-7032	6890	180
43545	E-06	527.3	528.3	Charcoal	0.3348	8790	9579-9964	9830	195
43546	E-06	562.3	565.3	Charcoal	0.2868	10030	11247-11838	11560	295

4.4.5 Carbonate sampling and stable isotope measurements

The uppermost 210 individual carbonate lamina from freeze core B-08, B-07, and D-07 were sampled for carbonate isotope ($\delta^{18}O_{cal}$ and $\delta^{13}C_{cal}$) analysis. Additional samples for carbonate isotope analysis were collected from Livingstone cores A-05 and E-06. Laminated portions of cores A-05, C-01 and E-06 were sampled at 1 mm intervals. Massive to banded sections were sampled at 2.5 mm intervals.

All samples for carbonate isotope analysis were soaked for a minimum of 24 hours in 7% H_2O_2 and sieved at 63 μm. The < 63 μm fraction was collected, soaked in a 50% commercial bleach solution for 6 to 8 hours, rinsed three times with deionized water, freeze dried, and

homogenized prior to analysis. Samples were measured at the University of Arizona using an automated carbonate preparation device (Thermo Finnigan® KIEL-III) coupled to a gas-ratio mass spectrometer (Finnigan® MAT 252). Samples at the University of Pittsburgh were measured with a GV Instruments, Ltd. (now Isoprime, Ltd., a subsidiary of Elementar Analysensysteme) Isoprime™ stable isotope ratio mass spectrometer and a Multi-Prep™ inlet module and Gilson auto sampler. Powdered carbonate samples were reacted with dehydrated phosphoric acid under vacuum at 70°C (Arizona) and 90°C (Pittsburgh). All results are reported in standard delta notation as the per mil (‰) deviation from Vienna Pee Dee Belemnite (VPDB), unless otherwise stated. Sample measurements were calibrated based on repeated measurements of NBS-19 and NBS-18. Precision is ± 0.1 and 0.13‰ for $\delta^{18}O$ and ± 0.06‰ and 0.09‰ for $\delta^{13}C$ (1σ), at the University of Arizona and the University of Pittsburgh, respectively. Internal sample reproducibility was determined by replicate sample measurements and is ± 0.02‰ for $\delta^{18}O$ and ± 0.03‰ for $\delta^{13}C$.

4.5 RESULTS

4.5.1 General Sedimentology

Light gray to tan laminated detrital carbonate sediments dominate the bottommost portions of the core, from 579.0 cm to 565.2 cm (Fig. 20; Table 13). Above 565.2 cm, sediments abruptly transition to a massive black gyttja that, in turn, grades into a massive to banded dark green to black gyttja by ~550.0 cm depth. Between ~550.0 and 176.2 cm depth, there are three sections with laminated sediments between 550.0 and 440.0 cm, 365.0 and 361.7 cm, and 211.5 and

210.0 cm. At 176.2 cm, massive to banded sediments abruptly become finely laminated. Above ~460.0 cm, the sediments become a light tan color. Well preserved laminations are continuous to the top of the core, with the exception of four discrete massive intervals that are dark green in color.

Table 13 Depths and ages of sediment transitions in the Pumacocha core

Depth (cm)	Age	Time unit	Sediment type
0 to 103.4	-57 to 1110	varve yr B.P.	Laminated couplets
103.4 to 123.5	1110 to 1490	cal yr B.P.	Massive & banded
123.5 to 158.5	1490 to 2010	cal yr B.P.	Laminated couplets
158.5 to 162.5	2010 to 2060	cal yr B.P.	Massive & banded
162.5 to 166.5	2060 to 2110	cal yr B.P.	Laminated couplets
166.5 to 171.0	2110 to 2170	cal yr B.P.	Massive & banded
171.0 to 173.0	2170 to 2190	cal yr B.P.	Laminated couplets
173.0 to 210.2	2190 to 2600	cal yr B.P.	Massive & banded
210.2 to 211.5	2600 to 2620	cal yr B.P.	Laminated couplets
211.5 to 361.7	2620 to 4810	cal yr B.P.	Massive & banded
361.7 to 365.0	4810 to 4885	cal yr B.P.	Laminated couplets
365.0 to 440.0	4885 to 6875	cal yr B.P.	Massive & banded
440.0 to 565.2	6875 to 11530	cal yr B.P.	Laminated & banded
565.2 to 579.1	11530 to 12100	cal yr B.P.	Laminated glacial clay

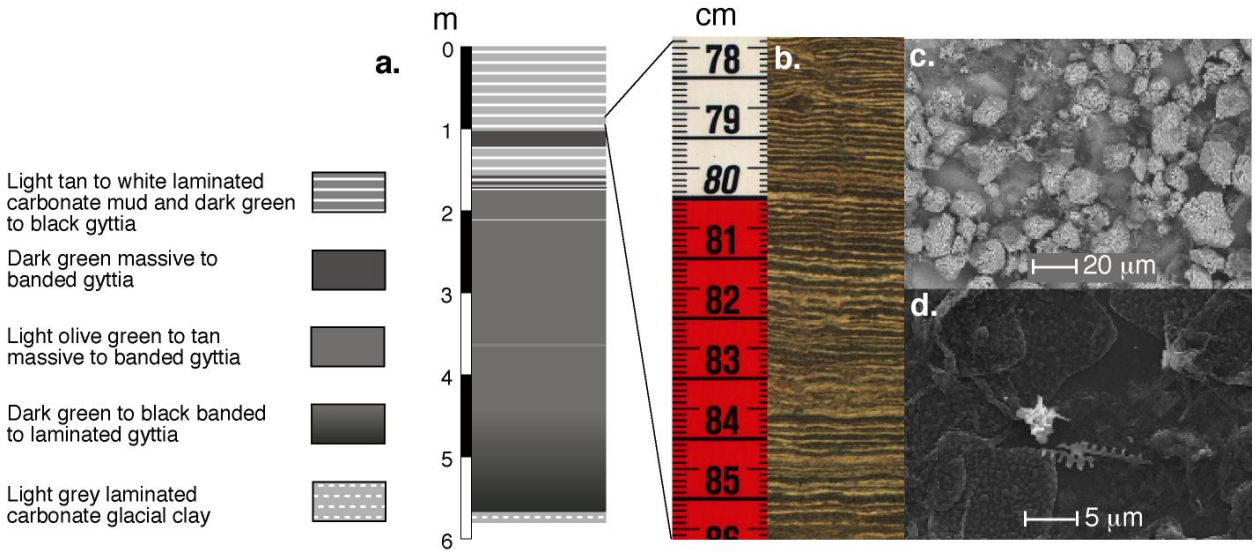

Figure 20 Composite stratigraphic column of the Pumacocha sediment record. (b) A high-resolution digital image from the upper portion of the Pumacocha sediment record showing a typical section of finely laminated millimeters scale varves. (c) Representative SEM image showing the euhedral calcite crystals that

comprise the sediments in the light lamina from the varved portion of the Pumacocha sediment record. (d) Representative SEM image showing the organic matter that comprises the dark lamina form the varved portion of the Pumacocha record.

4.5.2 Couplet Sedimentology

X-ray diffraction, SEM images, and high-resolution digital imagery indicate that the couplets between 176.2 and 0.0 cm consist of discrete dark green organic rich layers overlain by tan to white layers of euhedral calcite crystals (Fig. 20c, d). This couplet structure and compositional regularity suggests continuous rhythmic deposition in the uppermost portion of the Laguna Pumacocha record. Distinct couplet sequences are easily correlated between the network of cores from the lake, and demonstrates that sediment deposition is spatially consistent.

4.5.3 Age control

The AD 1963 ^{137}Cs maximum occurs between 8.7 and 10.5 cm in freeze core D-08 (Fig. 21a; Table 11). Based on the mean depth of this radiometric marker, we estimate a sedimentation rate of 0.21 cm yr^{-1}. The depth interval containing the AD 1963 ^{137}Cs peak also contains the AD 1963 couplet as determined by couplet counting. The sedimentation rate based on the mean depth of the AD 1963 couplet (0.20 cm yr^{-1}) agrees well with ^{137}Cs-based sedimentation rate. These results support the interpretation that the couplets are annual.

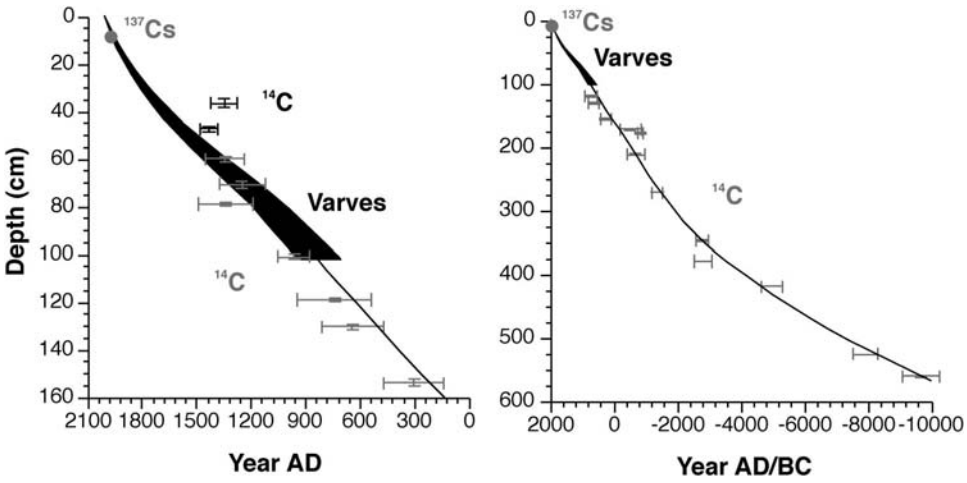

Figure 21 The left graph shows the varve-^{137}Cs-^{14}C age model for the upper 160 cm. Ages based on couplet counts have an estimated error of +/- 1% (shown with the increasing error range in black). Error ranges for ^{14}C are shown with horizontal bars for ages, and vertical bars for depth. The Right graph shows the entire age model for the last 11,500 years. A 6th order polynomial was fit to these data to derive the final age depth model.

Six AMS ^{14}C ages were measured on charcoal fragments from the upper 30 cm of the Laguna Pumacocha record (Fig. 21a; Table 12). The four lower ages, despite one being reversed, are in good agreement with the couplet-count-based ages (Fig. 21a; Table 12). Age reversals within the core may be the result of sample contamination, and/or the presence of 'old carbon' washed into the system from the surrounding watershed, or littoral vegetation that was burned and introduced to the sediments. Despite the reversals, the AMS ^{14}C ages are generally in good agreement with ages based on couplet counts.

Excess ^{210}Pb activities demonstrate a plateau between 0.0 and 8.7 cm and then an exponential decrease below 8.7 cm (Table 11). Application of a linear accumulation model below the plateau region yields a sediment accumulation rate of 0.35 cm yr^{-1}. This is higher than the accumulation rates estimated from ^{137}Cs and couplet counts and underestimates the age of the ^{137}Cs peak. Typically, constant excess ^{210}Pb activities in the uppermost sediments is attributed to

sediment mixing, either from bioturbation or disturbance during the coring process (Appleby and Oldfield, 1983). However, deposits within the core are finely laminated to the sediment-water interface, indicating that mechanical mixing has not occurred. Constant ^{210}Pb activities in the uppermost sediments, despite no physical mixing, have been observed in other varved lakes (e.g., Lake Zurich; Erten et al., 1985). This phenomenon may be explained by the existence of a mobile ^{210}Pb fraction at the dissolved and/or colloid level that quickly moves through pore waters within the upper most sediments until compaction precludes interstitial pore fluid movement (Abril, 2003). This process can affect ^{210}Pb while not influencing the ^{137}Cs profile (Abril, 2003).

The strong agreement between the ^{137}Cs, AMS ^{14}C, and couplet counts supports the interpretation that the Laguna Pumacocha sediment core couplets are varves. We therefore rely solely on linearly interpolated ages based on couplet counts for age control in the upper 104.5 cm of the Pumacocha sediment record. Below 104.5 cm, we fit a 4th order polynomial to the remaining 12 AMS ^{14}C ages (Table 12).

4.5.4 Modern controls on Pumacocha $\delta^{18}O_{lw}$

Near-monthly surface water sample collection at Laguna Pumacocha spanned two dry and two wet seasons between August 2006 and May 2008 (Fig. 22). Lake water δ^{18}O varied the most

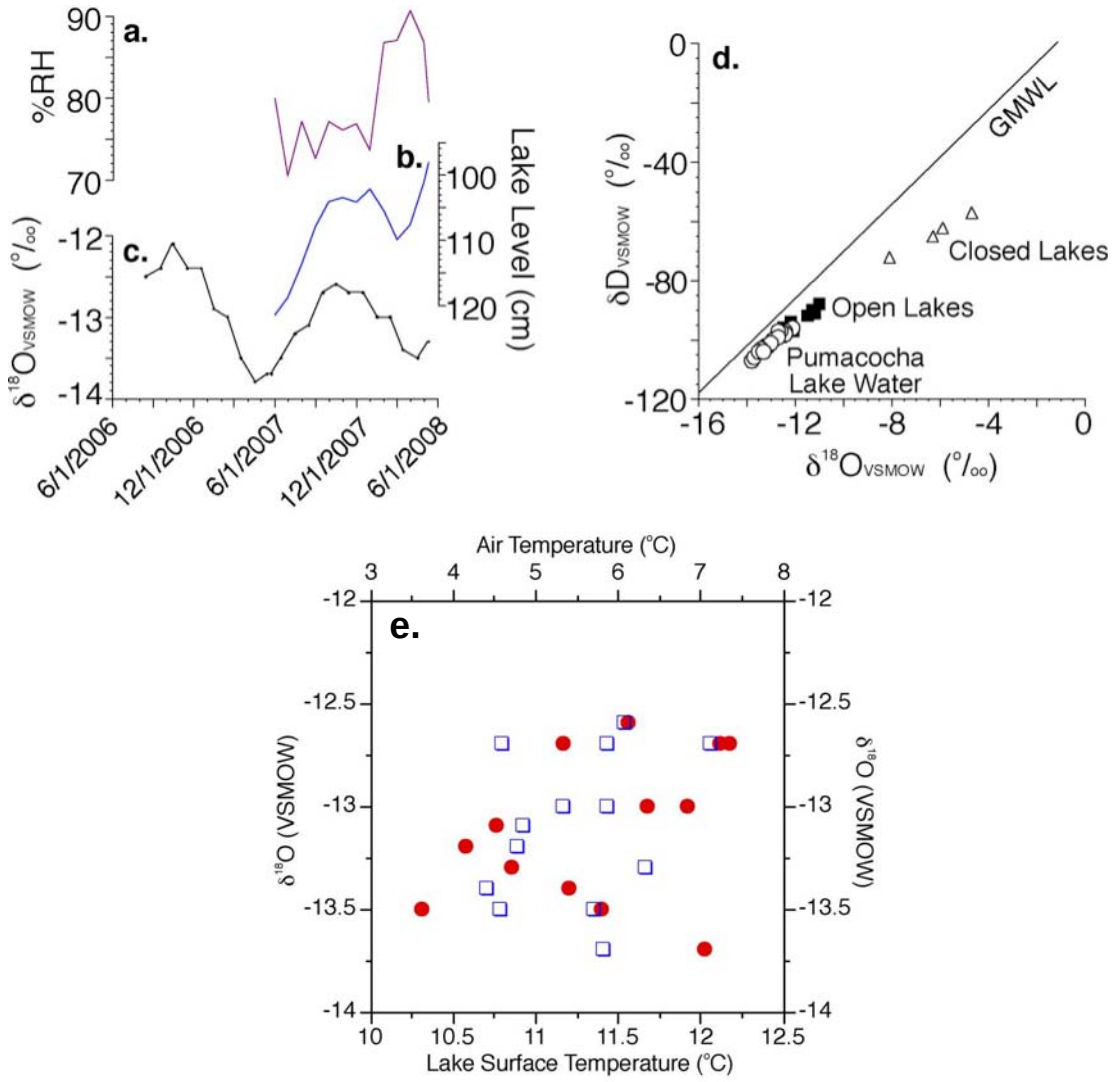

Figure 22 Modern (a) percent relative humidity (%RH), (b) lake level, and (c) surface $\delta^{18}O_{lw}$ measurements from Pumacocha. (d) Plot of surface water and $\delta^{18}O_{lw}$ from Pumacocha (black circles) and other open (open squares) and closed (open triangles) tropical Andean lakes. These lakes comprise a local evaporation line that plots off the so-called global meteoric water line (GMWL). (e) Air and surface temperature plotted against lake water oxygen isotopic composition.

between 2006/2007 (1.7‰); $\delta^{18}O_{lw}$ was -12.1‰ during October 2006 and -13.8‰ in April 2007. Less variability (0.9‰) in lake water oxygen isotopic composition was observed between the 2007 wet and 2008 dry seasons; $\delta^{18}O_{lw}$ was -12.6‰ in October 2007 and -13.5‰ in April 2008.

Comparing monthly average $\delta^{18}O_{lw}$ and lake characteristics with local climatic variables suggests that $\delta^{18}O_{lw}$ is inversely related to lake-level and relative humidity (%RH) (i.e., periods of high $\delta^{18}O_{lw}$ correspond to low lake levels and low %RH, and vice versa) (Fig. 22a-c). Air temperature and lake-surface temperature show no clear relationship with $\delta^{18}O_{lw}$ (Fig. 22e).

4.5.5 Modern carbonate

Authigenic carbonate collected within the littoral zone of the Pumacocha basin in August 2006 and May 2008 exhibited $\delta^{18}O_{cal}$ values of -12.2‰ and -12.4‰, respectively. Sediment trap carbonate collected between August 2006 and May 2007 produced average $\delta^{18}O_{cal}$ values near -12.8‰ with a maximum of -12.4‰ and a minimum of -13.2‰. Converted from VPDB to VSMOW (-13.1‰), sediment trap $\delta^{18}O_{cal}$ is within analytical error of annual average $\delta^{18}O_{lw}$ for the respective time periods when the carbonate was recovered (-12.9‰ VSMOW). This suggests that carbonate within the Pumacocha basin is precipitated in equilibrium with lake water and that $\delta^{18}O_{cal}$ reflects annual average $\delta^{18}O_{lw}$.

4.5.6 Holocene oxygen isotope trends

The oxygen isotopic composition of calcite in Laguna Pumacocha was low (varying between -13.8 and -14.5‰) at the end of the late Glacial (Fig. 23a). Between 11,100 and 10,300 cal yr B.P., mean $\delta^{18}O_{cal}$ values increased rapidly to -10.5‰. Maximum $\delta^{18}O_{cal}$ values (averaging -10.4‰) occurred near 9800 cal yr B.P. After 9800 cal yr B.P., $\delta^{18}O_{cal}$ values decreased

gradually. Minimum $\delta^{18}O_{cal}$ values (averaging -15.8‰) were achieved by ~370 varve yr B.P. After 370 varve yr B.P., $\delta^{18}O_{cal}$ values increase markedly.

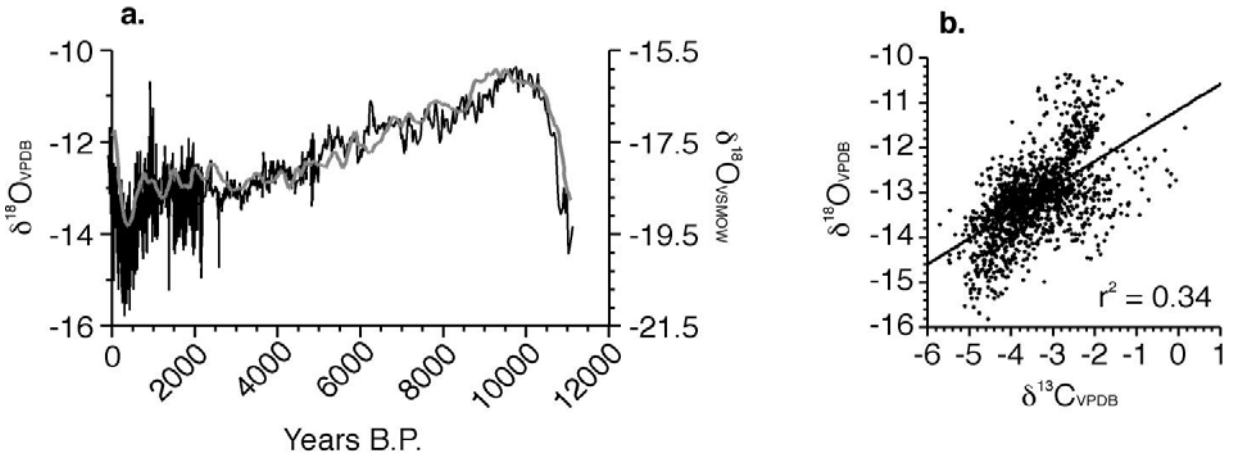

Figure 23(a) Plot of $\delta^{18}O_{cal}$ from Pumacocha (black line) between 11,200 cal yr B.P. and -57 varve yr B.P. (B.P. = AD 1950) plotted with Huascaran $\delta^{18}O$ (gray line; VSMOW). (b) Plot of $\delta^{13}C_{cal}$ and $\delta^{18}O_{cal}$ measurements from Pumacocha.

$\delta^{18}O_{cal}$ variability increases dramatically after 2300 cal yr B.P. (Fig. 23a). This change coincides with the transition from massive to finely laminated sediments. Increased variability after this transition is likely the result of a decrease in the sampling interval (2.5 mm to 1 mm), which reduced signal smoothing, and increased preservation of high frequency variability in the finely laminated sediments as a result of reduced bioturbation after 2300 cal yr B.P. A detailed description and analysis of the high-frequency variability during the period from -57 to 2300 varve yr B.P. can be found in Chapter 3.

4.6 DISCUSSION

4.6.1 Environmental significance of Pumacocha $\delta^{18}O_{cal}$

The isotopic mass balance of a lake is controlled by the isotopic composition of its inputs (i.e., groundwater, precipitation, surface inflow) and outputs (i.e., groundwater loss, surface outflow, and evaporation; Gat, 1996). Laguna Pumacocha is located in a perched catchment, topographically isolated from nearby watersheds and inter-valley groundwater flow. This limits the influence of groundwater on the lake's isotopic composition. Because the lake is a headwater, surface inflow is restricted to the immediate watershed, which is very small (1.67 km^2). This limits evaporative modification of surface water during transport to the lake after a precipitation event (Fig. 19a). Evaporative enrichment of lake surface waters also appears to be a negligible influence on mean annual $\delta^{18}O_{lw}$. Predicted mean annual $\delta^{18}O_{precip}$ based on interpolated IAEA-GNIP data (-13.10 ± 1.5‰) (Bowen and Wilkinson, 2002; Bowen and Revenaugh, 2003; Bowen et al., 2005) is identical within analytical error to annual $\delta^{18}O_{lw}$ between June 11, 2005 and May 11, 2008 (-13.00‰). These factors suggest that Laguna Pumacocha is an open hydrologic system and that $\delta^{18}O_{lw}$ tracks regional $\delta^{18}O_{precip}$. A poor linear correlation ($r^2 = 0.34$, $p < 0.001$) between $\delta^{18}O_{cal}$ and $\delta^{13}C_{cal}$ in Laguna Pumacocha during the entire 11,200-year-long record supports the inference that that Pumacocha has been an open system throughout the late Glacial and Holocene, and that the relationship between $\delta^{18}O_{lw}$ and $\delta^{18}O_{precip}$ was consistent during this time (Fig. 23b; Li and Ku, 1997). It may be argued that short periods of profound aridity at Pumacocha, such as during the early Holocene, may have resulted in an increase in the influence of evaporation on the lakes isotopic mass balance.

However, the linear relationship between $\delta^{18}O_{cal}$ and $\delta^{13}C_{cal}$ from 10,660-8330 cal yr B.P. (the period with the highest $\delta^{18}O_{cal}$ in the record) is incredibly poor ($r^2 = 0.05$; $p < 0.001$), which suggests that even during periods of enhanced aridity, Pumacocha appears to have remained an open system, leaving the $\delta^{18}O_{lw}$-$\delta^{18}O_{precip}$ relationship intact. Groundwater outflow from Pumacocha was not directly measured, but given the strong agreement between estimated mean annual $\delta^{18}O_{precip}$ and mean annual $\delta^{18}O_{lw}$, we assume that groundwater outflow plays a minimal role in modifying the lakes isotopic mass balance. Surface outflow from the lake measured in May 2007 was 3.32×10^5 m^3 yr^{-1}, which is ~25% of the total modern lake volume (1.3×10^6 m^3). However, the outflow likely increases during the monsoon season (DJF) to equal inflow since the volume of water that falls over the watershed during an average wet season is nearly double the volume of the lake. As a result, the residence time of water in the upper portion of the water column is estimated to be one year or less, which allows $\delta^{18}O_{lw}$ to reflect $\delta^{18}O_{precip}$.

Lake carbonate oxygen isotopic composition is a function of the initial $\delta^{18}O_{lw}$ and the temperature at which the calcite is precipitated (Kim and O'Neil, 1997; O'Neil et al., 1969). Monthly average lake surface temperatures at Pumacocha varied by 1.2°C between May 29, 2007 and May 11, 2008, which equates to a ~0.3‰ shift in $\delta^{18}O_{cal}$ (Fig. 22a; Kim and O'Neil, 1997). However, $\delta^{18}O_{cal}$ varied by as much as 1.7‰ during this same interval, which is much greater than can be explained by temperature-controlled fractionation alone, and therefore likely reflects changes in the isotopic composition of precipitation (Fig. 22a). On longer time scales, there is evidence from speleothems in the Andean foothills of the Peruvian Amazon (1000 m asl) that Holocene temperatures have been stable about a mean and that anomalies have not exceeded ~ ± 2°C (van Breukelen et al., 2008). One of the largest Holocene glaciations recognized in the Andes occurred during the Little Ice Age (LIA; Rabatel et al.). Estimates based on changes in

equilibrium line altitudes from the Cordillera Real in northern Bolivia suggest a modest LIA cooling of 1.1 to 1.2°C between 4430 and 4780 m asl relative to the present (Rabatel et al., 2008). Taking into account temperature controlled fractionation during the formation of precipitation from water vapor (~ +0.6‰ per ˚C; Rozanski et al., 1992) and subsequently calcite from lake water (-0.24‰ per ˚C; Kim and O'Neil, 1997), temperature shifts of these magnitudes would alter $\delta^{18}O_{cal}$ by 0.4 to 0.5‰. This shift is much smaller than the observed 1.8‰ difference between the LIA and today. Although temperature is incorporated into the Laguna Pumacocha $\delta^{18}O_{cal}$ record, it likely only accounts for a very small portion of the observed variability. If temperature the dominant signal in the Pumacocha record, the 5.6‰ decrease in $\delta^{18}O_{cal}$ from the early Holocene to the LIA would reflect a ~16°C temperature decrease during the Holocene. This is much too large to be realistic, particularly since mean annual insolation has increased in the Southern Hemisphere during the Holocene, which would serve to raise, not lower, mean annual temperatures (Laskar et al., 2004; Paillard et al., 1996).

The isotopic composition of precipitation over tropical South America, and therefore Laguna Pumacocha, is primarily controlled by the amount of precipitation, or the strength of the SASM (Vuille and Werner, 2005). Given the evidence that $\delta^{18}O_{cal}$ reflects $\delta^{18}O_{lw}$, which ultimately is controlled by changes in $\delta^{18}O_{precip}$ related to SASM variability, we interpret the Laguna Pumacocha $\delta^{18}O_{cal}$ record as an archive of SASM intensity (i.e., the amount of SASM precipitation). This interpretation is supported by the similarities between the magnitude and direction of trends in the Huascaran and Pumacocha isotope stratigraphies (Fig. 23a). It could be argued that arid early Holocene aridity influenced both records via sublimation/evaporation. However, ice core records are probably not significantly affected by isotopic enrichment through sublimation because studies have shown that only the surface layer is impacted and that this

layer is often scoured away by wind erosion (Hardy et al., 1998). At Pumacocha, the poor correlation between $\delta^{13}C_{cal}$ and $\delta^{18}O_{cal}$ between 10,660-8330 cal yr B.P. suggests that the lake was hydrologically open during the early Holocene and that evaporation did not significantly impact the $\delta^{18}O_{lw}$-$\delta^{18}O_{precip}$ relationship. Given the evidence against a temperature effect on $\delta^{18}O_{cal}$ at Pumacocha, the good correlation between Pumacocha and Huascaran during the last 11,200 years ($r^2 = 0.79$; $p < 0.001$) suggests that both records are recording similar changes in the isotopic composition of precipitation related to changes in the strength of the SASM. This conclusion is in contrast to previous studies that attributed isotopic variability in tropical ice cores to temperature (Thompson et al., 2000), but is in agreement with multiple lines of evidence that suggest precipitation variability is the dominant control on $\delta^{18}O$ variability over tropical South America. the primary control on water isotopes in tropical Andean ice cores (i.e. the amount effect; Hastenrath et al., 2004; Hoffmann et al., 2003; Vuille et al., 2003b).

4.6.1 Holocene precipitation trends

The long-term decrease in $\delta^{18}O_{cal}$ at Laguna Pumacocha (~ 0.3‰ per millennium) indicates that the isotopic composition of precipitation at the lake has decreased through the Holocene, likely in response to an increase in the amount of SASM-derived precipitation (Fig. 24d). Alternatively, this decrease in $\delta^{18}O_{cal}$ could signify a gradual reduction in evaporation within the Pumacocha basin through the Holocene, but this scenario is deemed less likely given the remarkable match between Pumacocha and Huascaran and evidence that Pumacocha has remained hydrologically open, even during periods of enhanced aridity. The Pumacocha $\delta^{18}O_{cal}$ trends suggest that the early Holocene was dry in the tropical Andes and that precipitation In

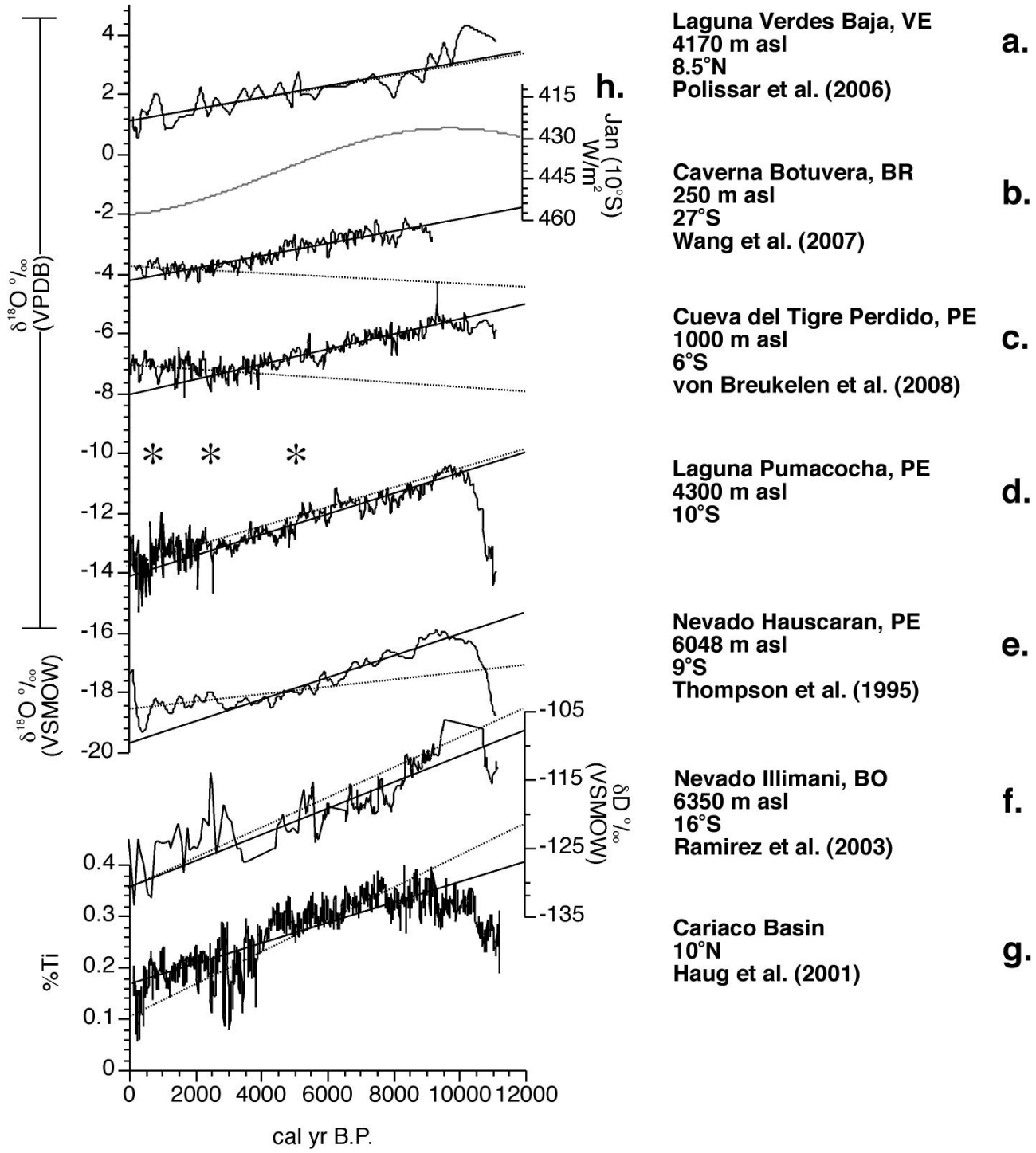

Figure 24 Plot comparing paleoclimate records from (a) Laguna Verdes Baja, VE, (b) Caverna Botuvera, BR, (c) Cueva del Tigre Perdido, PE, (d) Laguna Pumacocha, PE, (e) Huascaran ice core, PE, (f) Illimani ice core, BO, (g) Cariaco Basin, VE. The solid line in each profile is the calculated slope from 10,000 to 2400 cal yr B.P. and the dashed line is the slope calculated from 2400 cal yr B.P. to the present.

addition to the resemblance between the independently dated Huascaran ice core and In addition to the resemblance between the independently dated Huascaran ice core and Pumacocha sediment core $\delta^{18}O$ records discussed above ($r^2 = 0.79$, $p < 0.001$ from 11,200 cal yr B.P. to present; Fig. 24d, e) there is a strong correlation between the Illimani ice core δD record and Pumacocha sediment core $\delta^{18}O$ ($r^2 = 0.73$, $p < 0.001$ from 10,000 cal yr B.P. to present; Fig. 24d, f). The correlation between Pumacocha and Illimani is similar to the correlation between Illimani and Huascaran from 10,000 cal yr B.P. to the present ($r^2 = 0.69$, $p < 0.001$), indicating that all of these records are recording similar climatic signals. Remarkably, Holocene trends in $\delta^{18}O$ measured on diatom silica from Laguna Verdes Baja in the Venezuelan Andes (8.85817° N, 70.87367° W; 4170 m asl) are similar with those from Pumacocha ($r^2 = 0.64$, $p < 0.001$; Fig. 24a, d; Polissar et al., 2006a). This suggests that the NH South American tropics were also dry during the early Holocene.

The robust relationships between ice core $\delta^{18}O$ and δD stratigraphies and lacustrine sediment core $\delta^{18}O$ profiles demonstrate that these geological archives are recording changes in the isotopic composition of precipitation, and that these variations are coherent across both hemispheres of the tropical Andes (Fig. 24a-f). Given the superior resolution of the Pumacocha record (~20 yrs/sample from 2300-11,200 cal yr B.P. and 1.25 yrs/sample from -57 to 2300 varve yr B.P.), we choose this record to represent isotopic shifts in precipitation of the tropical Andes.

The isotopic composition of precipitation over South America is controlled by many factors including the isotopic composition of source waters, the degree of rainout during transport, moisture recycling across the Amazon basin and altitude affects (Sturm et al., 2007; Vuille and Werner, 2005). Polissar et al. (2006a) examined the influence of these processes on

the isotopic composition of precipitation reaching the Andes through the Holocene using a simple modern model. They concluded that the decrease in $\delta^{18}O_{precip}$ through the Holocene was due to a reduction in the fraction of moisture reaching the Andes in response to less effective moisture recycling over the Amazon. This resulted in an increase in the fraction of precipitation lost to runoff and hence more isotopically negative precipitation reaching the Andes. However, this study was limited by the lack of lowland hydrologic records to make inferences about increases or decreases in the amount of precipitation occurring in the Andes relative to the Amazon basin.

New speleothem records from the eastern (Wang et al., 2007) and western (van Breukelen et al., 2008) Amazon basin now allow for a direct assessment of lowland hydrology on long time-scales (Fig. 18, 24b, c). Recently published oxygen isotopic results from speleothems in the 'Nordeste' region of northeastern Brazil (05.60° S, 37.73° W; 100 m asl) indicate that precipitation in this region is anti-phased with the rest of tropical South America (Cruz et al., 2009). Through the Holocene, precipitation has decreased in the 'Nordeste' region, as indicated by a long-term trend toward more positive $\delta^{18}O_{cal}$. A speleothem record from Cueva Tigre de Perdido (CTP), located in the foothills of the Peruvian Andes near the town of Nueva Cajamarca (5.94° S, 77.30° W; 1000 m asl), provides a record of the isotopic composition of precipitation after its passage across the Amazon basin (van Breukelen et al., 2008). In the CTP record, $\delta^{18}O$ is low at the end of the late Glacial, elevated during the early Holocene, and gradually declines through the middle and late Holocene. These trends are similar to those from a speleothem at Caverna Botuvera, Brazil (76.23° S, 49.15° W; 250 m asl), illustrating that the CTP record reflects large-scale hydrologic conditions across the Amazonian lowlands (Fig. 24b, c). The CTP record reflects the isotopic composition of local precipitation after its modification

by rainout and water recycling over the Amazon (i.e., loss of precipitation to runoff and return of precipitation from evapotranspiration), but just prior to its ascent up the eastern flank of the Andes. Like the Andean $\delta^{18}O$ and δD records, CTP shows a steady decrease in $\delta^{18}O$ through the Holocene. However, the slope of this trend begins to lessen between ~5000 and 4000 cal yr B.P., in contrast to the consistent slope observed in the oxygen isotopic records from Huascaran, Illimani, and Laguna Pumacocha (Fig. 24b, c). In fact, there is a decrease in $\delta^{18}O_{cal}$ at Pumacocha at ~5000 cal yr B.P., indicating an increase in tropical Andean effective moisture at this time. The timing of this transition is similar to climatic shifts noted in other Andean paleoclimate records, such as the onset of major glaciation at the Quelccaya Ice Cap and rising lake levels at Lake Titicaca (Baker et al., 2001b; Thompson et al., 2006). A new core from Laguna Azulcocha (12.06825° S, 75.67083° W; 4450 m asl; 160 km south of Pumacocha) helps to further constrain the timing of increase in moisture during the mid-Holocene (Fig. 18, 25; Table 14). Laguna Azulcocha is currently an 11 m deep lake with a very small watershed (< 1 km^2), but prior to ~5400 cal yr B.P. the lakebed was desiccated and occupied by grasses (Fig. 25). After ~5400 cal yr B.P. grasses abruptly transitioned to lake sediments, and by ~4200 cal yr B.P. the sediments were finely laminated, reflecting deep-water conditions. Importantly, the transition from an arid early Holocene to wetter conditions during the middle and late Holocene is observed in several pollen records from a network lakes in Colombia between 3.5° and 4.5° N and 80 to 450 m asl (Behling and Hooghiemstra, 2000). These records support the idea that the northern South American Tropics responded similarly to climatic forcing during the Holocene.

After 2300 cal yr B.P., tropical Andean precipitation continued to increase relative to the Amazon basin. Slope reversals in the lowland speleothem records after 2300 cal yr B.P. indicate that precipitation declined slightly in the Amazon basin at this time (Fig. 24b, c). Persistent

negative slopes in the Andean records, however, suggest that conditions not only remained wet, but that precipitation continued to increase (Fig. 24a, d-f). Greater tropical Andean precipitation after 2300 cal yr B.P. coincides with a major sedimentological change within the Pumacocha basin, when massive sediments abruptly transitioned to finely laminated varves comprised of alternating organic and carbonate rich layers at 2300 cal yr B.P. (Chapter 3). Increased precipitation after 2300 cal yr B.P. also coincides with further increases in lake levels within the Titicaca basin and high lake stands at Lago Taypi Chaka Kkota and Laguna Viscachani in northern Bolivia (Abbott et al., 1997a; Abbott et al., 1997b). The regional synchronicity of these major hydrologic shifts across broad geographical regions underscores their significance and that a common underlying mechanism must be driving them.

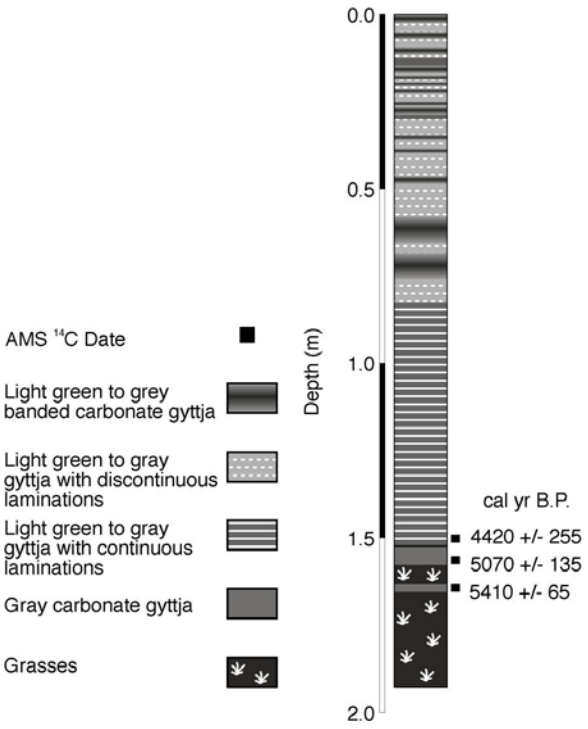

Figure 25 Stratigraphic profile of Laguna Azulcocha (-12.06825°, -75.67083°; 4450 m asl). Radiocarbon dates represented by black boxes constrain the middle Holocene transition from dry conditions indicated by grasses and peat in the core, to lake sediments between 5410 and 5070 cal yr B.P. Laminated sediments after 4420 cal yr B.P. indicate deepwater conditions.

The Laguna Pumacocha $\delta^{18}O_{cal}$ record suggests that the wettest period in the wettest period in the tropical Andes occurred during the late Holocene, between ~700 and 200 varve yr B.P., and coincident with LIA (Fig. 24 b-d). The LIA is a prominent feature in many other Andean records from both hemispheres and is associated with glacial advances, cooler temperatures, and increased precipitation (Chapter 3; Polissar et al., 2006b). Bird (Chapter 3) and Polissar et al. (2006b) presented evidence that suggests radiative forcing played a prominent role in driving tropical climate change during the LIA. Pollisar et al. (2006b) suggested that near surface cooling and possible increases in precipitation in response to reduced radiative forcing was the primary mechanism responsible for the inferred LIA glacial advances. Bird (Chapter 3) attributed the increase in precipitation during the LIA to a warming of the eastern tropical Pacific in response to negative radiative forcing that allowed the Intertropical Convergence Zone (ITCZ) to migrate to a more southerly latitude in both the tropical Atlantic and eastern Pacific, which was subsequently reinforced by a combination of the NH temperature response to lower radiative forcing and North Atlantic cooling remotely forced by the tropical Pacific. Southerly displacement of the ITCZ and its land-based equivalent, together with reduced thermal gradients during the LIA, enhanced middle- to upper-level easterly flow, which in turn increased moisture transport to the high Andes (Garreaud et al., 2003).

Importantly, a LIA hydrologic response is subdued in speleothem records from lowland South America. This implies that the low-lying Amazon basin is not as sensitive to high-frequency changes in radiative forcing as the high Andes. This conclusion is indirectly supported by recently published studies that used instrumental data and model simulations to explore how changes in radiative forcing affect temperatures along an elevation gradient in the Andes (Urrutia and Vuille, 2009; Vuille et al., 2008). These studies clearly demonstrate that

radiative forcing has a greater impact on temperatures at high elevations in the Andes relative to the low elevation Amazon basin. While directed at exploring the effect of anthropogenic greenhouse gases on tropical Andean glaciers, this study illustrates the point that higher elevations in the South American tropics are more sensitive to radiative forcing than the lower elevations.

The general increase in Andean precipitation over the last 10,000 years largely tracks the increase in Southern Hemisphere summer insolation (Fig. 24h; Laskar et al., 2004; Paillard et al., 1996). This observation is in accord with recent model simulations that show monsoons are strongest in the hemisphere with maximum summer insolation (Kutzbach et al., 2008). It has been previously suggested that insolation changes cannot account for the coherent trends in South American precipitation because opposite trends would be expected for the different hemispheres (Polissar et al., 2006a). However, a coherent continental South American response to orbital-scale insolation forcing is supported by evidence from multiple sites in the northern South American tropics that indicates that low lying areas in Colombia (80 to 450 m asl) were dry during the early Holocene and became progressively wetter through the Holocene (Behling and Hooghiemstra, 2000). Given the strong similarities between Andean and Amazonian paleoclimate records from both hemispheres with insolation, we argue that increasing insolation is the primary driver of these trends. In the Northern Hemisphere South American tropics, the response to increasing southern Hemisphere summer insolation may be indirect and mediated by the dynamical response of the tropical Pacific to insolation and radiative forcing. The %Ti record of terrestrial erosion from the Cariaco Basin is more in line with the anticipated NH response to insolation forcing (Haug et al., 2001), showing that the NH tropics were wet during the early Holocene and became progressively drier through the middle and late Holocene. This

is the expected response to insolation forcing in the NH, but opposite of that observed in the Venezuelan Andes and lowland areas of Colombia and Venezuela. However, the dynamics responsible for the apparent paradoxical response of the Venezuelan Andes and low lying areas of Colombia to Holocene-scale insolation trends are beyond the scope of this paper. See Polissar et al. (In Review) for a discussion of this issue.

Precipitation in the Andes is limited by the availability of moisture needed to initiate deep convection (Garreaud et al., 2003). Deep convection requires > 5 g/kg of near surface water vapor, whereas dry conditions are characterized by values below 3 g/kg. Deep convection occurs over the Altiplano during the austral summer when middle- to upper-level easterly flow increases, which advects moisture from the Amazon basin to high elevations. Near surface water vapor in the Amazon basin exceeds 12 g/kg year round, indicating that moisture availability is not limited at the source, but by the ability of atmospheric flow to transport it to elevation. Therefore, the long-term increase in tropical Andean precipitation from the early to late Holocene reflects greater moisture transport to the high Andes via enhanced middle- to upper-level easterly tropospheric flow. The inferred increase in middle- and upper-level easterly flow through the Holocene is consistent with a southward migration of the Intertropical Convergence Zone (ITCZ) over the last 10,000 years in response to precessional insolation forcing, which is observed in several paleoclimate records (Fleitmann et al., 2007; Haug et al., 2001). Because levels of near surface water vapor within the Amazon are in excess of the threshold needed for deep convection, even during times of greater moisture export to the Andes, increased precipitation at elevation does not come at the expense of precipitation in the Amazon (Garreaud et al., 2003).

4.6.2 Holocene precipitation partitioning

The aforementioned differences in tropical Andean and Amazonian precipitation are illustrated semi-quantitatively by the difference between the Pumacocha and CTP $\delta^{18}O$ records ($\delta^{18}O_{Pumacocha\text{-}CTP}$; Fig. 26). Both CTP and Pumacocha incorporate the effects of moisture recycling and precipitation on the isotopic composition of precipitation during its passage over the Amazon basin. However, CTP captures precipitation trends at the foothills of the Andes at 1000 m asl, whereas the Laguna Pumacocha sediment core $\delta^{18}O$ record reflects precipitation at 4300 m asl. The difference between these two records should, therefore, be indicative of differences in precipitation along an elevation gradient. If precipitation trends are similar at these two sites, then the difference between the Pumacocha and CTP $\delta^{18}O$ records should be constant through time. Greater precipitation at Pumacocha, but not at CTP, will produce a lower $\delta^{18}O_{Pumacocha\text{-}CTP}$ value, whereas increased precipitation at CTP relative to Pumacocha will produce a higher $\delta^{18}O_{Pumacocha\text{-}CTP}$ value. This simple interpretive model assumes that altitude affects and the adiabatic lapse rate have been constant thorough time, which may not be a valid assumption, particularly during times with variable radiative forcing (e.g. the LIA). Despite these limitations, the $\delta^{18}O_{Pumacocha\text{-}CTP}$ record captures the salient features of Andean climate change during the Holocene (Fig. 26).

The $\delta^{18}O_{Pumacocha\text{-}CTP}$ record is characterized by a long-term decreasing trend. This suggests an increase in precipitation partitioning between Pumacocha and CTP through the Holocene with the Andes becoming progressively wetter relative to the Amazon basin (Fig. 26). This trend tracks the increase in Southern Hemisphere insolation (Laskar et al., 2004; Paillard et al., 1996) and the inferred southerly migration of the ITCZ (Haug et al., 2001). These

relationships support the idea that moisture transport to the Andes increased to a greater degree relative to the Amazon as a result of strengthened middle- to upper-level easterly tropospheric flow related to the insolation driven latitudinal migration of the ITCZ. The role of middle- to upper-level tropospheric flow is supported by the fact that the Pumacocha and Huascaran $\delta^{18}O$ profiles are similar (6800 and 4300 m asl), but the CTP record (1000 m asl) does not show an increase in precipitation (Fig. 24d, e). Therefore, the change in precipitation occurred between 4300 and 1000 m asl, but is similar at higher elevations.

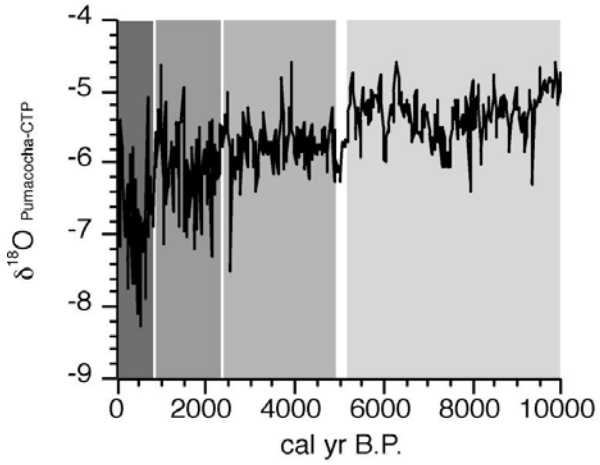

Figure 26 Differences between Andean and Amazonian precipitation are represented by the difference between the Pumacocha $\delta^{18}O_{cal}$ and Cueva del Tigre Perdido $\delta^{18}O_{cal}$ records ($\delta^{18}O_{Pumacocha}$-$\delta^{18}O_{CTP}$).

In addition to the long-term Holocene trend, several discrete isotopic shifts are apparent in the $\delta^{18}O_{Pumacocha-CTP}$ record that mark major climatic transitions in the Andes, which were noted above (Fig. 26). Specifically, transitions to wetter Andean conditions at ~5000 and 2300 cal yr B.P. and 700 varve yr B.P. are clearly visible. The transition at ~5000 cal yr B.P. is a major event that is apparent in several records from the Andes, and indeed is world-wide (e.g. Magney and Haas, 2004). Also apparent in the $\delta^{18}O_{Pumacocha-CTP}$ record, which is not immediately visible in the raw records, is a period of reduced Andean precipitation between ~8000 and 5000

cal yr B.P. (Fig. 26). This period coincides with a significant reduction in lake levels (nearly 85 m) within the Titicaca basin from 8000-5000 cal yr B.P., which suggests that reduced effective moisture at this time occurred at least as far north as Pumacocha, and may have been a pan-Andean event (Baker et al., 2001a; Rowe et al., 2003). Interestingly, this period is coincident with a prolonged increase in solar irradiance as inferred from residual $\Delta^{14}C$ (Reimer et al., 2004), suggesting that solar irradiance may have played an important role during this period However, more high-resolution records from the Andes are necessary to evaluate this idea.

The $\delta^{18}O_{Pumacocha\text{-}CTP}$ record also illustrates just how pronounced the LIA is in the Andes in comparison to the Amazonian lowlands. The LIA is one of the most profound Holocene climate events that was associated with glacial advances across the Andes, cooler temperatures, and increased precipitation (Polissar et al., 2006b). However, the LIA is muted in speleothem records from the Amazon basin. The difference between the Andean and Amazonian records supports recent model simulations and observations that radiative forcing has a more pronounced effect on high elevations in the Andes and suggests radiative forcing has been an import factor in Andean climate change (Vuille et al., 2008).

4.7 SUMMARY AND CONCLUSIONS

This work presents a new 11,200-year-long decadally resolved $\delta^{18}O_{cal}$ record from Laguna Pumacocha, a small alkaline lake in the high Andes of central Peru. The Laguna Pumacocha $\delta^{18}O_{cal}$ record reflects changes in the isotopic composition of precipitation reaching the Andes. The most prominent feature of the Pumacocha record is a long-term decrease in $\delta^{18}O_{cal}$ through the Holocene after an initial rise during the end of the late Glacial Period. This trend suggests

that precipitation was reduced during the early Holocene and subsequently increased throughout the middle and late Holocene. Similar trends are observed in other isotopic records from the Andes, including ice cores from Huascaran and Illimani and lake records from both hemispheres of the South American tropics. Lowland pollen and lake records from Colombia and Venezuela also indicate arid conditions during the early Holocene that transitioned to wetter conditions during the middle Holocene, which strongly suggests that the South American tropics are responding coherently to a common forcing. The likely mechanism driving the increase in precipitation through the Holocene is an increase in the strength of the South American summer monsoon and the southward migration of the ITCZ thorough the Holocene in response to increasing Southern Hemisphere insolation.

Increased precipitation through the Holocene is also inferred from $\delta^{18}O_{cal}$ records preserved in speleothems from the Andean foothills and the southeastern coast of Brazil. Differences between these archives and those from the Andes suggest that precipitation trends in the Andes and Amazon respond differently to similar forcing mechanisms. In particular there are inferred increases in Andean precipitation relative to the Amazon at ~5000, 2300 and 700 cal yr B.P. The timing of these transitions corresponds to major climate changes in the Tropical Andes. The transition to wetter Andean conditions at ~5000 cal yr B.P. coincides with the onset of major glaciation at the Quelccaya Ice Cap, and rising lake levels across the Andes. The shift in the $\delta^{18}O_{Pumacocha\text{-}CTP}$ at 2300 cal yr B.P. coincides with high lake stands at Titicaca and the onset of varved sedimentation at Pumacocha. The most dramatic and abrupt increase in Andean precipitation relative to the Amazon basin occurred at 700 cal yr B.P., which is co-contaminant with increasing precipitation that characterizes the LIA at Pumacocha. Notably, the LIA is conspicuously absent from lowland speleothem records. Studies have shown that solar forcing

and volcanism played a role in driving tropical climate change during the LIA. The lack of a LIA signal in Amazonian and lowland speleothems suggests that solar forcing of precipitation may be restricted to, or simply more pronounced at, high elevations in the Andes.

5.0 SUMMARY AND CONCLUSIONS

The research presented here uses physical sedimentology and geochemical indicators preserved in finely laminated alpine lake sediments to reconstruct Holocene climate change in the Alaskan Arctic and South American tropics. The Arctic amplifies climate change through ocean-atmosphere-cryosphere feedbacks, and variations in the tropical ocean-atmosphere system influence inter-hemispheric temperature and precipitation patterns. Therefore, it is important to understand the natural range of long-term climate variability in these regions in order to understand how these systems will respond to and influence climate in the future climate.

In the Alaskan Arctic, wet, and possibly warmer, conditions occurred from AD 10-730. After AD 730, the climate cooled and became drier, a trend that generally characterizes the last 1275 years. Within this relatively cool, arid period, there are three pronounced warm intervals, AD 1350-1450, AD 1500-1620, and the 20th century, with 20th century warming being the greatest of the three. The longest cool period in the Alaskan Arctic at Blue Lake occurred during the LIA from AD 1620-1880. Although LIA and 20th century warming track changes in radiative forcing, previous climate anomalies do not exhibit a straightforward relationship with radiative forcing. This suggests that other factors, in addition to radiative forcing, influence climate variability in this region.

In the tropical Andes, a 2300-year-long SASM reconstruction from Laguna Pumacocha shows that the SASM has experienced considerable variability during the late Holocene.

Increases and decreases in the strength of the SASM closely track reductions and increases in radiative forcing, respectively, inferred from proxy records of solar activity and net radiative forcing. Because the strength of the modern SASM is closely linked to ocean-atmosphere variability in the tropical Pacific, these results suggest that radiative forcing influenced the tropical Pacific and that its response, in turn, influenced the strength of the SASM. This conclusion is consistent with the dynamical response of the tropical Pacific to radiative forcing. Sea surface temperature variability in the tropical Pacific has been shown to influence Northern Hemisphere climate via El Niño-like teleconnections that resemble the North Atlantic Oscillation. Remote forcing of Northern Hemisphere climate that originates in the tropical Pacific is supported by the resemblance between the Pumacocha SASM reconstruction and reconstructed Northern Hemisphere temperatures of the last 2000 years. This suggests that the tropical Pacific is an important component of the global climate system that has the capacity to influence global climate variability at abrupt and long-term time scales.

SASM variability over the course of the Holocene inferred from the decadally-resolved 11,200-year-long Pumacocha $\delta^{18}O_{cal}$ record closely tracks orbitally induced changes in Southern Hemisphere summer insolation, with an increase in the strength of the SASM corresponding to an increase in Southern Hemisphere summer insolation. This trend is consistent with other paleoclimate records from the tropical Andes and from lowland regions of Colombia, indicating that millennial-scale Holocene climate change is synchronous in these parts of tropical South America. However, comparison of the Pumacocha SASM reconstruction with decadally-resolved speleothem $\delta^{18}O_{cal}$ records from the Peruvian Amazon and southeastern coastal Brazil show elevation dependent differences in the Holocene evolution of the SASM. Specifically, the Andean SASM appears to have become stronger than its Amazonian counterpart during the last

10,000 years. This difference is particularly pronounced during the LIA, which was the largest Andean climate anomaly in the last 11,200 years, but is virtually indistinguishable in the lowland speleothem records. These differences indicate that the Andean SASM, and the factors that influence it, are more sensitive to subtle changes in radiative forcing than its low elevation counterpart.

The research presented in this dissertation provides new information about the evolution of Holocene climate in the Alaskan Arctic and South American tropics and the role of radiative forcing in producing these changes. However, these investigations are but a first step. Future work will be directed toward improving the spatial distribution of high-resolution paleoclimate records from the Arctic and South American tropics in order to answer questions produced by the research presented here. In the Arctic, it will be important to collect new data from other parts of the Brooks Range and the eastern Russian Arctic in order to assess the spatial coherency of the signal captured in the Blue Lake record. As well, it will be important to understand if the inferred warm, wet period from AD 10-730 is recognized across the Alaskan Arctic because this could have implications for the driving mechanisms behind climate variability in this region. In the South American tropics, additional high-resolution records of SASM variability will improve our understanding of the spatial variability of this important system during climate states similar to the present (i.e., the Medieval Climate Anomaly) and those that are different (i.e., the Little Ice Age).

BIBLIOGRAPHY

Abbott, M., Wolfe, B. B., Wolfe, A. P., Seltzer, G. O., Aravena, R., Mark, B., G., Polissar, P. J., Rodbell, D. T., Rowe, H. D., and Vuille, M. (2003). Holocene paleohydrology and glacial history of the central Andes using multiproxy lake sediment studies. *Palaeogeography, Palaeoclimatology, Palaeoecology* **194,** 123-138.

Abbott, M. B., Binford, M. W., Brenner, M., and Kelts, K. R. (1997a). A 350014C yr High-Resolution Record of Water-Level Changes in Lake Titicaca, Bolivia/Peru. *Quaternary Research* **47,** 169-180.

Abbott, M. B., Seltzer, G. O., Kelts, K. R., and Southon, J. (1997b). Holocene Paleohydrology of the Tropical Andes from Lake Records. *Quaternary Research* **47,** 70-80.

Abbott, M. B., and Stafford, T. W. (1996). Radiocarbon geochemistry of modern and ancient Arctic lake systems, Baffin Island, Canada. *Quaternary Research* **45,** 300-311.

Abramovich, R., and Pattee, S. (1999). SNOTEL network-analysis of and future plans for the collection of additional climatic parameters at SNOTEL stations. *Proceedings of the Western Snow Conference***,** 137-140.

Abril, J. M. (2003). Difficulties in interpreting fast mixing in the radiometric dating of sediments using ^{210}Pb and ^{137}Cs. *Journal of Paleolimnology* **30,** 407-414.

Anderson, L., Abbott, M. B., Finney, B. P., and Burns, S. J. (2007). Late Holocene moisture balance variability in the southwest Yukon Territory, Canada. *Quat. Sci. Rev.* **26,** 130-141.

Anderson, L., Abbott, M. B., Finney, B. P., and Edwards, M. E. (2005). Palaeohydrology of the Southwest Yukon Territory, Canada, based on multiproxy analyses of lake sediment cores from a depth transect. *The Holocene* **15,** 1172-1183.

Appleby, P. G., J., N. P., Gifford, D. W., Godfrey, M. J., Oldfield, F., Anderson, N. J., and Battarbee, R. W. (1986). ^{210}Pb dating by low background gamma counting. *Hydrobiologia* **143,** 21-27.

Appleby, P. G., and Oldfield, F. (1983). The assessment of ^{210}Pb data from sites with varying sediment accumulation rates. *Hydrobiologia* **103,** 29-35.

Baker, P. A., Fritz, S. C., Garland, J., and Ekdahl, E. (2005). Holocene hydrologic variation at Lake Titicaca, Bolivia/Peru, and its relationship to North Atlantic climate variation. *Journal of Quaternary Science* **20,** 655-662.

Baker, P. A., Rigsby, C., A., Seltzer, G. O., Fritz, S. C., Lowenstein, T., K., Bacher, N. P., and Veliz, C. (2001a). Tropical climate changes at millennial and orbital timescales on the Bolivian Altiplano. *Nature* **409,** 698-701.

Baker, P. A., Seltzer, G. O., Fritz, S. C., Dunbar, R. B., Grove, M. J., Tapia, P. M., Cross, S. L., Rowe, H. D., and Broda, J. P. (2001b). The history of South American tropical precipitation for the past 25,000 years. *Science* **291,** 640-643.

Bard, E., and Delaygue, G. (2008). Comment on "Are there connection between the Earth's magnetic field and climate?" by V. Courtillot, Y. Gallet, J.-L. Le Mouël, F. Fluteau, A. Genevey EPSL 253, 328, 2007 *Earth and Planetary Science Letters* **265,** 302-307.

Bard, E., Raisbeck, G., Yiou, F., and Jouzel, J. (2000). Solar irradiance during the last 1200 years based on cosmogenic nuclides. *Tellus Series B Chemical and Physical Meteorology* **52,** 985-992.

Bard, E., Raisbeck, G. M., Yiou, F., and Jouzel, J. (1997). Solar modulation of cosmic nuclide production over the last millennium: comparison between 14C and 10Be records. *Earth and Planetary Science Letters* **150,** 453-462.

Behling, H., and Hooghiemstra, H. (2000). Holocene Amazon rainforest-savanna dynamics and climatic implications: high-resolution pollen record from Laguna Loma Linda in eastern Colombia. *Journal of Quaternary Science* **15,** 687-695.

Bertrand, C., Loutre, M.-F., Crucifix, M., and Berger, A. (2002). Climate of the last millennium: a sensitivity study. *Tellus A* **54A,** 221-244.

Besonen, M. R., Patridge, W., Bradley, R. S., Francus, P., Stoner, J. S., and Abbott, M. B. (2008). A record of climate over the last millennium based on varved lake sediments from the Canadian High Arctic. *The Holocene* **18,** 169-180.

Black, D. E., Peterson, L. C., Overpeck, J. T., Kaplan, A., Evans, M. N., and Kashgarian, M. (1999). Eight centuries of North Atlantic ocean-atmosphere variability. *Science* **286,** 1709-1713.

Blass, A., Grosjean, M., Troxler, A., and Strum, M. (2007). How stable are twentieth-century calibration models? A high-resolution summer temperature reconstruction for the eastern Swiss Alps back to AD 1580 derived from proglacial varved sediments. *The Holocene* **17,** 51-63.

Blotzer, L., Abbott, M. B., Bird, B. W., Finney, B. P., Ortiz, J. D., Patterson, W. P., and Anderson, L. (2008). A 4,000-yr lake record of drought variability from Scout Lake, Yukon Territory, Canada. *In* "38th International Arctic Workshop." pp. 184. Institute of Arctic and Alpine Research (INSTAAR), University of Colorado at Boulder.

Bond, G., Kromer, B., Beer, J., Muscheler, R., Evans, M. N., Showers, W., Hoffmann, S., Lotti-Bond, R., Hajdas, I., and Bonani, G. (2001). Persistent solar influence on North Atlantic climate during the Holocene. *Science* **294,** 2130-2136.

Bradley, R. S., Vuille, M., Hardy, D. R., and Thompson, L. G. (2003). Low latitude ice cores record Pacific sea surface temperatures. *Geophys. Res. Lett.* **30,** 1174.

Broccoli, A. J., Dahl, K. A., and Stouffer, R. J. (2006). Response of the ITCZ to Northern Hemisphere cooling. *Geophysical Research Letters* **33,** L01702.

Calkin, P. E., and Ellis, J. M. (1980). A lichenometric dating curve and its application to Holocene glacier studies in the central Brooks Range, Alaska. *Arctic and Alpine Research* **12,** 245-264.

Chiang, J. C. H., and Bitz, C. M. (2005). Influence of high latitude ice cover on the marine Intertropical Convergence Zone. *Climate Dynamics* **25,** 477-496.

Christie, D. A., Lara, A., Barichivich, J., Villalba, R., Morales, M. S., and Cuq, E. (In Press). El Niño-Southern Oscillation signal in the world's highest-elevation tree-ring chronologies from the Altiplano, Central Andes. *Palaeogeography Palaeoclimatology Palaeoecology*.

Clegg, B. F., Tinner, W., Henderson, A., Bigler, C., and Hu, F. S. (2005). Spatial manifestation of the Little Ice Age in Alaska. *EOS Transactions of the American Geophysical Union* **86[52],** Abstract PP31A-1513.

Clement, A. C., Seager, R., Cane, M. A., and Zebiak, S. E. (1996). An ocean dynamical thermostat. *Journal of Climate* **9,** 2190-2196.

Cobb, K. M., Charles, C. D., and Edwards, R. L. (2003). El Niño/Southern Oscillation and tropical Pacific climate during the last millennium. *Nature* **424,** 271-276.

Cockburn, J. M. H., and Lamoureux, S. F. (2007). Century-scale variability in late summer rainfall events recorded over seven centuries in subannually laminated lacustrine sediments, White Pass, British Columbia. *Quaternary Research* **67,** 193-203.

Courtillot, V., Gallet, Y., Mouël, J.-L. L., Fluteau, F., and Genevey, A. (2007). Are there connections between the Earth's magnetic field and climate. *Earth and Planetary Science Letters* **253,** 328-339.

Crowley, T. J. (2000). Causes of climate change over the past 1000 years. *Science* **289,** 270-277.

Crowley, T. J., and Lowery, T. S. (2000). How warm was the Medieval warm period? *Ambio* **29,** 51-54.

Cruz, F. W., Burns, S. J., Karmann, I., Sharp, W. D., Vuille, M., Cardoso, A., Ferrari, J. A., Silva Dias, P. L., and Viana, O. (2005). Insolation-driven changes in atmospheric circulation over the past 116,000 years in subtropical Brazil. *Nature* **434,** 63-66.

Cruz, F. W., Vuille, M., Burns, S. J., Wang, X., Cheng, H., Werner, M., Edwards, L. R., Karmann, I., Auler, A. S., and Nguyen, H. (2009). Orbitally driven east-west antiphasing of South American precipitation. *Nature Geoscience* **2,** 210-214.

Czaja, A., van der Vaart, P., and Marshall, J. (2002). A diagnostic study of the role of remote forcing in tropical Atlantic variability. *Journal of Climate* **15,** 3280-3290.

Ellis, J. M., and Calkin, P. E. (1984). Chronology of Holocene glaciation, central Brooks Range, Alaska. *Geological Society of America Bulletin* **95,** 897-912.

Emile-Geay, J., Cane, M. A., Seager, R., Kaplan, A., and Almasi, P. (2007). El Niño as a mediator of the solar influence on climate. *Paleoceanography* **22,** PA3210.

Erten, H. N., von Gunten, H. R., E., R., and Sturm, M. (1985). Dating of sediments from Lake Zurich (Switzerland) with ^{210}Pb and ^{137}Cs. *Aquatic Sciences-Research Across Boundaries* **47,** 5-11.

Evison, L. H., Calkin, P. E., and Ellis, J. M. (1996). Late-Holocene glaciation and twentieth-century retreat, northeastern Brooks Range, Alaska. *The Holocene* **6,** 17-24.

Fisher, D., Wake, C., Kreutz, K., Yalcin, K., Steig, E., Mayeski, P. A., Anderson, L., Zheng, J., Rupper, S., Zdanowicz, C., Demuth, M., Waskiewicz, M., Dahl-Jensen, D., Goto-Azuma, K., Bourgeois, J., Koerner, R. M., Sekerka, J., Osterberg, E., Abbott, M. B., Finney, B. P., and Burns, S. J. (2004). Stable isotope records from Mount Logan, Eclipse ice cores, and Nearby Jellybean Lake. Water cycle of the North Pacific over 2000 year and over five vertical kilometers: Sudden shifts and tropical connections. *Geographie physique et Quaternaire* **58,** 337-352.

Fleitmann, D., Burns, S. J., Mangini, A., Mudelsee, M., Kramers, J., Villa, I., Neff, U., Al-SubbarA. A., Buettner, A., Hippler, D., and Matter, A. (2007). Holocene ITCZ and Indian monsoon dynamics recorded in stalagmites from Oman and Yemen (Socotra). *Quaternary Science Reviews* **26** 170-188.

Francus, P., and Asikainen, C. A. (2001). Sub-sampling unconsolidated sediments: a solution for the preparation of undisturbed thin-sections from clay-rich sediments. *Journal of Paleolimnology* **26,** 323-326.

Francus, P., Keimig, F., and Besonen, M. (2002). An algorithm to aid varve counting and measurement from thin-sections. *Journal of Paleolimnology* **28,** 283-286.

Garreaud, R., Vuille, M., and Clement, A. (2003). The climate of the Altiplano: Observed current conditions and mechanisms of past changes. *Palaeogeography, Palaeoclimatology, Palaeoecology* **194,** 5-22.

Garreaud, R., Vuille, M., Compagnucci, R., and Marengo, J. (In Press). Present-day South American climate. *Palaeogeography Palaeoclimatology Palaeoecology*.

Gat, J. R. (1996). Oxygen and hydrogen isotopes in the hydrologic cycle. *Annual Reviews in Earth and Planetary Sciences* **24,** 225-262.

Haigh, J. D. (1994). The role of stratospheric ozone in modulating the solar radiative forcing of climate. *Nature* **370,** 544-546.

Haigh, J. D. (2003). The effects of solar variability on the Earth's climate. *Philosophical Transactions of the Royal Society of London* **361,** 95-111.

Hardy, D. R. (1996). Climatic influences on streamflow and sediment flux into Lake C2, northern Ellesmere Island, Canada. *Journal of Paleolimnology* **16,** 133-149.

Hardy, D. R., Vuille, M., Braun, C., Keimig, F., and Bradley, R. S. (1998). Annual and daily meteorological cycles at High Altitude on a tropical mountain. *Bulletin of the American Meteorological Society* **79,** 1899-1913.

Hastenrath, S., Polzin, D., and Francou, B. (2004). Circulation variability reflected in ice core and lake records of the southern tropical Andes. *Climatic Change* **64,** 361-375.

Haug, G., Hughen, K. A., Sigman, D. M., Peterson, L. C., and Rohl, U. (2001). Southward migration of the intertropical convergence zone through the Holocene. *Science (Washington D C)* **293,** 1304-1308.

Hodder, K. R., Gilbert, R., and Desloges, J. R. (2007). Glaciolacustrine varved sediment as an alpine hydroclimatic proxy. *Journal of Paleolimnology* **38,** 365-394.

Hoffmann, G., Ramirez, E., Taupin, J. D., Francou, B., Ribstein, P., Delmas, R. J., Durr, H., Gallaire, R., Simoes, J., Schotterer, U., Stievenard, M., and Werner, M. (2003). Coherent isotope history of Andean ice cores over the last century. *Geophys. Res. Lett.* **30,** 1179-1182.

Hu, F. S., Ito, E., Brown, T. A., Curry, B. B., and Engstrom, D. R. (2001). Pronounced climatic variations in Alaska during the last two millennia. **98** 10552-10556.

Hughen, K. A., Overpeck, J. T., and Anderson, R. F. (2000). Recent warming in a 500-year paleotemperature record from varves sediments, Upper Soper Lake, Baffin Island, Canada. *The Holocene* **10,** 9-19.

Hughen, K. A., Overpeck, J. T., Anderson, R. F., and Williams, K. M. (1996). "The potential for paleoclimatic records from varved Arctic lake sediments: Baffin Island, Eastern Canadian Arctic." The Geological Society, London.

IPCC. (2007). Climate Change 2007: The Physical Science Basis. Contribution of Working Group I to the Fourth Assessment Report of the Intergovernmental Panel on Climate Change (S. Solomon, D. Qin, M. Manning, Z. Chen, M. Marquis, K. B. Averyt, M. Tignor, and H. L. Miller, Eds.). Cambridge University Press, Cambridge, United Kingdom New York, NY, USA.

Jacoby, G. C., Workman, K. W., and D'Arrigo, R. D. (1999). Laki eruption of 1783, tree rings, and disaster for northwest Alaska Inuit. *Quaternary Science Reviews* **18,** 1365-1371.

Kelly, J. S. (1990). Generalized geologic map of the Chandler Lake quadrangle, north-central Alaska (U. S. G. Survey, Ed.), pp. 1 sheet, 19 p.

Kim, S.-T., and O'Neil, J. R. (1997). Equilibrium and nonequilibrium oxygen isotope effects in synthetic carbonates. *Geochimica et Cosmochimica Acta* **61,** 3461-3475.

Kutzbach, J., Liu, X., Liu, Z., and Chen, G. (2008). Simulation of the evolutionary response of global summer monsoons to orbital forcing over the past 280,000 years. *In* "Clim Dyn." pp. 567-579.

Lamoureux, S. (2000). Five centuries of interannual sediment yield and rainfall-induced erosion in the Canadian High Arctic recorded in lacustrine varves. *Water Resources Research* **36,** 309-318.

Lamoureux, S., England, J. H., Sharp, M. J., and Bush, A. B. G. (2001). A varve record of increased 'Little Ice Age' rainfall associated with volcanic activity, Arctic Archipelago, Canada. *The Holocene* **11,** 243-249.

Lamoureux, S. F. (1994). Embedding unfrozen lake sediments for thin section preparation. *Journal of Paleolimnology* **10,** 141-146.

Laskar, J., Robutel, P., Joutel, F., Gastineau, M., Correia, A. C. M., and Levard, B. (2004). A long-term numerical solution for the insolation quantities of the Earth. *Astronomy and Astrophysics* **428,** 261-285.

Leemann, A., and Neissen, F. (1994). Varve formation and the climatic record in an Alpine proglacial lake: calibrating annually laminated sediments against hydrological and meteorological data. *The Holocene* **4,** 1-8.

Leonard, E. M. (1985). Glaciological and climatic controls on lake sedimentation, Canadian Rocky Mountains. *Zeitschrift fur Gletscherkunde und Glazialgeologie* **21,** 35-42.

Li, H. C., and Ku, T. L. (1997). $\delta^{13}C$-$\delta^{18}O$ covariance as a paleohydrological indicator for closed-basin lakes. *Palaeogeography, Palaeoclimatology, Palaeoecology* **133,** 69-80.

Liu, K.-b., Reese, C. A., and Thompson, L. G. (2005). Ice-core pollen record of climatic changes in the central Andes during the last 400 yr. *Quaternary Research* **64,** 272-278.

Magney, M., and Haas, J. N. (2004). A major widespread climatic change around 5300 cal. yr BP at the time of the Alpine Iceman. *Journal of Quaternary Science* **19,** 423-430.

Mann, D. H., Heiser, P. A., and Finney, B. P. (2002b). Holocene history of the Great Kobuk Sand Dunes, Northwestern Alaska. *Quaternary Science Reviews* **21,** 709-731.

Mann, M. E., Cane, M. A., Zebiak, S. E., and Clement, A. (2005). Volcanic and Solar Forcing of the Tropical Pacific over the Past 1000 Years. *Journal of Climate* **18,** 447-456.

Mann, M. E., and Jones, P. D. (2003). Global surface temperatures over the past two millennia. *Geophys. Res. Lett.* **30,** 1820.

Marsh, N., and Svensmark, H. (2000). Cosmic rays, clouds, and climate. *Space Science Reviews* **94,** 215-230.

Maslanik, J. A., Serreze, M. C., and Barry, R. G. (1996). Recent decreases in Arctic summer ice cover and linkages to atmospheric circulation anomalies. *Geophysical Research Letters* **23,** 1677-1680.

Moberg, A., Sonechkin, D. M., Holmgren, K., Datsenko, N. M., and Karlen, W. (2005). Highly variable Northern Hemisphere temperatures reconstructed from low- and high-resolution proxy data. *Nature* **433,** 613-617.

Moore, J. J., Hughen, K. A., Miller, G. H., and Overpeck, J. T. (2001). Little Ice Age recorded in summer temperature reconstruction from varved sediments of Donard Lake, Baffin Island, Canada. *Journal of Paleolimnology* **25,** 503-517.

Mysak, L. A., and Venegas, S. A. (1998). Decadal climate oscillations in the Arctic: A new feedback loop for atmosphere-ice-ocean interactions. *Geophysical Research Letters* **25,** 3607-3610.

Nesje, A. (1992). A piston corer for lacustrine and marine sediments. *Arctic and Alpine Research* **24,** 257-259.

O'Neil, J. R., Clayton, R. N., and Mayeda, T. K. (1969). Oxygen Isotope Fractionation in Divalent Metal Carbonates. *The Journal of Chemical Physics* **51,** 5547.

Paillard, D., Labeyrie, L., and Yiou, P. (1996). Macintosh program performs time-series analysis. *EOS Transactions of the American Geophysical Union* **77,** 379.

Peterson, T. C., Vose, R., Schmoyer, R., and Razuvaev, V. (1998). Global Historical Climatology Network (GHCN) quality control of monthly temperature data. *International Journal of Climatology* **18,** 1169-1179.

Pienitz, R., Smol, J., Last, W. M., Leavitt, P. R., and Cumming, B. F. (2000). Multi-proxy Holocene palaeoclimatic record from a saline lake in the Canadian Subarctic. *The Holocene* **10,** 673-686.

Polissar, P. J., Abbott, M. B., Shemesh, A., Wolfe, A. P., and Bradley, R. S. (2006a). Holocene hydrologic balance of tropical South America from oxygen isotopes of lake sediment opal, Venezuelan Andes. *Earth and Planetary Science Letters* **242,** 375-389.

Polissar, P. J., Abbott, M. B., Wolfe, A. P., Bezada, M., Rull, V., and Bradley, R. S. (2006b). Solar modulation of Little Ice Age climate in the tropical Andes. *PNAS* **103,** 8937-8942.

Quispensivana, L. Q. (1996). Mapa geologico del cuadrangulo de Cerro de Pasco (I. G. M. y. M. Ministerio de Energia y Minas, Ed.).

Rabatel, A., Francou, B., Jomelli, V., Naveau, P., and Grancher, D. (2008). A chronology of the Little Ice Age in the tropical Andes of Bolivia (16ºS) and its implications for climate reconstruction. *Quaternary Research* **70,** 198-212.

Rabatel, A., Jomelli, V., Naveau, P., Francou, B., and Grancher, D.

Rabus, B. T., and Echelmeyer, K. A. (1998). The mass balance of McCall Glacier, Brooks Range Alaska, U.S.A.; its regional relevance and implication for climate change in the Arctic. *Journal of Glaciology* **44,** 333-351.

Ramirez, E., Hoffmann, G., Taupin, J. D., Francou, B., Ribstein, P., Caillon, N., Ferron, F. A., Landais, A., Petit, J. R., Pouyaud, B., Schotterer, U., Simones, J. C., and Stievenard, M. (2003). A new Andean deep ice core from Nevado Illimani (6350 m), Bolivia. *Earth and Planetary Science Letters* **212,** 337-350.

Reimer, P. J., Baillie, M. G. L., Bard, E., Bayliss, A., Beck, J. W., Bertrand, C. J. H., Blackwell, P. G., Buck, C. E., S., B. G., Cutler, K. B., Damon, P. E., Edwards, R. L., Fairbanks, R. G., Friedrich, M., Guilderson, T. P., Hogg, A. G., Hughen, K. A., Kromer, B., McCormac, F. G., Manning, S. W., Ramsey, C. B., Reimer, R. W., Remmele, S., Southon, J. R., Stuiver, M., Talamo, S., Taylor, F. W., van der Plicht, J., and Weyhenmeyer, C. E. (2004). IntCal04 Terrestrial radiocarbon age calibration, 26-0 ka B.P. *Radiocarbon* **46,** 1029-1058.

Rigor, I., G., Colony, R. L., and Martin, S. (2000). Variation in Surface Air Temperature Observations in the Arctic, 1979-97. *Journal of Climate* **13,** 896-914.

Rodbell, D. T., Seltzer, G. O., Anderson, D. M., Abbott, M. B., Enfield, D. B., and Newman, J. H. (1999). An ~15,000-year record of El Nino driven alluniation in southwestern Ecuador. *Science* **283,** 516-520.

Rowe, H. D., Guilderson, T. P., Dunbar, R. B., Southon, J. R., Seltzer, G. O., Mucciarone, D. A., Fritz, S. C., and Baker, P. A. (2003). Late Quaternary lake-level changes constrained by radiocarbon and stable isotope studies on sediment cores from Lake Titicaca, South America. *Global and Planetary Change* **38,** 273-290.

Rozanski, K., Araguás-Araguás, and Gonfiantini, R. (1992). Relation between long-term trends of oxygen-18 isotope composition of precipitation and climate. *Science* **258,** 981-985.

Schelske, C. L., Peplow, A., Brenner, M., and Spencer, C. N. (1994). Low-background gamma counting: applications for ^{210}Pb dading of sediments.

Seltzer, G., Rodbell, D., and Burns, S. (2000). Isotopic evidence for late Quaternary climatic change in tropical South America. *Geology* **28,** 35-38.

Shindell, D. T., Schmidt, G. A., Mann, M. E., Rind, D., and Waple, A. (2001). Solar forcing of regional climate change during the Maunder Minimum. *Science* **294,** 2149-2152.

Sikorski, J. J., Kaufman, D. S., Manley, W. F., and Nolan, M. (In Press). Winter accumulation at the equilibrium line of Little Ice Age glaciers, Brooks Range, Alaska. *Arctic, Antarctic, and Alpine Research*.

Smith, S. V., Bradley, R. S., and Abbott, M. B. (2004). A 300 year record of environmental change from Lake Tuborg, Ellesmere Island, Nunavut, Canada. *Journal of Paleolimnology* **32,** 137-148.

Snowball, I., and Muscheler, R. (2007). Palaeomagnetic intensity data: an Achilles heel of solar activity reconstructions. *The Holocene* **17,** 851-859.

Stafford, J. M., Wendler, G., and Curtis, J. (2000). Temperature and precipitation of Alaska: 50 year trend analysis. *Theor. Appl. Climatol.* **67,** 33-44.

Stroeve, J., Serreze, M., Drobot, S., Gearheard, S., Holland, M., Maslanik, J., Meier, W., and Scambos, T. (2008). Arctic sea ice extent plummets in 2007. *EOS* **89,** 2 pp.

Stuiver, M., and Reimer, P. J. (1993). Extended 14C database and revised CALIB radiocarbon calibration program. *Radiocarbon* **35,** 215-230.

Sturm, C., Hoffmann, G., and Langmann, B. (2007). Simulation of the Stable Water Isotopes in Precipitation over South America: Comparing Regional to Global Circulation Models. *In* "J Climate." pp. 3730.

Svensmark, H. (1998). Influence of Cosmic Rays on Earth's Climate. *Physical Review Letters* **81,** 5027-5030.

Thompson, L. G., Davies, M. E., Mosley-Thompson, E., Sowers, T. A., Henderson, K. A., Zagorodnov, V. S., Lin, P.-N., Mikhalenko, V. N., Campen, R. K., Bolzan, J. F., Cole-Dai, J., and Francou, B. (1998). A 25,000-Year Tropical Climate History from Bolivian Ice Cores. *Science* **282,** 1858-1864.

Thompson, L. G., Ellen Mosley-Thompson, M. E. D., Lin, P.-N., Henderson, K. A., and Mashiotta, T. A. (2005). Tropical ice core records: evidence for asynchronous glaciation on Milankovitch timescales. *Journal of Quaternary Science* **20,** 723-733.

Thompson, L. G., Mosley-Thompson, E., Bolzan, J. F., and Koci, B., R. (1985). A 1500-Year Record of Tropical Precipitation in Ice Cores from the Quelccaya Ice Cap, Peru. *Science* **229,** 971-973.

Thompson, L. G., Mosley-Thompson, E., Brecher, H., and Davis, M. (2006). Abrupt tropical climate change: Past and present. *Proceedings of the National Academy of Sciences* **103,** 10536-10543.

Thompson, L. G., Mosley-Thompson, E., Davies, M. E., Lin, P.-N., Henderson, K. A., Cole-Dai, J., Bolzan, J. F., and Liu, K.-B. (1995). Late Glacial Stage and Holocene Tropical Ice core Records from Huascaran, Peru. *Science* **269,** 46-50.

Thompson, L. G., Mosley-Thompson, E., and Henderson, K. A. (2000). Ice-core palaeoclimate records in tropical South America sinde the last Glacial Maximum. *Journal of Quaternary Science* **15,** 377-394.

Torrence, C., and Compo, G. P. (1998). A practicle guide to wavelet analysis. *Bulletin of the American Meteorological Society* **79,** 61-78.

Trouet, V., Esper, J., Graham, N. E., Baker, A., Scourse, J. D., and Frank, D. C. (2009). Persistent positive North Atlantic Oscillation mode dominated the Medieval Climate Anomaly. *Science* **324,** 78-80.

Urrutia, R., and Vuille, M. (2009). Climate change projections for the tropical Andes using a regional climate model: Temperature and precipitaton simulations for the end of the 21st century. *Journal of Geophysical Research* **114,** D02108.

Usoskin, I. (2004). Latitudinal dependence of low cloud amount on cosmic ray induced ionization. *Geophysical Research Letters* **31,** 4.

van Breukelen, M. R., Vonhof, H. B., Hellstrom, J. C., W.C.G., W., and Kroon, D. (2008). Fossil dripwater in stalagmites reveals Holocene temperature and rainfall variation in Amazonia. *Earth and Planetary Science Letters* **275,** 54-60.

Villar, J. C. E., Ronchail, J., Guyot, J. L., Cochonneau, G., Naziano, F., Lavado, W., De Oliveira, E., Pombosa, R., and Vauchel, P. (2008). Spatio-temporal rainfall variability in the Amazon basin countries (Brazil, Peru, Bolivia, Colombia, and Ecuador). *International Journal of Climatology*.

Vizy, E. K., and Cook, K. H. (2007). Relationship between Amazon and high Andes rainfall. *Journal of Geophysical Research* **112,** D07107.

Vuille, M., Bradley, R. S., Werner, M., Healy, R., and Keimig, F. (2003a). Modeling d18O in precipitation over the tropical Americas: 1. Interannual variability and climatic controls. *Journal of Geophysical Research* **108,** 24.

Vuille, M., Bradley, R. S., Werner, M., Healy, R., and Keimig, F. (2003b). Modeling d180 in precipitation over the tropical Americas: 2. Simulation of the stable isotope signal in Andean ice cores. *Journal of Geophysical Research* **108,** 16.

Vuille, M., Francou, B., Wagnon, P., Juen, I., Kaser, G., Mark, B. G., and Bradley, R. S. (2008). Climate change and tropical Andean glaciers: Past, present, and future. *Earth-Science Reviews* **89,** 79-96.

Vuille, M., and Werner, M. (2005). Stable isotopes in precipitation recording South American summer monsoon and ENSO variability: Observations and model results. *Climate Dynamics* **25,** 401-413.

Wang, X., Auler, A., Edwards, R., Cheng, H., Ito, E., Wang, Y., Kong, X., and Solheid, M. (2007). Millennial-scale precipitation changes in southern Brazil over the past 90,000 years. *Geophysical Research Letters* **34,** L23701.

Wirrmann, D., and De Oliveira Almeida, L. F. (1987). Low Holocene level (7700 to 3650 years ago) of Lake Titicaca (Bolivia). *Palaeogeography Palaeoclimatology Palaeoecology* **59,** 315-323.

Wright, H. E., Mann, D. H., and Glaser, P. H. (1984). Piston corers for peat and lake sediments. *Ecology* **65,** 657-659.

Zhou, J., and Lau, K.-M. (1998). Does a monsoon climate exist over South America? *Journal of Climate* **11,** 1020-1040.